

## EDITORIAL BOARD

### Editor-in-Chief

Igor Krivtsun  
E.O. Paton Electric Welding Institute of the NASU, Kyiv,  
Ukraine

### Deputy Editor-in-Chief

Serhii Akhonin  
E.O. Paton Electric Welding Institute of the NASU, Kyiv,  
Ukraine

### Deputy Editor-in-Chief

Leonid Lobanov  
E.O. Paton Electric Welding Institute of the NASU, Kyiv,  
Ukraine

### Editorial Board Members

Olena Berdnikova  
E.O. Paton Electric Welding Institute of the NASU, Kyiv,  
Ukraine

Yunlong Chang  
School of Materials Science and Engineering,  
Shenyang University of Technology, China

Chunlin Dong  
Guangzhou Jiao Tong University, China

Michael Gasik  
Aalto University Foundation, Finland

Len Gelman  
The University of Huddersfield, UK

Andrey Gumenyuk  
Bundesanstalt für Materialforschung und –prüfung (BAM),  
Berlin, Germany

Jacob Kleiman  
Integrity Testing Laboratory, Markham, Canada

Vitalii Knysh  
E.O. Paton Electric Welding Institute of the NASU, Kyiv,  
Ukraine

Volodymyr Korzhyk  
E.O. Paton Electric Welding Institute of the NASU, Kyiv,  
Ukraine

Victor Kvasnytskyi  
NTUU «Igor Sikorsky Kyiv Polytechnic Institute», Ukraine

Eric Macdonald  
The University of Texas at El Paso, USA

Serhiy Maksymov  
E.O. Paton Electric Welding Institute of the NASU, Kyiv,  
Ukraine

Dhanesh G. Mohan  
School of Engineering University of Sunderland England,  
United Kingdom

João Pedro Oliveira  
Universidade NOVA de Lisboa, Portugal

Mykola Pashchin  
E.O. Paton Electric Welding Institute of the NASU, Kyiv,  
Ukraine

Valeriy Pozniakov  
E.O. Paton Electric Welding Institute of the NASU, Kyiv,  
Ukraine

Uwe Reisgen  
Welding and Joining Institute, Aachen, Germany

Massimo Rogante  
Rogante Engineering, Civitanova Marche, Italy

Cezary Senderowski  
Mechanics and Printing Institute, Warsaw University  
of Technology, Poland

Magdalena Speicher  
Kempten University of Applied Sciences, Germany

Mattias Thuvander  
Chalmers University of Technology, Goteborg, Sweden

Valentyn Uchanin  
Karpenko Physico-Mechanical Institute, Lviv, Ukraine

Yongqiang Yang  
South China University of Technology, Guangzhou, China

**Executive Editor**  
Oleksandr Zelnichenko  
International Association "Welding", Kyiv, Ukraine

### Address of Editorial Office

E.O. Paton Electric Welding Institute, 11 Kazymyr Malevych Str., 03150, Kyiv, Ukraine  
Tel./Fax: (38044) 205 23 90, E-mail: [journal@paton.kiev.ua](mailto:journal@paton.kiev.ua), [patonpublishinghouse@gmail.com](mailto:patonpublishinghouse@gmail.com)  
<https://patonpublishinghouse.com/eng/journals/tpwj>

The Journal was registered by the National Council of Ukraine on Television and Radio Broadcasting on 09.05.2024,  
carrier identifier R30-04569, ISSN 0957-798X, DOI: <http://dx.doi.org/10.37434/tpwj>

### Subscriptions, 12 issues per year:

\$384 — annual subscription for the printed (hard copy) version, air postage and packaging included;  
\$312 — annual subscription for the electronic version (sending issues in pdf format or providing access to IP addresses).

### Representative Offices of "The Paton Welding Journal":

#### BRAZIL, Arc Dynamics

Address: Nova Iguacu, Rio de Janeiro, Brazil  
Daniel Adolpho, Tel.: +55 21 9 6419 5703, E-mail: [dadolpho@arcdynamics.com.br](mailto:dadolpho@arcdynamics.com.br)

#### BULGARIA, Bulgarian Welding Society

Address: Blvd. Asen Yordanov No.10, Sofia 1592, Bulgaria  
Pavel Popgeorgiev, Tel.: +359 899 96 22 20, E-mail: [office@bws-bg.org](mailto:office@bws-bg.org)

#### CHINA, China-Ukraine Institute of Welding, Guangdong Academy of Sciences

Address: Room 210, No. 363 Changxing Road, Tianhe, Guangzhou, 510650, China  
Zhang Yupeng, Tel.: +86-20-61086791, E-mail: [patonjournal@gwi.gd.cn](mailto:patonjournal@gwi.gd.cn)

#### POLAND, PATON EUROPE Sp. z o. o.

Address: ul. Kapitałowa 4, 35-213, Rzeszów, Poland  
Anton Stepakhno, Tel.: +38067 509 95 67, E-mail: [Anton.Stepakhno@paton.ua](mailto:Anton.Stepakhno@paton.ua)

The content of the Journal includes articles received from authors from around the world in the field of welding, cutting, cladding, soldering, brazing, coating, 3D additive technologies, electrometallurgy, material science, NDT and selectively includes translations into English of articles from the following journals, published in Ukrainian:

- Automatic Welding ([https://patonpublishinghouse.com/eng/journals/as](https://patonpublishinghouse.com/eng/journals/as;));
- Electrometallurgy Today (<https://patonpublishinghouse.com/eng/journals/sem>);
- Technical Diagnostics & Nondestructive Testing (<https://patonpublishinghouse.com/eng/journals/tdnk>).

CONTENTS

ORIGINAL ARTICLES

<b>V.I. Shvets, I.V. Ziakhor, L.M. Kapitanchuk, O.V. Didkovskyi, E.V. Antipin</b> PECULIARITIES OF FRACTURE OF WELDED JOINTS OF RAILWAY RAILS OF OXYGEN-CONVERTER K76F STEEL *	3
<b>Khokhlov M.A., Makhnenko O.O., Kostin V.A., Pokliatskyi A.G., Falchenko Iu.V., Khokhlova Yu.A.</b> THERMOMECHANICAL PROCESSES IN FRICTION STIR WELDING OF MAGNESIUM ALLOY SHEETS*	11
<b>T.M. Labur, A.G. Pokliatskyi, V.A. Koval</b> CONSUMABLE AND NONCONSUMABLE ELECTRODE WELDING OF HIGH-STRENGTH 2219-T31 ALUMINIUM ALLOY*	18
<b>V.G. Solovyov, Yu.M. Kuskov, I.Yu. Romanova</b> OPTIMIZATION OF THE METAL POOL SHAPE DURING ELECTROSLAG SURFACING IN A STATIONARY CURRENT-SUPPLYING MOULD FOR MANUFACTURE OF BIMETALLIC PRODUCTS*	28
<b>P.S. Shlonskyi, Feng Gao</b> STRUCTURE AND MECHANICAL PROPERTIES OF TITANIUM ALLOY-CARBON STEEL BIMETAL OBTAINED BY EXPLOSION WELDING**	37
<b>Ja. Kleiman</b> UltraMARS SYSTEM FOR NON-DESTRUCTIVE MEASUREMENT OF RESIDUAL STRESSES: NEW DEVELOPMENTS	41
<b>M.M. Gasik</b> SIMULATION OF ELECTRIC ARC MODE OF ELECTRIC FURNACE AND ANALYSIS OF ITS OPERATION IN REAL TIME***	48

INFORMATION

DNIPROMETYZ TAS: Expanding Horizons at the Düsseldorf WIRE 2024 Exhibition	53
--	----

\*Translated Article(s) from “Automatic Welding”, No. 3, 2024.  
\*\*Translated Article(s) from “Automatic Welding”, No. 2, 2024.  
\*\*\*Translated Article(s) from “Electrometallurgy Today”, No. 2, 2024.

# PECULIARITIES OF FRACTURE OF WELDED JOINTS OF RAILWAY RAILS OF OXYGEN-CONVERTER K76F STEEL

**V.I. Shvets, I.V. Ziakhor, L.M. Kapitanchuk, O.V. Didkovskyi, E.V. Antipin**

E.O. Paton Electric Welding Institute of the NASU

11 Kazymyr Malevych Str., 03150, Kyiv, Ukraine

## ABSTRACT

The fracture surface of rail K76F steel after static bending tests of rail butt joints produced by flash-butt welding was studied. Butt joints of rails of individual batches were fractured on the base metal or heat-affected zone (HAZ). It is shown that in the regions of dark colour and oval shape, the fracture on the iron oxide film takes place. The formation of films occurs as a result of melting and distribution of iron oxide inclusions along the structural boundaries probably in the thermo-deformation conditions of the crimping shop at the stage of blooming production. The formation of clusters of iron oxides occurs during the crystallization of the residual melt in steel ingots with an insufficient degree of deoxidation. Oval regions of dark colour on the fracture surface are evidence of an insufficient degree of deoxidation of rail steel and a factor of its quality reduction.

**KEYWORDS:** rail K76F steel, deoxidation, flash-butt welding, iron oxide

## INTRODUCTION

At present, the oxygen-converter method is mainly used for melting rail steel. Compared to the open-hearth method, it is distinguished by higher efficiency, lower capital costs, more favourable conditions for mechanization and automation of production processes, combination of the process of steel melting with continuous casting. The essence of the oxygen-converter method consists in blowing of liquid pig iron with oxygen in the aggregate-converter. Under the action of oxygen, pig iron impurities like manganese, silicon and, above all, carbon are oxidized and removed from the melt.

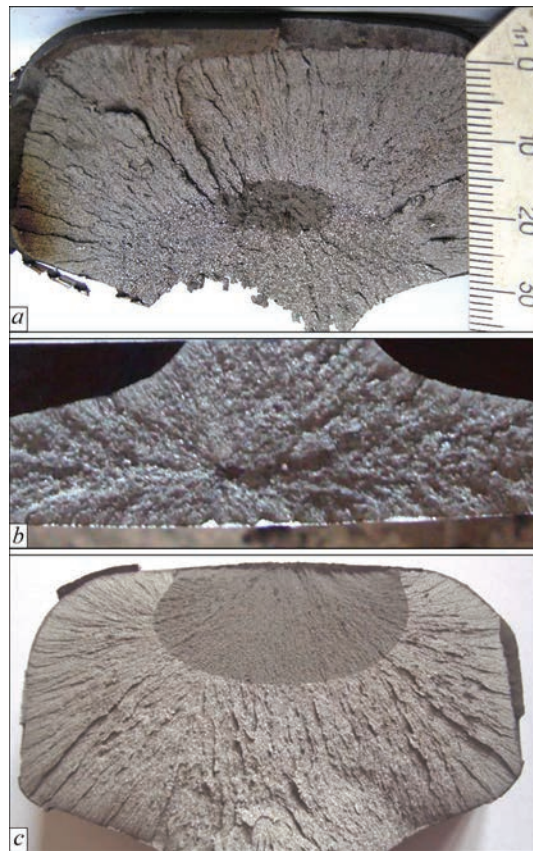
JSC Ukrzaliznytsia uses R65 type rails of K76F grade of converter production, hardened with induction heating along the entire length of rolling surface and side edges [1]. The results of qualification tests showed that the developed technology of rail production provided the compliance of their properties with the requirements of regulatory documents [2]. To join rails during the construction of railway tracks, the technology of flash-butt welding was used, developed at the PWI of the NASU and successfully realized in practice [3, 4].

During mechanical static bending tests, fracturing of rail joints usually occurs on the butt joint. The rail joints of individual batches were fractured on the base metal or HAZ. During visual inspection, regions of the oval shape were detected on the fracture surface, which were of dark colour due to peculiar features of the relief. In the work, these regions are defined as “oval spots” (OS) (Figure 1). OS, which were nuclei of butt joint fracture, were located mainly in the rail head (Figure 1, *a*), rarely — in the foot (Figure 1, *b*).

The aim of the work consisted in finding the nature and causes of OS formation on the fracture surface of welded butt joints of K76F rails.

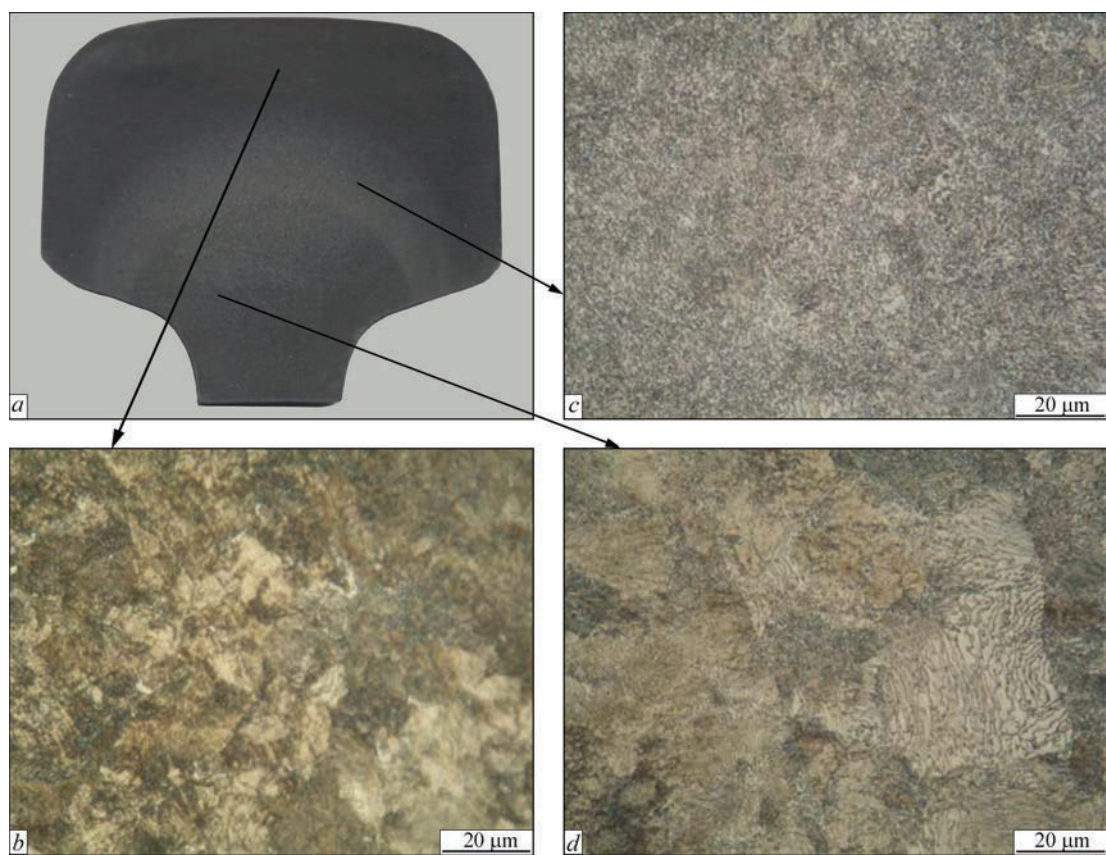
## PROCEDURE AND EQUIPMENT

K76F rails were investigated after fracturing of butt joints during the static bending tests. Analysis of the rail macrostructure was carried out on templates

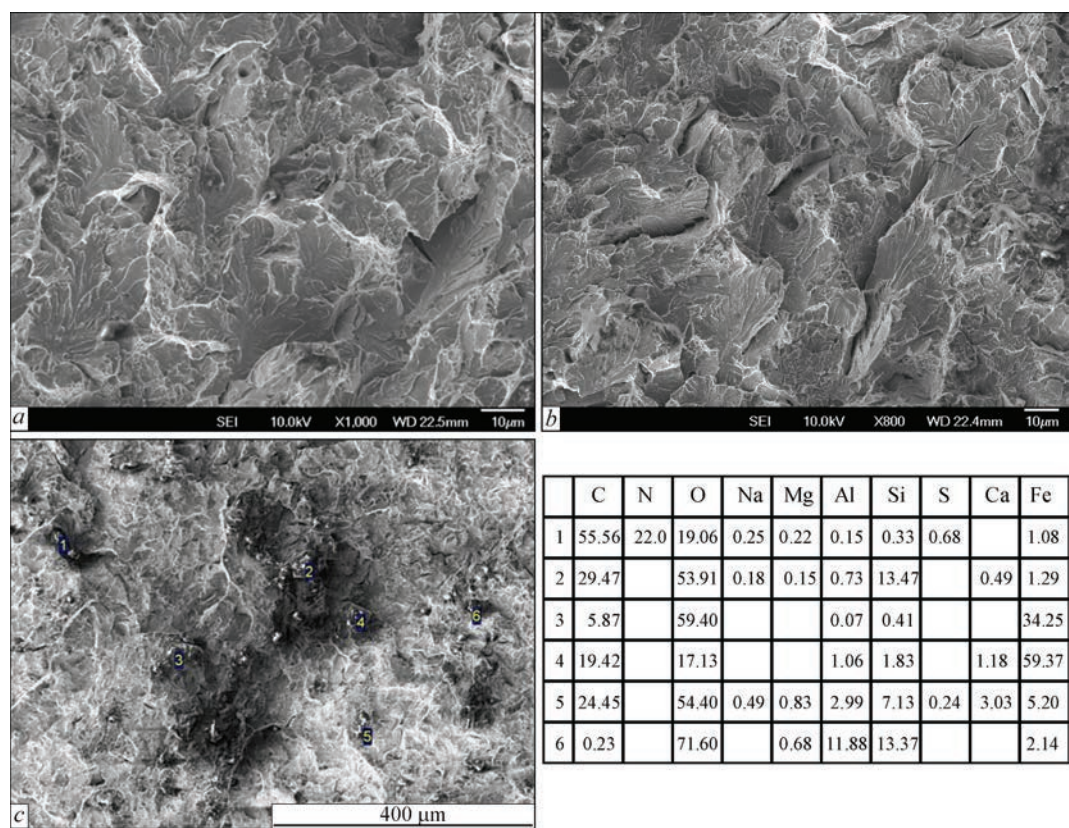


**Figure 1.** Oval spots on the fracture surface of rails: *a* — in the head area; *b* — in the foot area; in the head area at a distance of 7 mm from the joint line





**Figure 2.** *a* — rail macrostructure in the head area, ×1000; *b* — near-surface layer; *c* — tempering regions; *d* — base metal



**Figure 3.** Fracture surface in the region of heat-hardened layer (*a*, *b*), nonmetallic inclusions (*c*) and results of X-ray microanalysis of chemical composition (at.%)

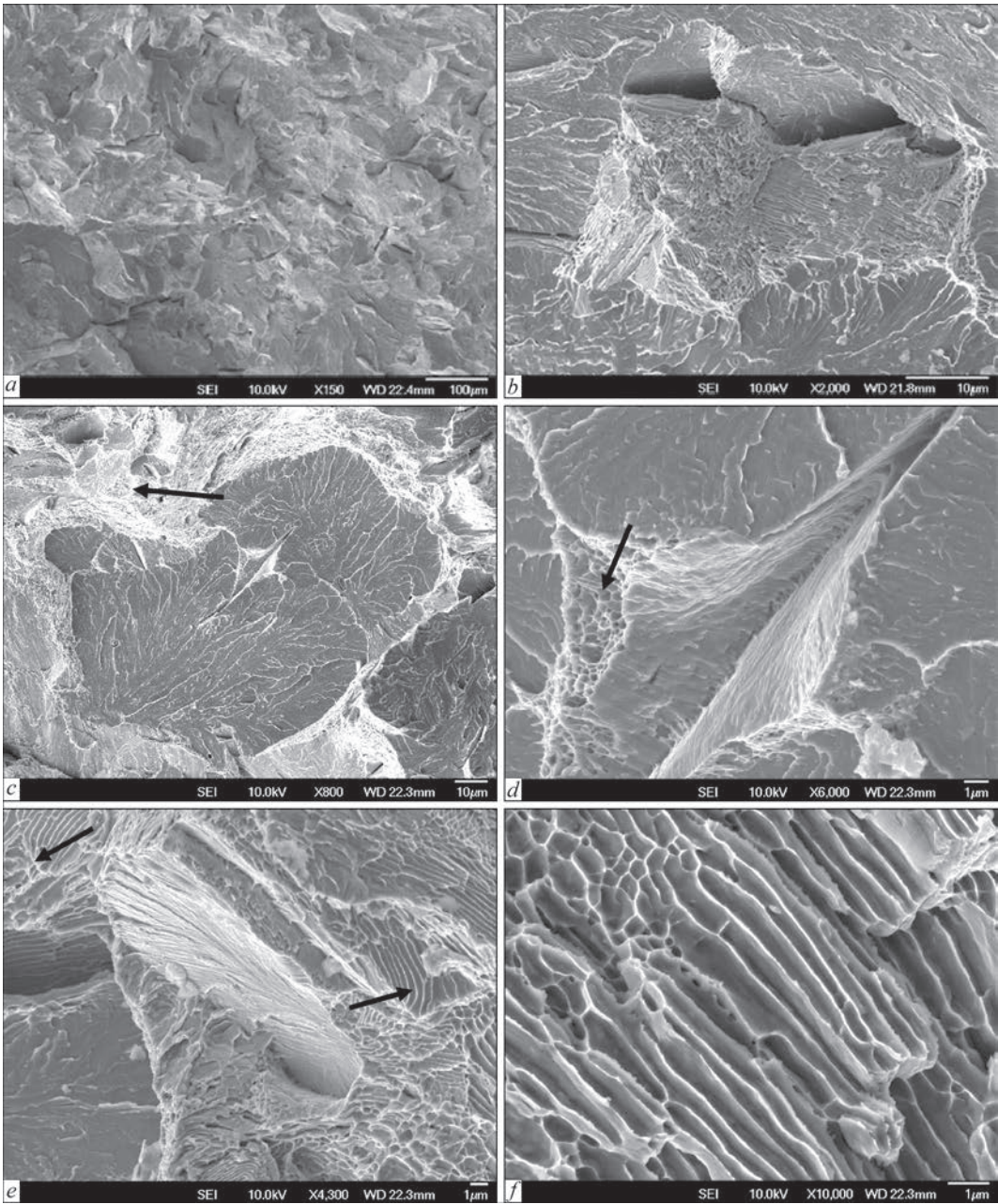


**Table 1.** Chemical composition of K76F rails, wt. %

Element	C	Mn	Si	V	Ti	Cr	P	Al	S
Grade composition	0.71–0.82	0.80–1.30	0.25–0.45	0.03–0.07	–	≤0.15	≤0.035	≤0.015	≤0.04
Composition of investigated rails	0.76	0.85	0.317	<0.02	0.005	0.04	0.013	0.015	<0.03

cut out in the cross direction. Microstructure examinations were conducted in the optical microscope NEOPHOT-32, equipped with a digital camera. Microstructure was revealed by etching of preliminary polished specimens in a 4 % HNO<sub>3</sub> alcohol solution. To analyze the microstructure and chemical heterogeneity of the fracture surface during fracturing on the base metal, Auger-microprobe JAMP 9500F of JEOL Company (Japan) was used, on which the X-ray energy dispersive spectrometer JNCA Penta FET x3 of

Oxford Instrument Company is installed. The energy of the primary electron beam was 10 keV at a current of 0.5 nA for the method of micro X-ray diffraction analysis (MXRD) and of 10 nA for the method of Auger-electron spectroscopy. To build the distribution of elements in depth, the specimen surface was bombarded by Ar<sup>+</sup> ions (ion etching) with the energy of 3 keV and etching rate of 20 nm/min. Vickers’s hardness was measured in a hardness tester NOVOTEST TC-GPB with a load of 292.4 N (30 kg).



**Figure 4.** Fracture surface in the tempering region (a, b); opening of metal on the film of iron oxide (c, d); opening of metal on the pearlite colonies (e, f)

RESEARCH RESULTS AND DISCUSSION

According to the results of spectral analysis, the chemical composition of the metal in the investigated rails corresponds to the grade one (Table 1). The rail macrostructure does not reveal disorders of metal continuity. In the head area, the regions of HAZ are clearly revealed, typical for the rails after surface heat treatment (Figure 2, *a*). Near the rolling surface, a heat-hardened layer of dark colour of up to 15 mm width is observed. This layer is adjacent to a layer of gray colour (tempering area), which is distinguished by a reduced hardness compared to the near-surface layer and base metal: *HV* 2430–2680 MPa, *HV* 3590–3800 MPa and *HV* 2700–3040 MPa, respectively. Microstructure of the near-surface layer of a dark colour is sorbite (Figure 2, *b*), and that of a gray layer and the base metal is sorbite-pearlite (Figure 2, *c, d*).

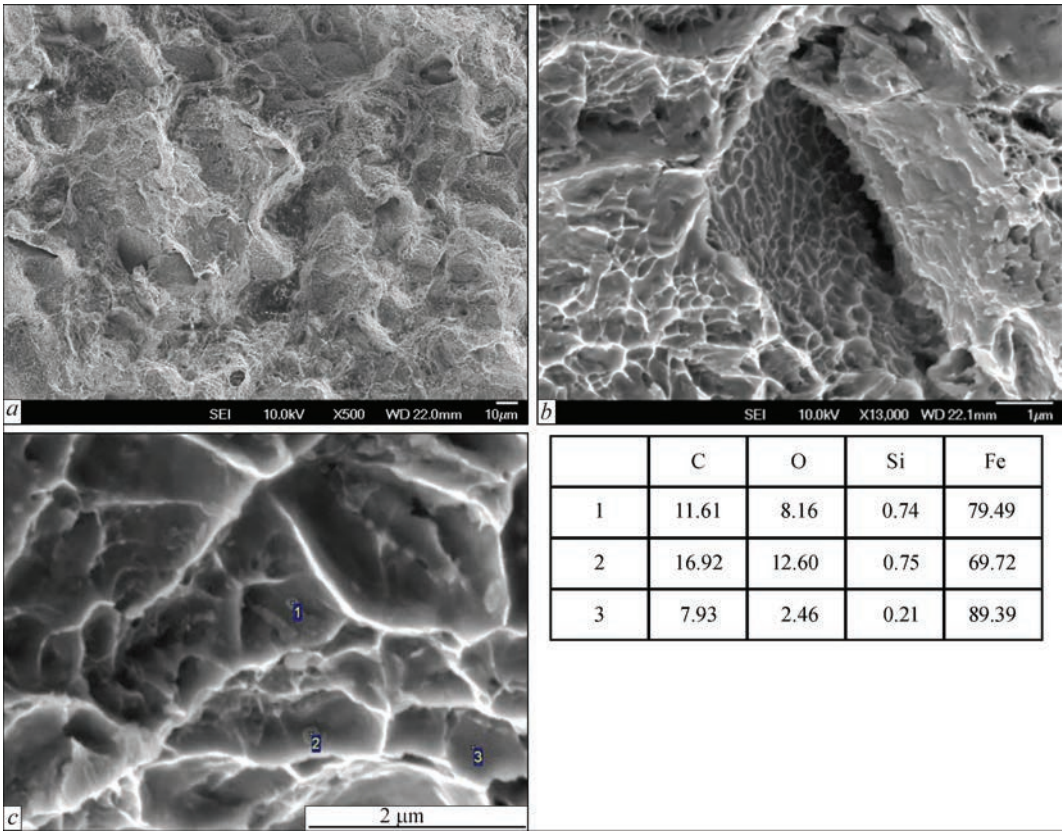
Fractographic examinations of the fracture surface during fracturing on the base metal showed that within the heat-hardened layer, the fracture is transcrystalline. The fracture surface consists of facets of intragranular spalling with elements of plastic deformation: stream-like pattern, tongues, tear crests (Figure 3, *a*). In some places, secondary cracks are encountered (Figure 3, *b*). Nonmetallic inclusions on the fracture surface are represented by complex oxides of aluminium, calcium and silicon (Figure 3, *c*; Table 1).

The formation of oxide clusters is a cause for the formation of a developed relief in this region.

In the tempering region, the fracture is mostly transcrystalline. However, fracturing is accompanied by the formation of spalling facets (Figure 4, *a*). Numerous secondary cracks (Figure 4, *b*) are present near spalling facets in the microstructure, places of metal opening on the film structural component (Figure 4, *c, d*) and pearlite colonies (Figure 4, *d, e*) are observed.

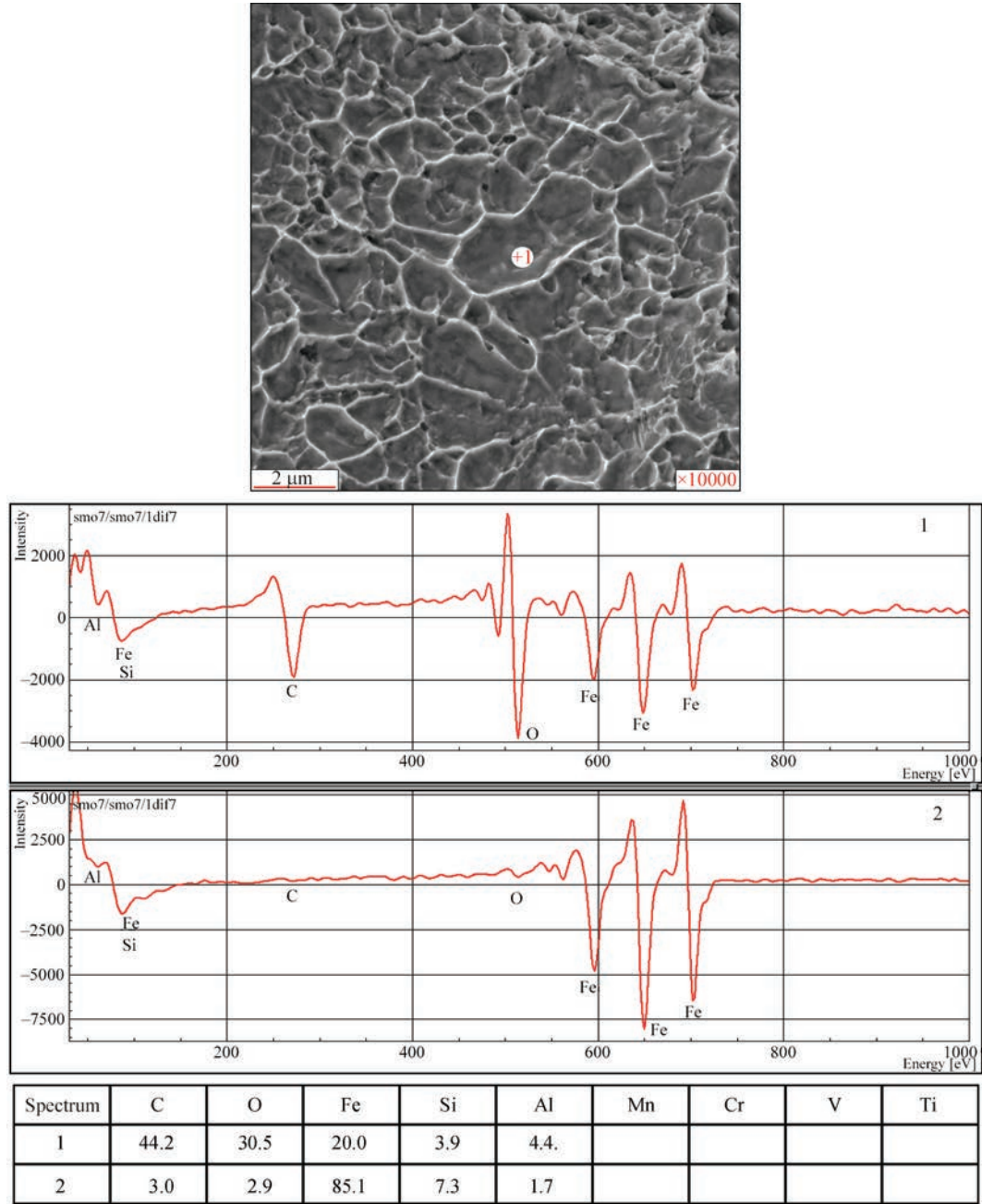
In the OS region, unlike in the tempering regions and a heat-hardened layer, the fracture is intercrystalline (Figure 5, *a*). The fracturing surface is dimple (Figure 5, *b*). According to the chemical composition, the particles, which are located in the dimples and determine the nature of fracture, are iron oxide (Figure 5, *c*, Table 1). The size of the particles is the tenth fractions of a micron.

Using the method of Auger-electronic spectroscopy, the elemental composition and its changes during layer-by-layer ion etching of the dimple surface were analyzed. Figure 6 shows the place of shooting, spectra before and after ion etching, as well as a table with the content of elements calculated by spectra. As is seen, the surface layer contains iron, oxygen and a small amount of aluminium. According to the profile of the element distribution in depth, the width of the layer with the elemental composition different from the base metal was about 50 Å (Figure 7). The results



**Figure 5.** Fracture surface in the OS region (*a, b*), particles on facets of intragranular fracturing (*c*) and results of X-ray microanalysis of chemical composition (at.%)

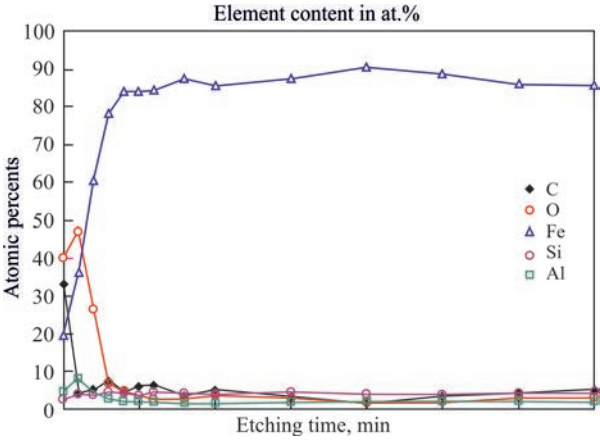




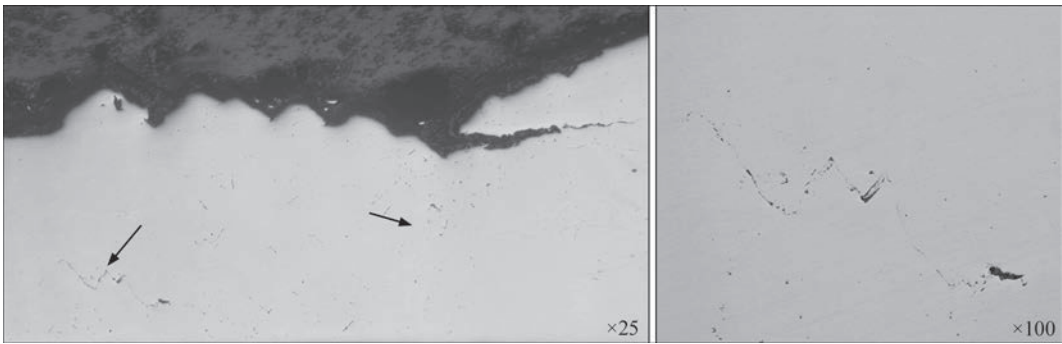
**Figure 6.** Results of Auger-spectral analysis of dimples surface in the OS region (at.%): 1 — before ion etching; 2 — after ion etching

of the examination suggest that opening of metal in the OS region occurs on the oxide film, which is located on the grain boundaries. Apparently, the film is a complex, mainly, iron oxide, with some amount of aluminium oxide.

Therefore, according to the fractographic examinations, on the one hand, the nature of fracture is determined by the microstructure of rail steel, and on the other, by the presence of oxides. Within OS, the determining factor is the oxide film. In the tempering region at a smaller amount of oxide films, microstructure of metal plays a significant role, which provides some plasticity of steel unlike brittle fracturing of a heat-hardened layer.



**Figure 7.** Distribution of elements in depth from the dimple surface in the OS region at an etching rate of 20 nm/min



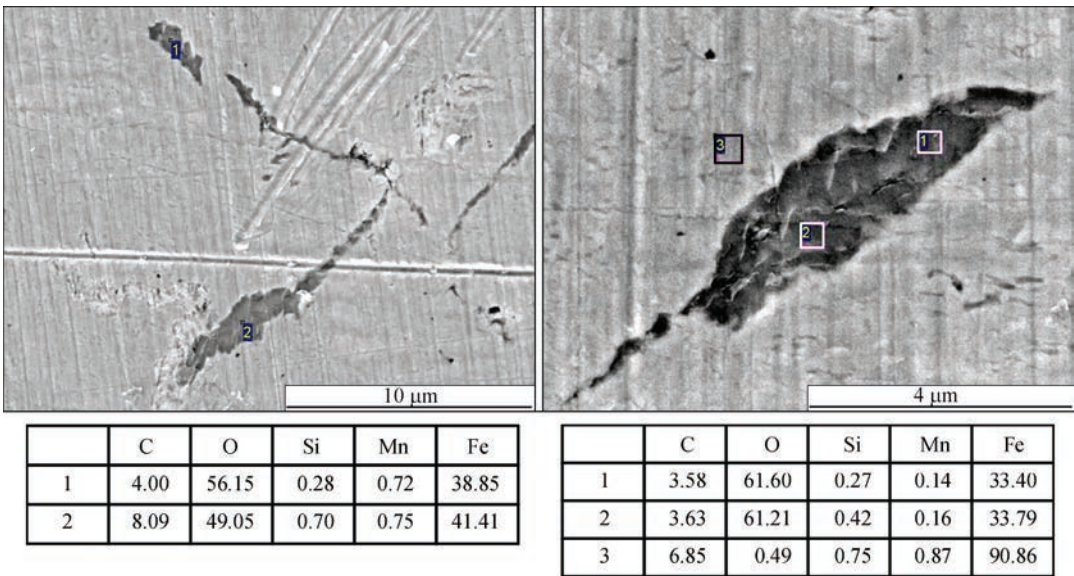
**Figure 8.** Nonmetallic inclusions in the rail metal adjacent to OS

In order to find the origin of oxide films, metallographic examinations of rail metal in the region adjacent to the OS were carried out. Numerous nonmetallic inclusions were found on the polished surface of the cross-section (Figure 8). According to the data of micro X-ray spectral analysis, in the metal, numerous iron oxides (Figure 9) are observed along with the inclusions of complex aluminium, silicon, calcium oxides typical to the converter rail steel. Iron oxides are located mainly on the grain boundaries. Obviously, the presence of a large number of iron oxides is associated with insufficient degree of rail steel deoxidation.

The nonuniform distribution and formation of clusters of iron oxides are caused by the features of ingot crystallization [5]. The impurities partially soluble in iron, including oxygen, are pushed into residual melt. In the places of residual melt crystallization at the structural boundaries, iron oxides are precipitated.

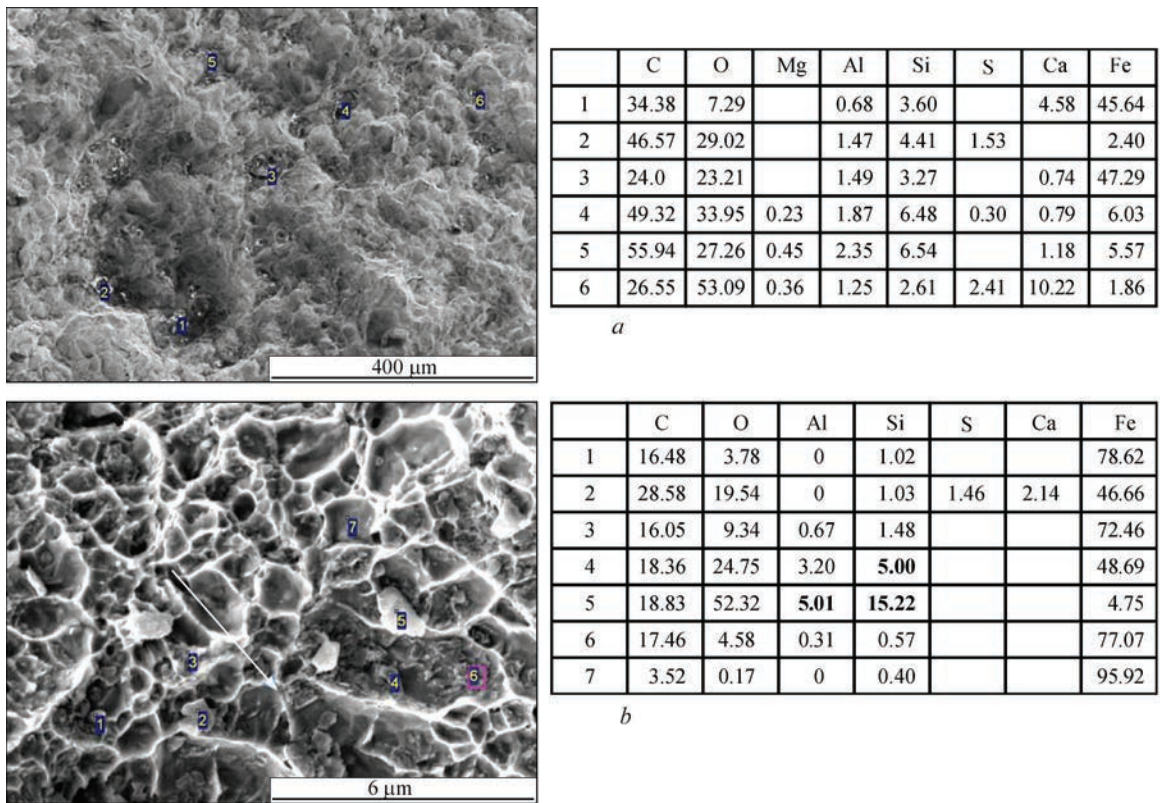
It is known [6] that the Fe–O system is characterized by the presence of FeO oxide (wüstite) with a melting point of 1380 °C. Between iron and wüstite, eutectics is formed at 1368 °C. FeO in the composition of oxide inclusions significantly reduces both their

melting point and ductility [7]. Thus, the FeO–Al<sub>2</sub>O<sub>3</sub> system has eutectics with a melting point of 1329 °C, the FeO–SiO<sub>2</sub>–Al<sub>2</sub>O<sub>3</sub> system has eutectics with a temperature of 1148 °C, the FeO–SiO<sub>2</sub>–CaO system has triple eutectics with a temperature below 1100 °C. Taking into account the level of melting points of the listed oxide systems, it is obvious that the rail steel with insufficient deoxidation level has prerequisites for the formation of oxide films. Thus, the films of iron oxide in the rails (see Figure 1, *a, b*) are probably formed at the stage of blooming production in the crimping shop [8]. During flash-butt welding of rails in thermodeformational conditions of joint formation, the formation of films can propagate. In this case, due to metal deformation, nonmetallic inclusions of aluminium, silicon and calcium oxides interact with iron oxides. As a result, the melting point of oxide films is decreased and the melt ductility is reduced at the ends of the parts. As a result, the OS area found on the fracture surface at a distance of 7 mm from the joint line, is much larger, OS spread to the head surface (Figure 1, *c*) [9]. In the fracture dimples, in this case, the places with numerous aluminium, silicon and calcium oxides of 1 µm were detected (Figure 10), which



**Figure 9.** Results of micro X-ray spectral analysis of nonmetallic inclusions (at.%) in the rail metal adjacent to OS





**Figure 10.** Fracture surface and X-ray microanalysis (at.%) of chemical heterogeneity in the OS region during fracturing of a butt joint at a distance of 7 mm from the joint line

confirms the participation of these oxides in the formation of oxide film.

It is worth noting the difference of OS from the known “matte spots” [9] observed on the fracture surface of the joints of KF76 rails. “Matte spots” is the result of interaction in the near-contact layer of silicon-containing oxide inclusions with the surface-active manganese in iron and a subsequent formation of silicate films [10]. It is known [11], that oxide films negatively affect the properties of steel. Thus, in [12] a decrease in the relative reduction in area of the rail steel metal with insufficient deoxidation is noted. The presence of OS on the fracture surface during static bending tests is the evidence of insufficient deoxidation degree and the factor of reduced steel quality.

**CONCLUSIONS**

1. According to the data of micro X-ray spectral analysis of the fracture surface of the welded butt joints of K76F rails, along with the inclusions of complex oxides of aluminium, silicon and calcium typical for converter rail steel, in the metal, numerous iron oxides are observed, which are located mainly on the grain boundaries. The presence of a large number of iron oxides is associated with insufficient degree of rail steel deoxidation.

2. Fracturing of K76F rails on iron oxide films during static bending tests is a sign of insufficient degree of steel deoxidation and a probable cause of re-

duced service characteristics of rails and their welded butt joints.

**REFERENCES**

1. Botshtein, V. A., Rudyuk, A. S., Chichkarev, E.A. et al. (2013) Mastering of converter rail steel production at PJSC MK Azovstal. *Metall i Litiyo Ukrainy*, 241(6), 34–37 [in Ukrainian].

2. (2016) TU U 27.1-40075815-002:2016: *Rails are new welded for railways*.

3. Kuchuk-Yatsenko, S.I., Didkovsky, O.V., Bogorsky, M.V. et al. (2002) *Method of flash-butt welding*. Pat. 46820 Ukraine, 6 B23K11/04, C2. Publ. 06/17/2002 [in Ukrainian].

4. Kuchuk-Yatsenko, S.I., Didkovsky, O.V., Antipin, Ye.V. et al. (2016) Flash-butt welding of high-strength rails, mining – informatics. *Automation and Electrical Eng.*, 528(4), 40–48.

5. Samoilovich, Yu.A. (1983) *System analysis of ingot crystallization*. Kyiv, Naukova Dumka [in Russian].

6. Barabash, O.M., Koval, Yu.N. (1986) *Crystal structure of metals and alloys: Reference*. Kyiv, Naukova Dumka [in Russian].

7. (1985) *Atlas of slags: Reference*. Ed. by I.S. Kulikova. Moscow, Metallurgiya [in Russian].

8. Levchenko, N.V. (2006) Variation of nonmetallic inclusions during rail production. *Metallurgical and Mining Industry*, 2, 63–65.

9. Kuchuk-Yatsenko, S.I., Shvets, V.I., Didkovsky, A.V., Antipin, E.V. (2016) Effect of non-metallic inclusions of rail steel on welded joint formation. *The Paton Welding J.*, 5–6, 24–28. DOI: <https://doi.org/10.15407/tpwj2016.06.04>

10. Shvets, V.I., Ziakhor, I.V., Kapitanchuk, L.M. (2023) Features of formation and transformation of oxides in flash-butt welding of K76F rails. *The Paton Welding J.*, 7, 16–24. DOI: <https://doi.org/10.37434/tpwj2023.07.02>

11. Gubenko, S.I. (2015) *Nonmetallic inclusions and strength of steels*. Palmarium Academic Publ.
12. Trotsan, A.I., Kaverinsky, V.V., Koshule, I.M., Nosochenko, A.O. (2013) On the factors influencing the quality of rail steel and rails. *Metall i Litiyo Ukrainy*, 241(6), 9–14.

**ORCID**

V.I. Shvets: 0000-0003-4653-7453,  
I.V. Ziakhor: 0000-0001-7780-0688,  
O.V. Didkovskiy: 0000-0001-5268-5599,  
E.V. Antipin: 0000-0003-3297-5382

**CONFLICT OF INTEREST**

The Authors declare no conflict of interest

**CORRESPONDING AUTHOR**

I.V. Ziakhor  
E.O. Paton Electric Welding Institute of the NASU  
11 Kazymyr Malevych Str., 03150, Kyiv, Ukraine.  
E-mail: zyakhor2@ukr.net

**SUGGESTED CITATION**

V.I. Shvets, I.V. Ziakhor, L.M. Kapitanchuk,  
O.V. Didkovskiy, E.V. Antipin (2024) Peculiarities  
of fracture of welded joints of railway rails  
of oxygen-converter K76F steel. *The Paton Welding  
J.*, 5, 3–10.

**JOURNAL HOME PAGE**

<https://patonpublishinghouse.com/eng/journals/tpwj>

Received: 07.03.2024

Received in revised form: 09.04.2024

Accepted: 27.05.2024





# THERMOMECHANICAL PROCESSES IN FRICTION STIR WELDING OF MAGNESIUM ALLOY SHEETS

**M.A. Khokhlov<sup>1</sup>, O.O. Makhnenko<sup>2</sup>, V.A. Kostin<sup>1</sup>, A.G. Pokliatskyi<sup>1</sup>,  
Iu.V. Falchenko<sup>1</sup>, Yu.A. Khokhlova<sup>1</sup>**

<sup>1</sup>E.O. Paton Electric Welding Institute of the NASU  
11 Kazymyr Malevych Str., 03150, Kyiv, Ukraine

<sup>2</sup>Kyiv Academic University  
36 Acad. Vernadskyi Str., 03142, Kyiv, Ukraine

**ABSTRACT**

Experimental laboratory equipment for friction stir welding (FSW) as a result of working out the optimal welding modes at different linear velocities allows producing high-quality butt joints from thin ductile metals. With the development of new mathematical methods for modeling thermodeformational processes, it became possible to analyze the stress-strain state and thermomechanical processes occurring in the FSW joint zone, which is necessary for predicting the operational properties, strength and service life of welded structures made of thin metal. Using mathematical models and finite element analysis, the temperature distributions from the volume heat source at FSW were visualized, and the residual deformations and stresses in the zone of butt-welded joints of thin sheets of magnesium alloys were numerically determined. In the future, it is advisable to determine the effective balance of the linear speed and the rotation speed of the FSW tool to obtain better homogeneity of the weld structure and reduce heat input into the metal during welding.

**KEYWORDS:** magnesium alloys, friction stir welding, microstructure, modulus of elasticity, temperature distributions, residual stresses, plastic deformations

**INTRODUCTION**

Magnesium has high specific strength, high rigidity and damping characteristics, absolute biological compatibility that is why it is included into the top ten of innovative future materials for application in structural elements of aerospace engineering, cars, sports equipment, microelectronics, and in surgical implants [1–3]. The ratio of strength to weight of magnesium alloy parts makes them one of the many important materials, which will replace aluminium and will be used in automotive industry in the coming years to lower the force of inertia and for the benefit of productivity, controllability and fuel saving. A large part of investigations on magnesium alloys weldability considers the experience of application of environmentally-friendly and energy-efficient technology — friction stir welding (FSW) used for solid-phase joining of parts of relatively simple geometry. Statistically successful is the experience [4] of application of a tool in the form of a smooth pin with a concave shoulder at FSW, as it allows avoiding deformation when joining lightweight and ductile alloys; the welds form without cavities and contain locally strengthened zones along the lower contour of the weld nugget [5, 6]. An idea

for the subsequent experiments was mathematical modeling of temperature and deformation processes at FSW using fundamental regularities [7–11]. Such a complex approach at evaluation of the quality of welded joint formation is developed for further application in statistical scaled models for prediction of service properties, strength and service life of welded structures from thin magnesium alloys.

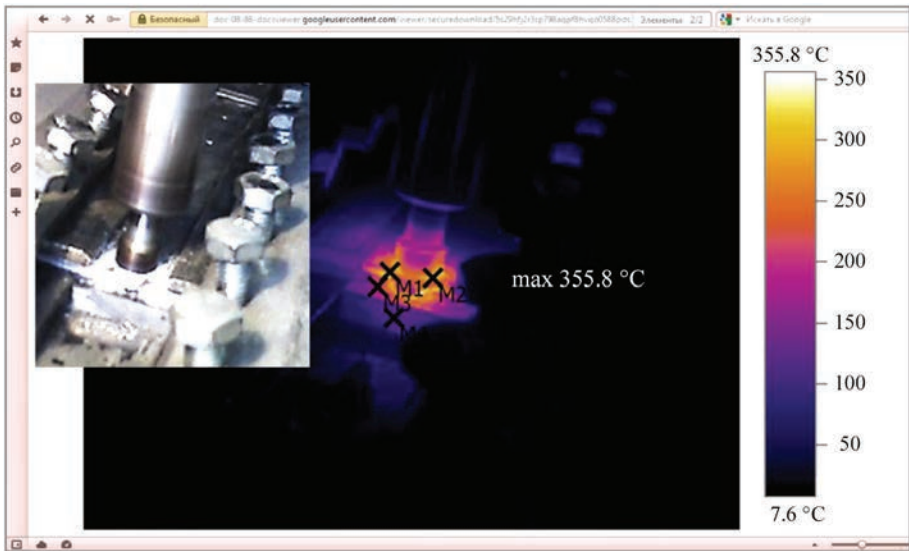
The objective of this study is producing sound FSW butt joints of magnesium alloy at a constant speed of the tool rotation and at different linear welding speeds, determination of physical-mechanical parameters of the material in FSW zone by the indentation method, as well as experimental measurement of surface temperature fields at FSW, determination of the temperature fields by mathematical modeling methods, distribution of strains and residual stresses in FSW butt joints.

**MATERIALS AND METHODS  
OF INVESTIGATION**

Welding of butt joints of 2 mm sheets of MA2-1 magnesium alloy of Mg–Al–Zn system (Table 1) was performed in experimental welding equipment for FSW

**Table 1.** Chemical composition of MA2-1 magnesium alloy, wt. %

Fe	Si	Mn	Ni	Al	Cu	Be	Mg	Zn	Others
0.04	0.1	0.3–0.7	0.004	3.8–5.0	0.05	0.002	92.6–95.1	0.8–1.5	0.3



**Figure 1.** Thermogram of the temperature field at FSW of butt joint of 2 mm magnesium alloy (Fluke Ti25)

at a constant frequency of tool rotation of 1420 rpm and at different linear speeds (8, 16, 24 m/h).

Comparative evaluation of the temperature fields at FSW was performed by experimental infrared thermal imager Fluke Ti25 (Figure 1) and COMSOL Multiphysics was used for modeling the kinetics of temperature field change during FSW process.

In order to determine the features of macro- and microstructure by the method of optical microscopy and of physical-mechanical properties by indentation method, welded joint microsections were made and treated by the water solution of a mixture of 5 % hydrochloric acid and 5 % orthophosphoric acid. Experimental determination of the Young’s modulus by indentation was conducted to more precisely determine the data, which were used for modeling of welding. Indentation at 100 g load with automatic determination of the modulus of elasticity (*E*) was conducted by triangular Berkovich indenter in a computerized “Mikron-Gamma” instrument in keeping with ISO/FDIS 14577–2015; Metallic materials — Indentation test for hardness and materials parameters [12–14] (measurement of hardness value which the test allows determining, was not performed in this work). Macrostructural studies were conducted with an optical binocular (40–100 magnification), microstructural studies and navigation at indentation were

performed using the instrument microscope and digital video camera for DCM500 microscopes. Investigations of the level of microstructure dispersity were conducted by scanning electron microscopy (SEM) in JSM-840 (JEOL, Japan) in secondary electron mode (SEI) at 20 kV accelerating voltage and probe current of 10<sup>−7</sup> A. The electron microscope is fitted with a combined system of energy-dispersive microanalysis INCA PentaFet (INCA, England) and digital image recording system Scan Micro Capture 2.1.

In the methodology [9] of numerical analysis of the thermodeformational processes at FSW the equation of nonstationary heat conductivity is used to determine the kinetics of temperature distributions,

$$\frac{\partial}{\partial x}\left(\lambda \frac{\partial T}{\partial x}\right)+\frac{\partial}{\partial y}\left(\lambda \frac{\partial T}{\partial y}\right)+\frac{\partial}{\partial z}\left(\lambda \frac{\partial T}{\partial z}\right)+W(x,y,z,t)=\rho c \frac{\partial T}{\partial t}, \tag{1}$$

which allows for the power of volume heat release *W*(*x*, *y*, *z*, *t*); *ρ* is the material density; *c* is the specific heat; *λ* is the coefficient of thermal conductivity; *T* is the material temperature (Table 2).

Boundary conditions on the joint surfaces, taking into account the convective heat exchange with the environment:

$$q=-h(T_{\text{out}}-T), \tag{2}$$

**Table 2.** Thermal-physical properties of MA2-1 magnesium alloy (*T*<sub>m</sub> = 650 °C)

<i>T</i> , °C	Density, kg/m <sup>3</sup>	Young’s modulus of elasticity, GPa	Yield limit, MPa	Heat conductivity coefficient λ, W/m·°C	Specific heat conductivity <i>S</i> , J/(cm·°C)
20	1785	42	140	1.02	1.80
100	1785	40	137	1.07	1.86
200	1761	37	134	1.12	1.92
300	1746	35	129	1.18	1.98
400	1730	32	88	1.23	2.04
500	1714	29	63	1.25	2.13



where  $T_{out}$  is the ambient temperature;  $q$  is the heat flux;  $h$  is the coefficient of heat transfer from the surface ( $h = 10 \text{ W/m}^2\cdot^\circ\text{C}$ ).

Power of heat release at FSW

$$W(x, y, z, t) = \mu P_n \omega r, \quad \text{at } z = 0, R1 < r < R2 \quad (3)$$

(on the upper surface in the tool shoulder zone),

at  $0 < z < \delta$ ,  $r = R1$  (across the thickness in the tool pin zone), where  $\mu$  is the friction coefficient;  $P_n$  is the normal force in the contact zone;  $\omega$  is the angular velocity of the tool rotation;  $r = \sqrt{(x - x_0)^2 + (y - y_0)^2}$  is the distance of the contact point from the tool rotation axis ( $x_0, y_0$ );  $R1$  is the pin radius;  $R2$  is the shoulder radius;  $\delta$  is the thickness of the plate being welded.

In the elastoplastic definition the strain tensor

$$\varepsilon_{ij} = \varepsilon_{ij}^e + \varepsilon_{ij}^p \quad (i, j = x, y, z), \quad (4)$$

where  $\varepsilon_{ij}^e$  is the tensor of elastic deformations;  $\varepsilon_{ij}^p$  is the tensor of plastic deformations. The components of tensors of stresses  $\sigma_{ij}$  and elastic deformations  $\varepsilon_{ij}^e$  are connected to each other by Hooke's law:

$$\varepsilon_{ij}^e = \frac{\sigma_{ij} - \delta_{ij}\sigma}{2G} + \delta_{ij}(K\sigma + \varphi) \quad (5)$$

where  $\delta_{ij}$  is the unit tensor;  $\sigma = \frac{1}{3}(\sigma_{xx} + \sigma_{yy} + \sigma_{zz})$ ,

$G = \frac{E}{2(1+\nu)}$  is the shear modulus;  $K = \frac{1-2\nu}{E}$  is the

volumetric compression compliance;  $E$  is the Young's modulus;  $\nu$  is the Poisson's ratio;  $\varphi$  is the function of free relative elongations (volumetric changes) caused by temperature change:

$$\varphi = \alpha(T - T_0), \quad (6)$$

where  $\alpha$  is the coefficient of relative temperature elongation of the material.

Plastic deformations are associated with the stressed state by the equation of the theory of plastic nonisothermal flow, associated with von Mises yield condition. Iteration processes are used to solve the problem with physical nonlinearity, associated with development of plastic deformations.

The developed mathematical model allows determination of residual welding stresses and deformations in the zone of FSW butt joint, as a result of non-uniform temperature heating, because of mechanical friction of the tool against the plate material during welding. The mathematical model can be efficient for prediction of general deformations of large-sized structures with a large number of welded joints. In order to simplify the model, the following aspects were not taken into account: dependence of friction

coefficient on material temperature, heating and heat removal to the work tool and fixtures.

Mathematical modeling of FSW process was conducted on 2 mm magnesium alloy plates at a constant speed of the tool rotation of 1420 rpm, and for different linear welding speeds of 8, 16, 24 m/h, using a specialized proprietary program of finite element analysis.

## RESULTS

At optical examination of the macrostructure of a set of 6 samples, produced at different linear welding speeds (Figure 2), it was determined that all of them have similar and typical for FSW asymmetrical weld shape with zones of metal advancing (AS) and retreating (RS), and sound zone of intensive plastic deformation without cavities. Weld width is approximately 10 mm.

Thermodynamic processes at FSW form a clear boundary between the weld nugget and TMAZ at the retreating size (RS) (Figure 3, a). Basic magnesium alloy of Mg–Al system has a rolled structure with an elongated grain (Figure 3, b). TMAZ structure along AS has horizontal bands of metal flow diffusion from initial rotation of FSW tool with a microstructure similar to that of base metal (Figure 3, c). Increase of weld metal ductility from heating at torsional deformation leads to elongation and compression of metal grain boundaries, and further on to local extrusion and recrystallization. Here, fine round grains of 1–10  $\mu\text{m}$  size are formed (Figure 3, d and Figure 4).

From the fundamental viewpoint, in Mg–Al chemical system, which was exposed to intensive deformation, formation of distribution phases, which consist of Mg-rich and Al-rich regions, is possible in the range of 550–640  $^\circ\text{C}$ . Such a temperature ensures a high mobility of the atoms, and promotes growth of the grains of dimensions from 50 up to 500 nm due to diffusion and recrystallization. At mixing of the zones with high and low temperature, this recrystallization occurs with increase of dislocation density on the grain and subgrain boundaries. So-called Lomer–

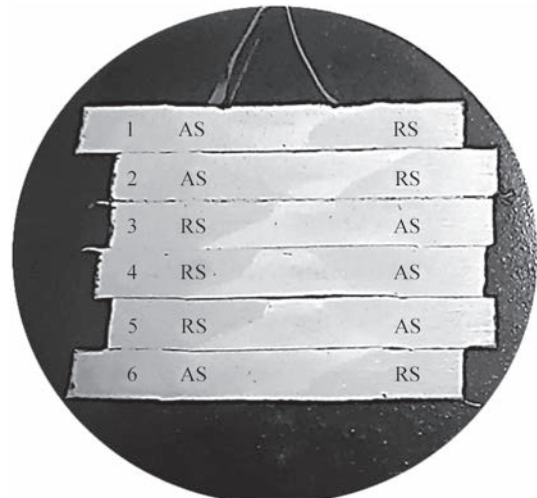
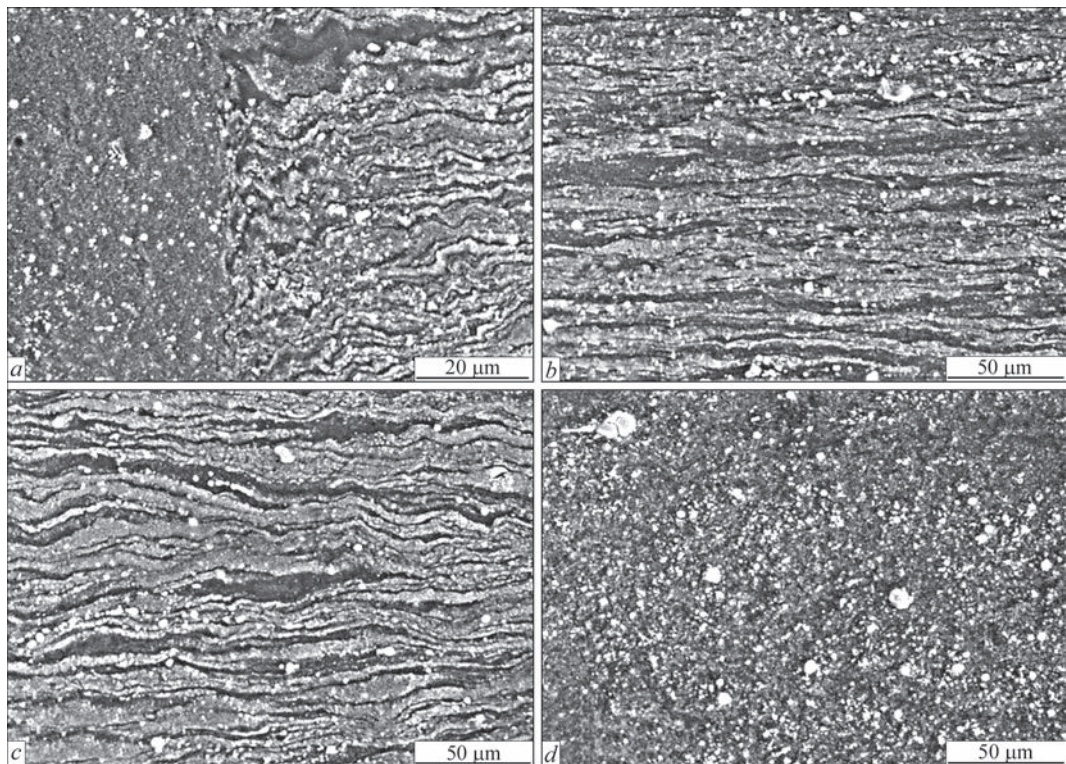


Figure 2. Macrostructure of FSW butt joints



**Figure 3.** Microstructure of FSW weld on the retreating side (RS) – base metal (b), HAZ–TMAZ–weld nugget (c) and weld nugget middle (d) REM

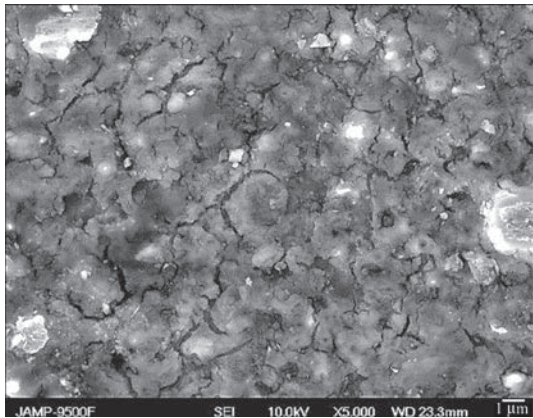
Cottrell barriers are formed, which stop dislocation sliding because of formation of thresholds on them as a result of mutual intersection. Furtheron, they inhibit generation of new dislocations. Thus, the more difficult it is for dislocations to move in the material, the stronger is the strain hardening. Usually, formation of a fine sound structure at FSW takes place with the participation of several mechanisms simultaneously, and the result depends on the welding conditions, chemical composition of the material and other factors.

The modulus of elasticity ( $E$ ) was determined for 5 types of textures of the zone of the joint — base metal, TMAZ, top, bottom and center of the nugget (Figure 5). In the nugget central part  $E = 30$  GPa, this zone contains an ellipsoidal structure (Figure 6) and elongated from pressing and tool rotation textures in the weld upper and lower parts. For the weld up-

per part  $E = 36$  GPa. The highest value  $E = 90$  GPa was determined in the nugget at the distance of 50–150 μm along the sample lower edge. That is, elasticity is increased 2 – 3 times, compared to base metal, where  $E = 35$  GPa. For TMAZ modulus of elasticity is  $E = 30$  GPa.

Comparison of the shape and depth of indentation diagrams shows a more ductile state of the base metal (Figure 7, a), and in the nugget zone below the intersection midpoint the elastic reaction of the material surface is increased (Figure 7, b). The depth of the indenter immersion into the base metal is greater, and it is equal to 7.57 μm, and in the nugget zone below the intersection midpoint it is equal to 5.44 μm. As such a significant inhomogeneity of the texture of FSW joint zones creates a high level of elastically deformed state in the thin metal, it ensures the traditional statistics of fracture through TMAZ at tensile strength testing. Therefore, additional heat treatment is usually recommended, after which the state can be normalized by approximately 10 % [15].

By experimental thermogram of the welding process recorded by the thermal imager, it was approximately determined that the temperature of external surface of the magnesium alloy and tool at FSW is not higher than 355.8 °C. The model of the temperature fields at the specified welding parameters (Figure 8) shows similar temperature at a small distance from the point of contact of cylindrical FSW tool with the metal, and after passing of FSW tool the temperature is at the level of 410 °C. In the zone, where a refined



**Figure 4.** Fine grains in the nugget zone (SEM)



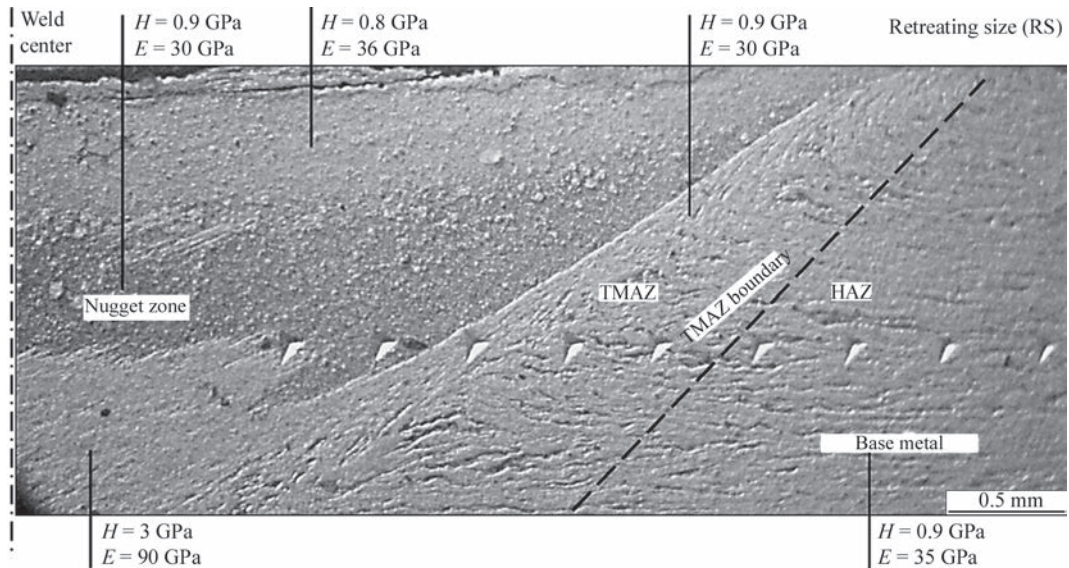


Figure 5. Distribution of hardness and Young's modulus of elasticity in FSW joint from RS

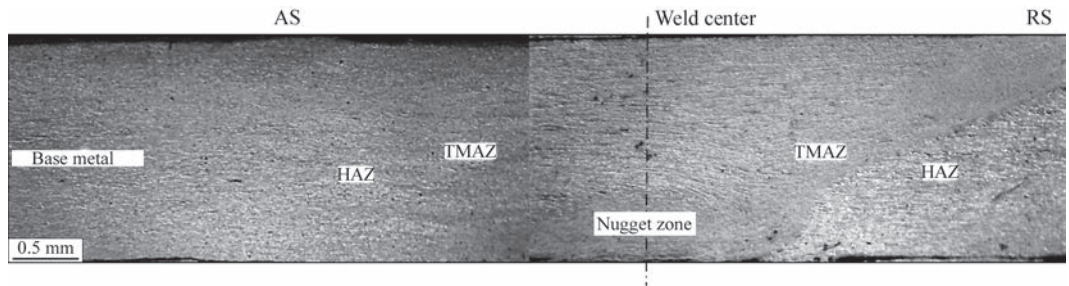


Figure 6. Microstructure of the central part of FSW with indenter imprints

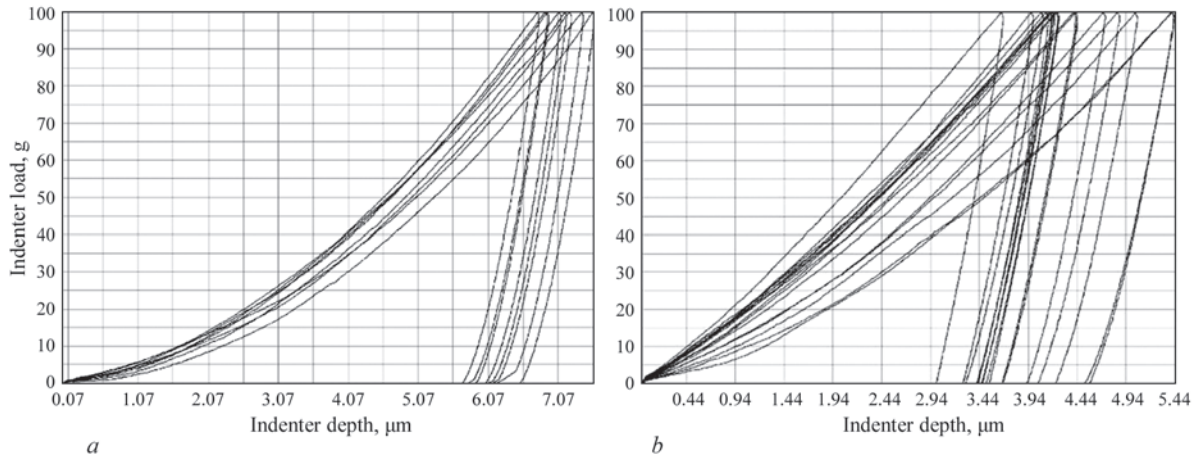


Figure 7. Diagram of indentation of base metal (a) and weld nugget (b)

structure forms with 2–3 times increase of elasticity, the temperature is equal to 500 °C.

In keeping with the thermal cycle (Figure 9, a), heating to the temperature of 600–610 °C, at which the welded joint forms, is not essentially dependent on linear speed of FSW tool advancing. The width of the temperature field of FSW joint zone (Figure 9, b) is reduced with increase of the linear speed, and it is equal to 8, 6 and 4 mm, for linear speeds of 8, 16 and 24 m/h, respectively.

The width of the weld on experimentally produced samples of FSW joints at linear welding speed of

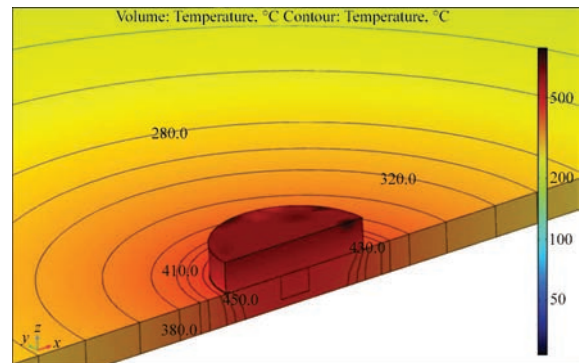
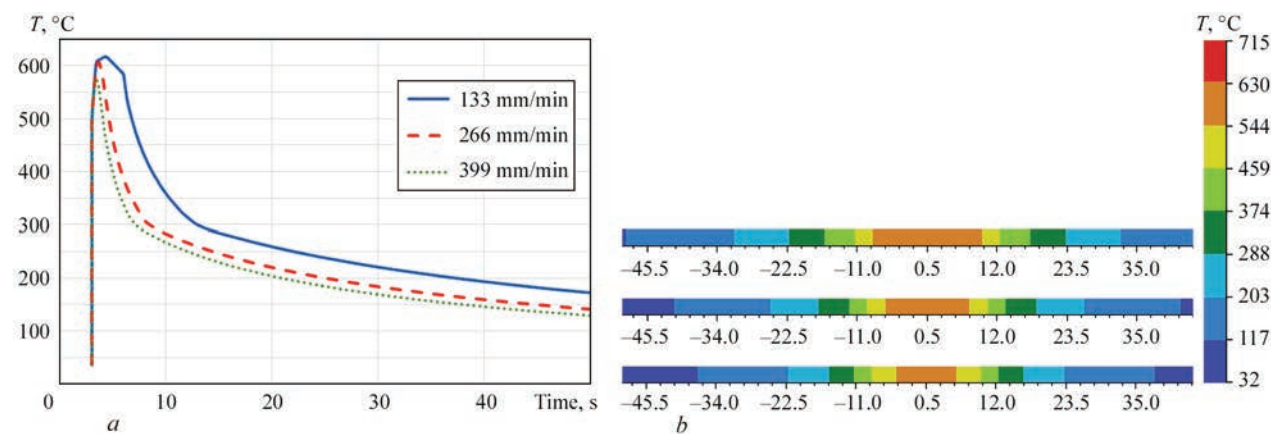
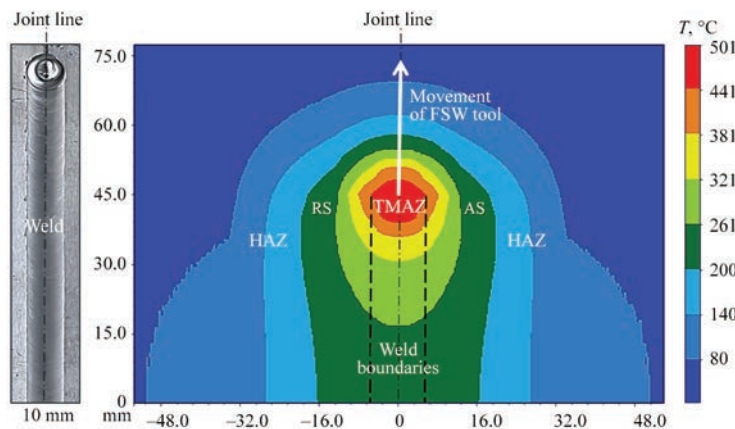


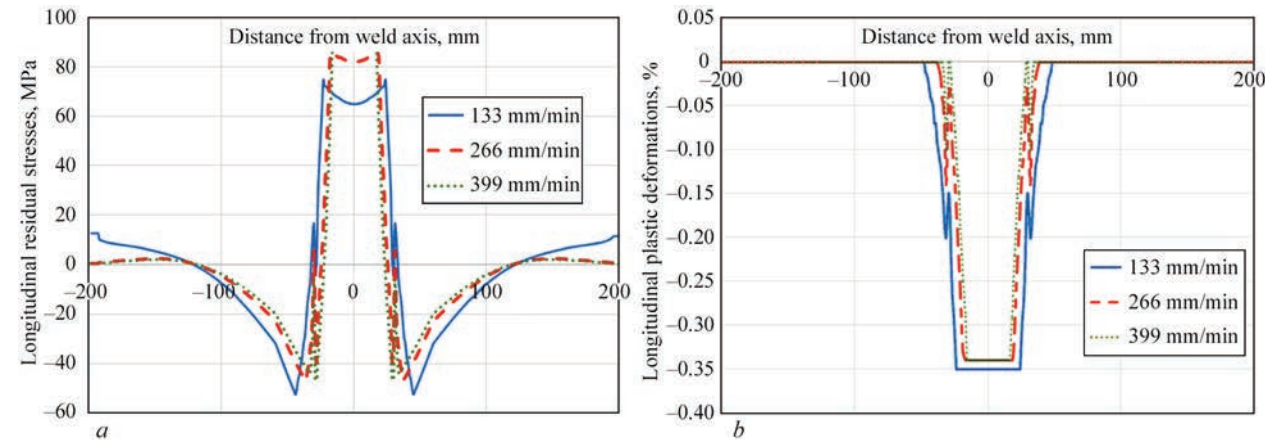
Figure 8. Model of temperature fields of FSW process



**Figure 9.** Distribution of thermal cycles (*a*) and temperature fields (*b*) at FSW of 2 mm plates from a magnesium alloy at different linear welding speeds



**Figure 10.** TMAZ width at linear speed of 8 m/h in the sample and model



**Figure 11.** Distribution of longitudinal residual stresses (*a*) and plastic deformations (*b*) in the butt joint of 2 mm plates from a magnesium alloy at different FSW linear speeds

8 m/h is equal to approximately 10 mm (Figure 10) is presented in the calculation data by a similar value.

Calculations of maximal residual tensile stresses showed that they reach the material yield limit of 140 MPa (Figure 11, *a*). The level of maximal calculated residual plastic shrinkage deformations is relatively low — up to 0.35 % (Figure 11, *b*). At increase of linear welding speed, maximal residual tensile stresses increase by 10–15 %, which is related to increase of temperature gradient during welding. It was also established that residual plastic deforma-

tions (longitudinal) demonstrate a slight lowering of the level with increase of the linear welding speed.

### CONCLUSIONS

Sound welded joints of thin sheets of magnesium alloy are produced at a constant frequency of FSW tool rotation of 1420 rpm and linear welding speeds of 8, 16, 24 m/h. A clearcut textured boundary between the weld nugget and TMAZ forms on the metal retreating side; weld nugget contains a refined ellipsoidal structure with 2–3 times increase of the modulus of elastic-



ity, compared to the base metal. The calculated temperature field which characterizes the FSW process, correlates with experimentally determined surface temperature and has a maximal temperature at the level of 600 °C in the nugget zone, i.e. the metal in the joint zone is in the ductile state. Modeling of the kinetics of temperature field change during FSW shows that the HAZ width decreases with increase of the linear speed. It is found that at higher linear welding speed the maximal residual stresses are increased by 10–15 %. Residual plastic deformations are decreased at increase of the linear welding speed. To produce a uniform structure of FSW weld of thin sheets of the magnesium alloy, lowering of the heat input into the metal due to increase of FSW linear speed or lowering of the speed of FSW tool rotation can be effective, i.e. it is rational to further on determine the balance of linear speed and rotation speed of FSW tool.

## REFERENCES

1. Yan Yanga, Xiaoming Xionga, Jing Chen et al. (2023) Review. Research advances of magnesium and magnesium alloys worldwide in 2022. *J. of Magnesium and Alloys*, **11**, 26112654. DOI: <https://doi.org/10.1016/j.jma.2023.07.011>
2. Jiangfeng Song, Jing Chen, Xiaoming Xiong et al. (2022) Research advances of magnesium and magnesium alloys worldwide in 2021. *J. of Magnesium and Alloys*, **10**(4), 863–898. DOI: <https://doi.org/10.1016/j.jma.2022.04.001>
3. Kostin, V.A., Falchenko, Yu.V., Puzrin, A.L., Makhnenko, A.O. (2023) Production, properties and prospects of application of modern magnesium alloys. *Suchasna Elektrometalurhiya*, **1**, 43–52. DOI: <https://doi.org/10.37434/sem2023.01.06> [in Ukrainian].
4. Poklyatskyi, S.I., Motrunich, S.I., Fedorchuk, V.E., Klochkov, I.M. (2023) Strength and structure of butt, overlap and fillet joints of AMg6M alloy produced by friction stir welding. *The Paton Welding J.*, **2**, 10–17. DOI: <https://doi.org/10.37434/tpwj2023.02.02>
5. Krasnowski, K. et al. (2021) Relation between geometry of FSW tools and formation of nano-dispersed zones in macro-structure EN AW 6082-T6 alloy welded joints. *Biuletyn Instytutu Spawalnictwa w Gliwicach*, **65**(5), 7–16. DOI: <https://doi.org/10.17729/ebis.2021.5/1>
6. Krasnovsky, K., Khokhlova, Yu.A., Khokhlov, M.A. (2019) Influence of tool shape for friction stir welding on physico-mechanical properties of zones of welds of aluminium alloy EN AW 6082-T6. *The Paton Welding J.*, **7**, 7–11. DOI: <http://dx.doi.org/10.15407/tpwj2019.07.02>
7. Tsaryk, B.R., Muzhychenko, O.F., Makhnenko, O.V. (2022) Mathematical model of determination of residual stresses and strains in friction stir welding of aluminium alloy. *The Paton Welding J.*, **9**, 33–40. DOI: <https://doi.org/10.37434/tpwj2022.09.06>
8. Asadi et al. (2015) Microstructural simulation of friction stir welding using a cellular automaton method: A microstructure prediction of AZ91 magnesium alloy. *Inter. J. of Mechanical and Materials Eng.* DOI: <https://doi.org/10.1186/s40712-015-0048-5>
9. Makhnenko, O.V., Kandala, S.M., Basystyuk, N.R. (2021) Influence of heat transfer factor on level of residual stresses after heat treatment of reflection shield of WWER-1000 reactor. *Mech. Adv. Technol.*, **5**(2), 254–259. DOI: <https://doi.org/10.20535/2521-1943.2021.5.2.245074>
10. Makarenko, A.A., Makhnenko, O.V. (2022) Mathematical modeling of residual stresses in composite welded joints of WWER-1000 reactor vessel cover with CSS nozzles. *The Paton Welding J.*, **1**, 33–40. DOI: <https://doi.org/10.37434/tpwj2022.01.07>
11. Dutka, V.A., Maistrenko, A.L., Zabolotnyi, S.D., Stepanets, A.M. (2023) Prediction of thermal state of tool from superhard materials in friction stir welding of heat-resistant alloys. *Instrumentalne Materialoznavstvo: Transact.*, Issue 26, Kyiv, ISM, 295–305 [in Ukrainian].
12. Khokhlova, Yu.A., Ishchenko, D.A., Khokhlov, M.A. (2017) Indentation from macro- to nanometer level and examples of investigation of properties of materials with a special structure. *Tekh. Diahnost. ta Neruiniv. Kontrol*, **1**, 30–36. DOI: <https://doi.org/10.15407/tdnk2017.01.05> [in Ukrainian].
13. Oliver, W.C., Pharr, G.M. (1992) An improved technique for determining the hardness and elastic modulus using load displacement sensing indentation experiments. *J. Mater. Res.*, **7**, 1564–1583. DOI: <https://doi.org/10.1557/JMR.1992.1564>
14. Kazuhisa Miyoshi (2002) NASA/TM-2002-211497: *Surface characterization techniques: An overview*. 12–22. <http://ntrs.nasa.gov/archive/nasa/casi.ntrs.nasa.gov/20020070606.pdf>
15. Kulwant Singh, Gurbhinder Singh, Harmeet Singh (2019) Microstructure and mechanical behaviour of friction-stir-welded magnesium alloys: As-welded and post weld heat treated, 20, September 100600. DOI: <https://doi.org/10.1016/j.mt-comm.2019.100600>

## ORCID

M.A. Khokhlov: 0000-0002-8180-3459,  
V.A. Kostin: 0000-0002-2677-4667,  
A.G. Pokliatskyi: 0000-0002-4101-2206,  
Iu.V. Falchenko: 0000-0002-3028-2964,  
Yu.A. Khokhlova: 0000-0002-2145-973X

## CONFLICT OF INTEREST

The Authors declare no conflict of interest

## CORRESPONDING AUTHOR

Yu.A. Khokhlova  
E.O. Paton Electric Welding Institute of the NASU  
11 Kazymyr Malevych Str., 03150, Kyiv, Ukraine.  
E-mail: [khokhlova.julia@gmail.com](mailto:khokhlova.julia@gmail.com)

## SUGGESTED CITATION

M.A. Khokhlov, O.O. Makhnenko, V.A. Kostin, A.G. Pokliatskyi, Iu.V. Falchenko, Yu.A. Khokhlova (2024) Thermomechanical processes in friction stir welding of magnesium alloy sheets. *The Paton Welding J.*, **5**, 11–17.

## JOURNAL HOME PAGE

<https://patonpublishinghouse.com/eng/journals/tpwj>

Received: 07.03.2024

Received in revised form: 16.04.2024

Accepted: 31.05.2024

# CONSUMABLE AND NONCONSUMABLE ELECTRODE WELDING OF HIGH-STRENGTH 2219-T31 ALUMINIUM ALLOY

**T.M. Labur, A.G. Pokliatskyi, V.A. Koval**

E.O. Paton Electric Welding Institute of the NASU  
11 Kazymyr Malevych Str., 03150, Kyiv, Ukraine

## ABSTRACT

The influence of the conditions of nonconsumable (TIG) and consumable (MIG) electrode arc welding of high-strength aluminium alloy of 2219-T31 grade (USA) 5 mm thick was studied. Effective welding modes were selected by the main characteristics: absence of coarse defects, weld form factor, standard mechanical properties, and features of fracture surface relief. The strength level of welded joints after welding is 25–30 % lower compared to base metal ( $\sigma_t = 366\text{--}370$  MPa). The impact toughness values of the welds after TIG welding vary from 16.4 to 20.3 J/cm<sup>2</sup>, according to the rolling direction. Bend angle is almost 3 times lower than the base metal value (180 and 177°). Fracture of joints with technological reinforcement and of the weld root occurs along the boundary of weld fusion with the base metal, and at a distance from the surface — along the weld axis. The relief retains a predominantly cellular structure. Analysis results were used to establish the technological conditions of achieving an optimal quality of welds and the type of shielding gas for welding.

**KEYWORDS:** aluminium alloy, nonconsumable and consumable electrode welding modes, inert gases: argon, helium, welded joints, mechanical properties, investigations

## INTRODUCTION

The main requirement in ensuring the reliability and performance of the structure is the weld quality. Analysis of standard welding technologies, widely used in fabrication of lightweight structures, shows that, in addition to selection of the welding process, its cost, the degree of processing and mastering in production the normative documents, required to reproduce the technologies under shop conditions, is also taken into account. Here, greater attention is paid to technological convenience of the process in the shop. However, the arc phenomena, deposition rate, as well as the possibility of precise control of the process remain to be the decisive factors for improvement of the efficiency of application of the selected arc welding technology. Certainly, saving on structural materials cost and energy consumption, as well as the possibility of process robotization are taken into account. The above requirements are now considered as key ones to increase the efficiency of welded structure fabrication, ensuring the conditions for reproducible quality of welds, saving the expenses and possibility of working without human intervention [1–3].

Nonconsumable (TIG) and consumable (MIG) electrode welding in different shielding gases (argon and helium), plasma-arc and hybrid joining processes are the most in demand for fabrication of lightweight structures from aluminium alloys [4–6]. The first technology is realized at a low speed, which is due to the mechanism of wire feed into the metal pool. With this

method, a good formation of the welds is observed, as the arc is burning in a stable manner even at a low electric current density [4, 5]. Pulsed modes ensure intensive refinement of oxide inclusions at simultaneous degassing of the welds, and promote their wide acceptance in structure fabrication [2]. Plasma-arc welding method allows producing a sound joint of thin sheets, but this process remains to be costly, and it does not demonstrate any flexibility in manufacture [1]. Low heat input at MIG improves the efficiency of welding parts and components from aluminium alloys, and the process lends itself easily to automation and integration into the production line [1]. The main disadvantage of this technology remains to be a process of electrode metal heating insufficiently stable in time and space, as the arc length and position of its spot on the surface change alternately. It influences the mechanism of formation of molten metal drop, its size and nature of transition into the weld pool to fill the gap between the parts [3]. In addition, it influences the type of shielding atmosphere — argon or helium (Figure 1). Gas replacement increases the ability of the arc to penetrate the metal, input energy value, and the number of electrode drops decrease 1.5–2 times, average pool temperature, duration of its existence and degree of its degassing are increased. On the other hand, evaporation of volatile elements is decreased, and no pores form at the liquid drop stage [4].

Aluminium alloy of 2219 grade of Al–Cu–Mn (6.8 % Cu–0.32 % Mn–0.16 % Zr) alloying system belongs to the class of heat-hardenable and has a high



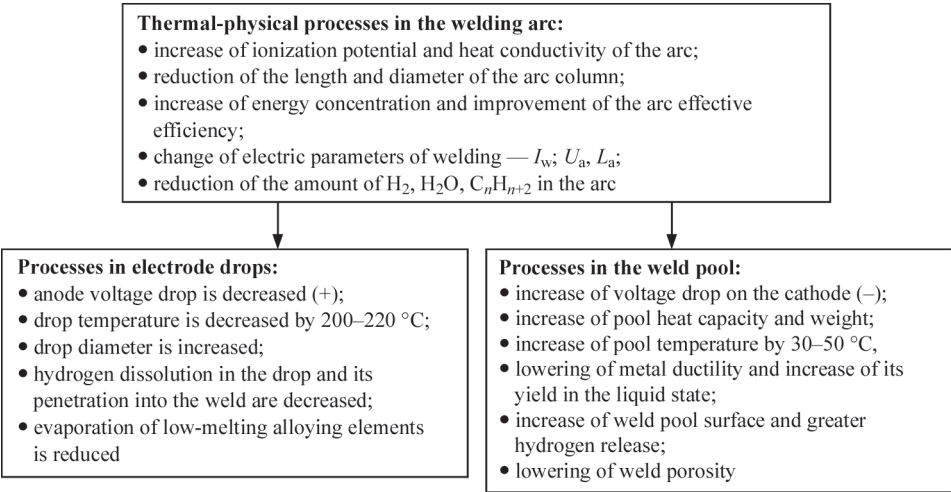


Figure 1. Thermal-physical processes arising in the arc, electrode metal drops, and in the weld pool at argon replacement by helium

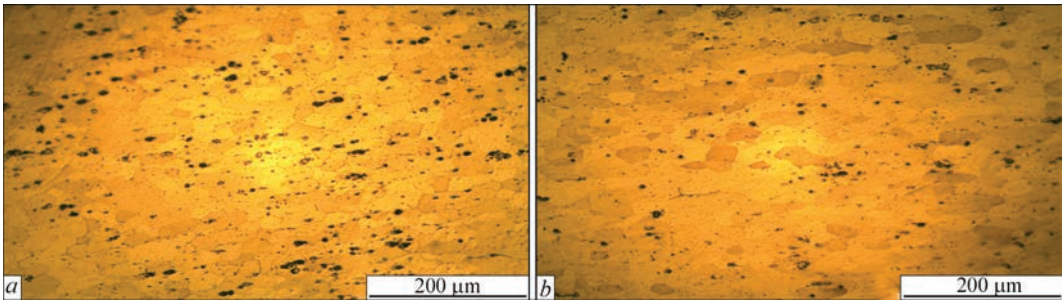


Figure 2. Microstructure of 2219-T31 alloy 5 mm thick along (a) and across (b) the rolling direction

specific heat [3]. High technological plasticity in the cold and hot state and adequate cold resistance distinguish it among the other alloys [4]. Under the conditions of superlow temperatures, including the temperature of –269 °C, the alloy strength and ductility become higher, making 2219 alloy unique for products, exposed to a broad temperature range in service [1]. A good combination of technological and physical-mechanical properties (Table 1) makes it highly popular in aerospace industry, as well as in structures of cylinders and tanks for liquid gas storage.

The above-mentioned technological and service properties are achieved due to the main alloying elements of 221-T31 alloy, namely copper and manganese. The alloy microstructure consists of aluminium-rich  $\alpha$ -phase (solid solution) and stable  $\theta$ (CuAl<sub>2</sub>)-phase (Figure 2). Intermediate phases include  $\theta'$ (CuAl<sub>2</sub>) and  $S'$ (Al<sub>2</sub>CuMg), and presence of  $\theta$ (Al<sub>2</sub>Cu),  $T$ (Al<sub>12</sub>Mn<sub>2</sub>Cu), Al<sub>3</sub>Zr and Al<sub>11</sub>V phases provides the respective level of physical-mechanical properties both of the alloy proper, and of its welded joints. Semi-finished products are supplied to the

manufacturer in the annealed (0), hardened and naturally aged (T3) or quenched and artificially aged state (T8), which is determined by tactical-technical and cost parameters of the respective welded structures and their operation conditions.

At the same time, under the conditions of technological heating, including the welding processes, 2219 alloy (similar to its Russian analog 1201), demonstrates sensitivity to the temperature level, which is due to the mechanism of solid solution decomposition and morphology of phase precipitation location, and ratio of their volume fraction in the structure [2–4]. Segregation of alloying elements and admixtures along the boundaries of weld crystallites and base metal grains results in formation of a heterogeneous structure, lowering the joint strength by 30–40 %. Welding speed affects the morphology of weld microstructure, as the temperature gradient on the interface of solid solution of liquid metal and phases, as well as the nature of distribution of alloying elements through the weld volume depend on it [3]. At metal overheating formations of brittle interlayers from oversaturat-

Table 1. Mechanical properties of 5 mm sheets of 2219-T31 aluminium alloy

Orientation	$\sigma_t^{b.m.}$ , MPa	$\sigma_{0.2}^{b.m.}$ , MPa	$\delta$ , %	$\alpha$ , deg	$a_n$ , J/cm <sup>2</sup>
Along the rolling direction	368	259.4	24.4	180	30.0
Across the rolling direction	369.6	270.4	22.0	177	23.1

ed phases develop between the grains, particularly on the fusion boundary with the base metal, where they sometimes form a dense frame around the grains. To reduce the heat input, it is recommended to apply concentrated heat sources and, as far as possible, increased welding speeds that ensures minimal level of heat input into the metal, its accelerated cooling, and less strength loss [6–8].

The objective of this work is determination of optimal conditions of welding the rocket load-carrying element set from aluminium alloy of 2219-T31 grade by TIG and MIG methods.

## EXPERIMENTAL PROCEDURE

Before welding, the sheet blanks from 2219-T31 alloy were degreased with further chemical etching in a sodium hydroxide solution with multiple rinsing in hot and cold water. Blank lightening was performed in a nitric acid solution with further washing in running water. The blanks were dried naturally, which was followed by scraping the end faces and surfaces of the edges to be welded (approximately 15 mm wide) to

the depth of 0.1 mm with the purpose of prevention of oxide film inclusions and gas pores in the welds.

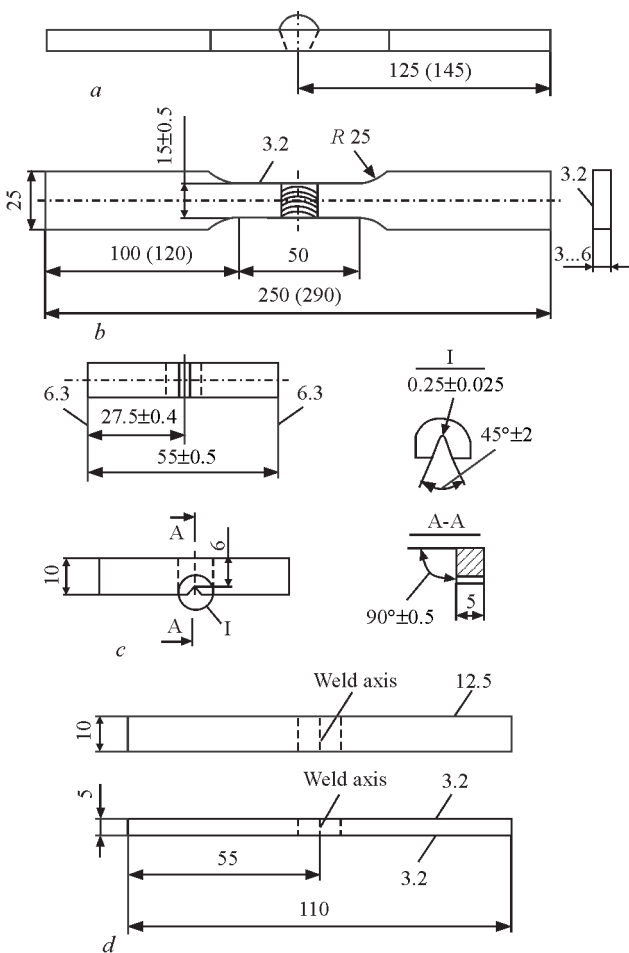
The quality of weld formation was controlled by their appearance. Internal quality of the welds was assessed by the results of detection of defects of the type of cracks, lacks-of-penetration, and pores by roentgenography (GOST 7512–89). X-ray unit RAP-150/300 was used for this purpose, and the density of weld metal was assessed in Densitometr instrument. Control results allowed selection of optimal modes of the welding process, when no coarse defects form.

After welding 2219-T31 alloy the produced butt joints were examined, and measurement of the main geometrical parameters of the welds was conducted. Geometrical parameters of the welds ( $B$  is the weld width from the joint face surface,  $H$  is the weld width from the joint reverse surface (weld root),  $\delta$  is the base metal penetration depth (in this case it is equal to its thickness),  $b$  is the height of technological reinforcement convexities,  $h$  is the weld root height) was determined using electronic caliper ART-34460-150, which had the division price of 0.01 mm, and measurement accuracy of 0.03 mm.

Qualitative assessment of the change in the values of strength, ductility and toughness of welded joints of 2219-T31 alloy, depending on the studied arc welding processes, was performed by the results of mechanical testing of standard samples (GOST 1497–84) using all-purpose TsD-4 machine with 2T scale. Testing was conducted on samples of XIII type to GOST 6996–66. Sample drawings with dimensions are given in Figure 3. Tensile testing and determination of strength values of the joints ( $\sigma_t^{wj}$ ) were conducted using flat samples with technological reinforcements on the face side with removed weld root. Evaluation of weld metal strength ( $\sigma_t^{w.m}$ ) was performed on samples without reinforcement or weld root, which were mechanically removed from the test sample surface. Mechanical tests of the above-mentioned samples were conducted under stationary conditions and their ultimate strength values were calculated ( $\sigma_t^{wj}$  and  $\sigma_t^w$ ). Sample load was here uniformly distributed over the entire working part, in keeping with the requirements of GOST 1497–73.

Strength value determined experimentally allowed calculation of strength coefficients of the joints and establishing the level of their sensitivity to the thermal cycle of welding under TIG and MIG conditions. The degree of their influence on the condition of metal in the welds with technological reinforcement and without it is characterized by the joint strength coefficient, calculated as  $K_w = \sigma_t^{wj} / \sigma_t^{b.m}$  or  $K_w = \sigma_t^{w.m} / \sigma_t^{b.m}$ .

General state of the metal and its deformability after the thermal cycle of welding was assessed us-



**Figure 3.** Drawings of samples which were used to determine the mechanical properties of welded joints: *a* — ultimate strength of welded joint ( $\sigma_t^{wj}$ ); *b* — ultimate strength of weld metal ( $\sigma_t^{w.m}$ ); *c* — impact toughness of weld metal; *d* — welded joint bend angle



ing the technological testing method — bend angle ( $\alpha$ ). This ductility value was determined on samples of base metal and welded joints under the conditions of three-point bending with load application from the weld root side. Technological reinforcement and weld root were here removed by machining to the required dimensions (Figure 3).

Impact toughness value ( $\alpha_n$ ) allowed determination of brittle fracture susceptibility of the joint metal. Its experimental determination was performed using the respective scheme of loading samples with a sharp notch of radius  $R = 0.25$  mm (Charpy) along the weld axis, in keeping with the requirements of GOST 9454–76. Average value of this characteristic was determined by the results of testing three samples.

Modern analysis procedures were used to substantiate the produced experimental results of comprehensive investigation of the mechanical properties of welded joints of 2219-T31 alloy. Their systematization and plotting of graphical dependencies were performed using modern computer technologies, including Smage Pro and Statistica 5.0 programs.

INVESTIGATION RESULTS  
AND THEIR DISCUSSION

In order to form an appropriate technological reinforcement of the welds, using 1.6 mm welding filler wire of 2319 grade it was found that higher quality joints can be produced by TIG method at 12 m/h speed of welding 2219-T31 alloy. The value of welding current here was equal to 290 A. Considering the risks of defect development in the welds (tungsten inclusions), especially when making extended welds, 6 mm tungsten electrode (GOST 23949) with lanthanum oxide or yttrium oxide was used for welding. The distance from the edge of the nonconsumable electrode to the surface of the edges being welded was equal to 4 mm.

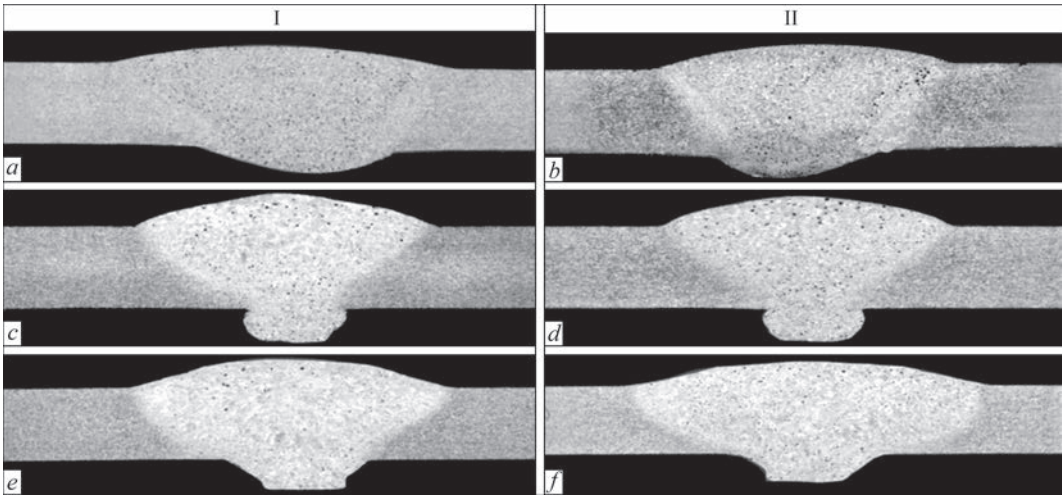
**Table 2.** Tentative modes of automatic nonconsumable electrode welding of 2219-T31 aluminium alloy 5 mm thick

Tungsten electrode diameter, mm	Filler wire diameter, mm	Welding current value, A	Welding speed, m/h	Argon flow rate, l/min
6.0	1.6	290	12.0	15–17

Butt welds were made on blanks of 300×150×5 mm size, which were cut out of sheet semi-finished products along and across the rolling direction, without scraping the edges on the backing. Filler wire feed rate was equal to 128–130 m/h. Welding of the metal from one side was performed without edge preparation. The angle of the torch inclination relative to weld axis was equal to 10–15°, the distance between the torch nozzle and metal being welded was equal to 8–12 mm. Arc length (distance between the metal and wire tip) was equal to 3–5 mm.

Automatic argon-arc welding (TIG) was performed from MW-450 power source of Fronius Company, Austria, which ensures maximal value of welding current of 450 A and allows making extended welds at the required current level. Used for this purpose was symmetrical square wave alternating current of 200 Hz frequency, which will ensure a high degree of cathode cleaning of the edges being welded and stability of performance of 2219-T31 alloy joining process [3]. Tentative modes of welding 2219-T31 alloy 5 mm thick are given in Table 2.

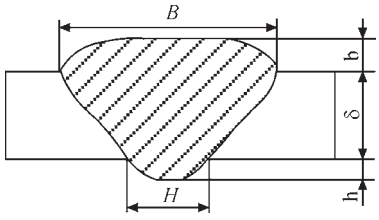
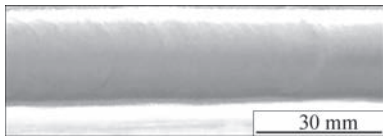



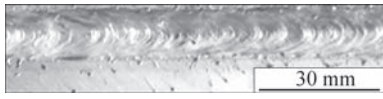
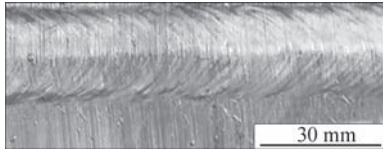
Complete penetration of the edges being welded without their scraping was achieved in one pass. Formation of the back bead, i.e. weld root, occurred at application of a replaceable stainless steel backing with an elliptical shape of the groove of 1 mm depth and 6 mm width. Reliable shielding of the welding zone was ensured by high purity argon (GOST 10157), the flow rate of which was equal to 15–17 l/min. TIG

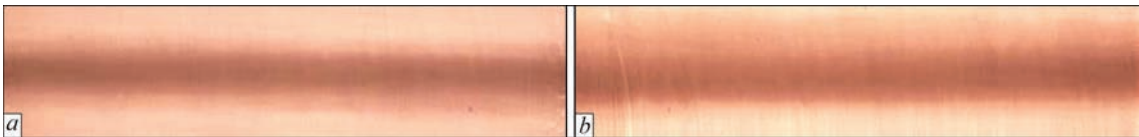


**Figure 4.** Microstructure ( $b$ ) of welded joints of 2219-T31 alloy 5 mm thick produced by TIG ( $a, b$ ) and MIG welding ( $c, d$ ) in argon ( $c, d$ ) and helium ( $e, f$ ) along (I) and across (II) the rolling direction

welding technology was realized in the horizontal position by complete melting of base material and filler wire edges at heating by tungsten electrode arc. All the welding parameters were thoroughly controlled and measured to determine the optimal welding mode of 2219-T31 alloy 5 mm thick. The established mode allowed producing a smooth weld surface with gradual transition to the base metal (Figure 4).

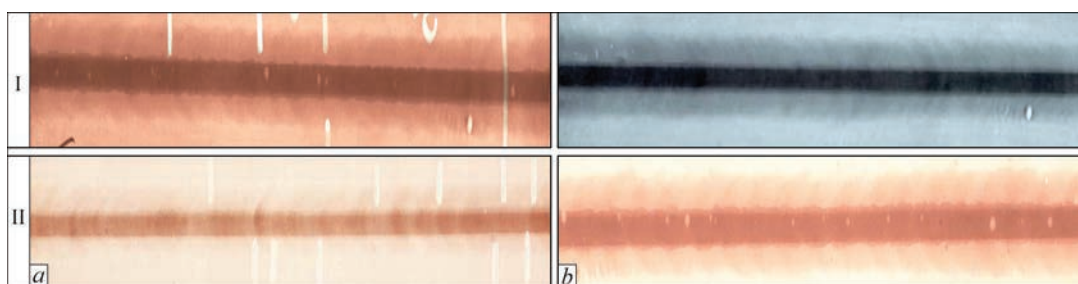
Analysis of the appearance of butt joints and assessment of weld quality by X-ray method did not reveal any coarse defects of the type of cracks, lacks-of-penetration or porosity in the welds, produced by TIG (Figure 5, *a*). This is indicative of realization of appropriate thermal-physical conditions in welding, namely liquid metal solidification and sound weld formation. Application of different polarity

Shielding atmosphere	Rolling orientation					Weld form factor $K = \frac{B}{b + \delta}$	Sample appearance
		$B$	$b$	$H$	$h$		
TIG welding							
Argon	Along	16.04–16.55	0.91–0.95	8.56–9.03	1.27–1.32	2.75	
	Across	15.35–16.43	0.96–1.3	8.22–8.9	1.38–1.56	2.19	
MIG welding							
Argon	Along	13.3–14.15	1.61–1.70	5.45–5.72	1.85–1.92	2.09	
	Across	14.5–16.41	1.51–1.60	5.49–5.75	1.86–2.06	2.22	
Helium	Along	13.9–15.10	1.44–1.67	6.38–7.21	1.84–1.95	2.21	
	Across	16.6–17.18	0.67–0.73	6.08–6.28	1.75–1.89	2.90	
<p>Notes. 1. Weld form factor (<math>K</math>) — ratio of weld width (<math>B</math>, mm) to its thickness (<math>b + \delta</math>), where <math>B</math> is the weld width, <math>b</math> is the reinforcement height, <math>\delta</math> is the molten base metal depth; <math>H</math> is the weld root width, <math>h</math> is the reinforcement height from the weld root side, 2. <math>K</math> value is allowed in the range from 0.5 to 4. Values from 1.2 to 2 are regarded as optimal.</p>							



**Figure 5.** X-ray diffraction patterns of 2219-T31 alloy welds produced by TIG welding in argon along (*a*) and across the rolling direction (*b*)





**Figure 6.** X-ray diffraction patterns of 2219-T31 alloy produced by MIG welding in argon (I) and helium (II) along (a) and across (b) the rolling direction

square wave current in modes, when reverse polarity prevails, ensures efficient degassing of the welds with such a welding process.

Modes of test alloy welding by MIG technology (Figure 3) were also optimized. Their essence is heating of 1.6 mm electrode (filler) wire of 2319 grade by the arc up to melting of its tip and filling of the gap between the edges of blanks being welded by liquid metal. Presence of a replaceable backing from stainless steel with a groove of elliptical shape of 1 mm depth and 6 mm width allowed achieving complete penetration of the edges being welded and forming the weld root in one pass (Figure 4), depending on shielding gas grade — argon (GOST 10157) or helium (GOST 20461, DSTU 141175:2004). Argon flow rate here was equal to 25 l/min, and of helium — 30 l/min.

Butt welds were produced in an argon or helium atmosphere by an arc from IUP-1 power source on blanks of 300×150×5 mm size, which were cut out of sheet semi-finished products along and across relative to the direction of rolling. Visual control of the quality of weld formation showed absence of coarse defects of the type of cracks and lacks-of-penetration in the test alloy butt joints produced by a consumable electrode, but defects in the form of pores were recorded after X-ray inspection. As evidenced by X-ray diffraction patterns of butt joints (Figure 6) produced by MIG in argon, pores of 1 to 2 mm diameter form in the zone of technological reinforcement at liquid metal crystallization, i.e. the welding conditions did not provide its proper degassing. Different factors can be the source of their formation, including temperature conditions of the environment, higher humidity of shielding gas, etc. Porosity can also be caused by segregation of elements present in the composition of 2219-T31 alloy, as a result of structural transformations of the liquid weld metal. In order to prevent

porosity, it is necessary to thoroughly clean the base metal and filler wire from oxides or contamination.

Complete penetration of joints welded by MIG technology in argon, was produced in the mode, when the welding current value was 165–170 A, and arc voltage was 24–25 V. Welding speed was equal to 28–29 m/h. Higher density of welding current enhanced the metal penetrability by the arc. The extent of the arc immersion into the liquid metal of the weld pool is increased, and it has a positive impact on formation of welds of smaller dimensions. It occurred due to high specific arc power and temperature level in the metal region of the impact of an active heating spot, which allowed increasing the process speed, compared to TIG welding [1, 2].

At helium application as shielding atmosphere in MIG welding of 2219-T31 alloy formation of higher quality welds is observed. This is related to the fact that compared to argon, helium provides the thermal-physical conditions of stable realization of the arc process: it promotes increase of metal penetration depth. High concentration of thermal energy at helium-arc welding is ensured by reliable arc excitation and its stable burning, which determines the quality of “cathode” cleaning of the surfaces of the weld and of the zone near it. Owing to a high ionization potential and heat conductivity, the volumes of electrode metal sputtering are reduced. At helium application the electric current was 120–135 A, and voltage was 34–36 V. Welding speed here was 25–27 m/h (Table 3).

Measurement of the geometrical parameters of welds in joints produced by MIG welding in argon, showed that their width varies in the ranges of 13.3–14.15 mm and 14.45–16.11 mm, and in helium it changes in the range of 13.90–15.10 mm, respectively. The dimensions of the weld root (penetration) are 10–15 % larger than in TIG welded joints. In samples

**Table 3.** Tentative modes of automatic consumable electrode arc welding of 2219-T31 aluminium alloy 5 mm thick in shielding gas atmosphere

Shielding atmosphere	Electrode wire diameter, mm	Welding current, A	Welding speed, m/h	Arc voltage, V	Gas flow rate, l/min
Argon	1.6	165–170	28–29	24–25	25
Helium	1.6	120–135	25–27	34–36	20

**Table 4.** Mechanical properties of welded joints of 2219-T31 aluminium alloy 5 mm thick made by argon-arc welding by TIG and MIG methods

Welding process	Shielding atmosphere	Weld orientation relative to rolling direction	$\sigma_t^{wj*}$ , MPa	$\sigma_t^{wm**}$ , MPa	$\alpha$ , deg	$a_n$ , J/cm <sup>2</sup>	Strength factor $K$	
							$\frac{\sigma_t^{w,j}}{\sigma_t^{b,m}}$	$\frac{\sigma_t^{w,m}}{\sigma_t^{b,m}}$
Nonconsumable electrode	Argon	Along	255.2	241.9	60	16.3	0.69	0.66
		Across	258.0	240.9	58	19.4	0.70	0.65
Consumable electrode	Argon	Along	258.6	231.7	45	16.2	0.70	0.63
		Across	261.5	234.8	45	17.0	0.71	0.64
	Helium	Along	238.2	252.0	52	18.5	0.64	0.68
		Across	243.0	239.1	54	18.0	0.66	0.65

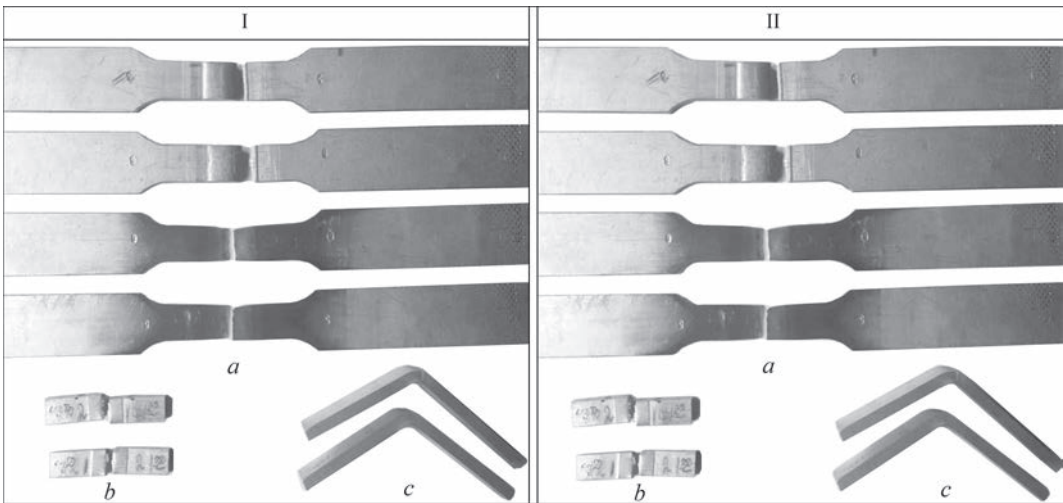
Notes. 1. Samples failed in the zone of weld fusion with base metal: 2. Sample fracture occurred in the weld metal. 3. Strength coefficient is given relative to base metal strength in the initial condition (2219-T31).  $K = \frac{\sigma_t^{w,j}}{\sigma_t^{b,m}}$  — welded joint;  $K = \frac{\sigma_t^{w,m}}{\sigma_t^{b,m}}$  — weld metal.

with technological reinforcement, a reverse dependence of its height on the shielding gas is observed. These values are 30–45 % higher in joints produced by MIG welding in argon. Weld root height, both in the first and second variants of shielding atmosphere differs 1.5 times. Weld form factor, in keeping with formula  $K = B(b + \delta)$  for joints TIG welded along and across the rolling direction, is equal to 2.75 and 2.19, respectively, and for MIG welded joints it is 2.1 and 2.2 in argon, and 2.2 and 2.9 in helium. Comparing the results of measurement of geometrical dimensions of welds in TIG joints, cut out along and across the rolling direction, and in MIG joints made in argon or helium one can see that their values differ by 2–3 mm, respectively. Weld root dimensions are 10–15 % larger in TIG welded joints than in the joints produced under MIG conditions.

To assess the mechanical properties of the joints, produced by TIG using 1.6 mm 2319 welding wire, standard samples from defect-free weld regions were prepared, based on X-ray inspection results. Analy-

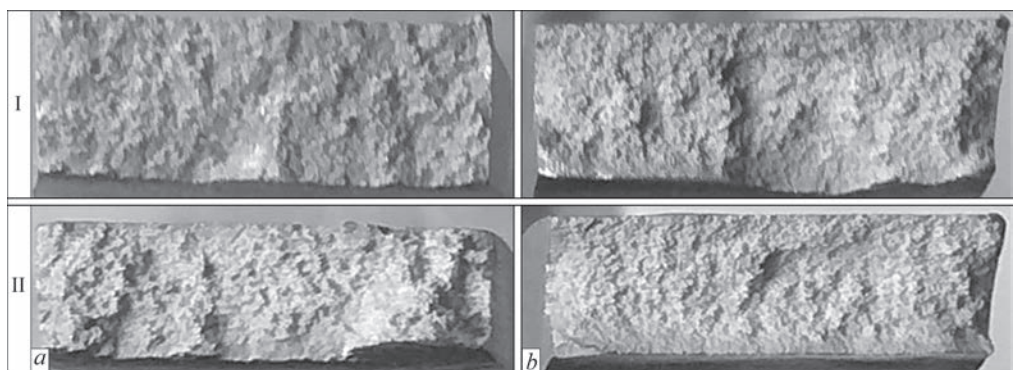
sis of the results of their experimental testing showed (Table 4) that irrespective of the rolling direction, TIG joints with weld reinforcement fail along the zone of weld fusion with the base metal at static tension ( $\sigma_t^{w,j}$ ) (Figure 7). Samples without technological reinforcement fail along the weld metal. Figure 8 shows fractures of samples of 2219-T31 welded joints produced by TIG in both the directions relative to rolling orientation. All the fractures demonstrate a ductile nature of the relief. Pitted structure of the fracture surface is indicative of the mechanism of nucleation, growth and coalescence of microvoids as a result of breaking up of the bridges between the crystallites.

Figures 9 and 10 show the characteristic fractures and special features of fracture surface of 2219-T31 alloy welded joints produced in argon and helium by MIG technology. The pattern of the sample surface depends on its type and loading mode at testing. In samples without technological reinforcement, fracture runs along the weld axis. Their relief is more ductile compared to relief of samples with technological re-



**Figure 7.** Fracture mode of samples of welded joints of 5 mm 2219-T31 alloy produced by nonconsumable electrode in argon along (I) and across (II) the rolling direction under the conditions of mechanical testing: *a* — uniaxial tension; *b* — impact toughness, *c* — three-point bending





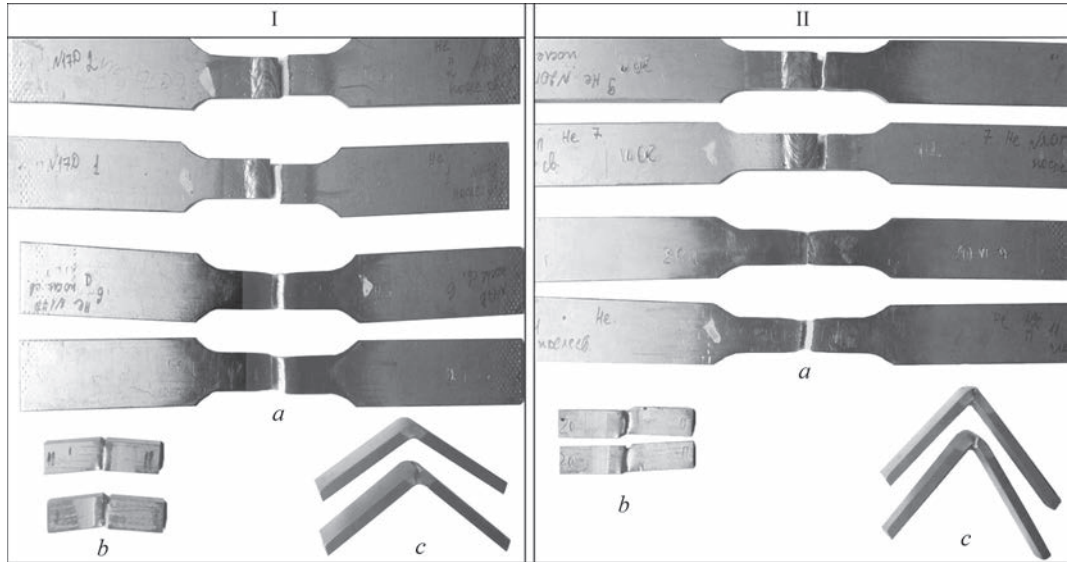
**Figure 8.** Fractures of samples of welded joints of 5 mm 2219-T31 alloy produced by nonconsumable electrode in argon along (I) and across (II) the rolling direction, after mechanical tensile testing: *a* — samples without reinforcement; *b* — samples with reinforcement

inforcement. They fail along the zone of weld fusion with base metal. Here, after TIG welding the ultimate strength of welded joints, where the weld was located along the rolling direction of the welded sheets, is on the level of 247–262 MPa, and in the weld located across the rolling direction it is in the range of 253–261 MPa, i.e. it decreased by almost 30 %, compared to the level of base metal strength.

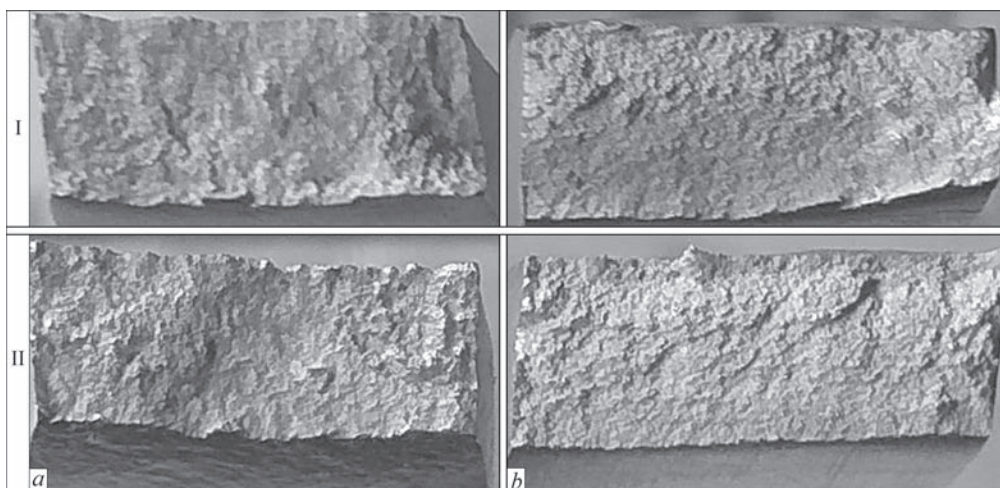
Samples without technological reinforcement fail in the weld metal, where the ultimate strength ( $\sigma_t^{w.m}$ ) at static tensile testing after welding is equal to 237–245 MPa under the conditions of the weld orientation along the rolling direction and 234–247 MPa at its location across the rolling direction. Impact toughness of the metal of welds produced in TIG welding along the rolling direction, varies from 15.9 to 16.9 J/cm<sup>2</sup>, and across the rolling direction it changes from 17.5 to 22.4 J/cm<sup>2</sup>, respectively. Bend angle of the mentioned welded joints is equal to approximately 60° (Table 4). In the case, when the samples have technological reinforcement, the ultimate strength of welded joints, produced by consumable electrode in helium at

weld orientation along the rolling direction, is equal to 231–252 MPa, and at weld orientation across the rolling direction, it is at the level of 227–265 MPa. In welding in argon, the ultimate strength of welded joints is equal to 255–260 and 256–266 MPa at weld orientation along and across the rolling direction, respectively.

When helium is used in MIG welding, a similar dependence of the mode of fracture of test samples of welded joints is observed (Figure 10). The fracture surface has a predominantly ductile relief, which reflects the fine-dendritic structure of the welds. In samples with technological reinforcement, the relief on the fracture surface is more brittle, which is indicative of a higher degree of local deformation of the metal in the zone of weld fusion with the base metal. Welds made along the rolling direction, have the ultimate metal strength on the level of 254–259 MPa, and those welded across the rolling direction – on the level of 257–261 MPa. Bend angle values of joints welded in helium with weld location along the rolling direction decreased to 27–31°, and those across the



**Figure 9.** Fracture mode of samples of welded joints of 5 mm 2219-T31 alloy produced by consumable electrode in helium along (I) and across (II) the rolling direction, under the conditions of mechanical testing: *a* — uniaxial tension; *b* — impact toughness; *c* — three-point bending



**Figure 10.** Fractures of samples of welded joints of 5 mm 2219-T31 alloy produced by consumable electrode in helium along (I) and across (II) the rolling direction, after mechanical tensile testing: *a* — samples without reinforcement; *b* — samples with reinforcement

rolling direction are 1.5 times higher (39–45°). The impact toughness value of the weld metal dropped to 12.9–13.5 and 12.3–12.9 J/cm<sup>2</sup>, respectively.

Analysis of fracture surface morphology in welded joints produced both along and across the rolling direction, showed that their relief has a predominantly cellular structure. It forms as a result of microcrack initiation on coarse phase particles or intermetallic inclusions. The crack length is determined by the size of volume fraction in the base metal and depends on the TIG or MIG welding cycle. Optimal modes of welding 2219-T31 alloy promote formation of a homogeneous structure, which ensures the ductile mode of joint fracture under the test conditions.

## CONCLUSIONS

1. Technological conditions of producing sound welds when joining 5 mm high-strength aluminium alloy of 2219-T31 grade at arc technologies of TIG and MIG welding were studied. It was found that optimal formation of sound welds without coarse defects is achieved under TIG conditions at electric current of 290 A and welding speed of 12 m/h. At MIG in argon atmosphere such welds can be produced using current  $I_w = 165\text{--}170$  A and welding speed of 28 m/h, and in case of helium application — 120–135 A with the speed of 25–27 m/h, i.e. under the conditions, when power losses are 20–30 % lower. Weld form factor *b* in the joints, TIG welded along and across the rolling direction, is equal to 2.75 and 2.19, and in joints MIG welded in argon it is 2.1 and 2.2, and in helium — 2.2 and 2.9, respectively.

2. Level of alloy welded joint strength after TIG is equal to 255–258 MPa, that is 30 % lower compared to base metal ( $\sigma_t = 366\text{--}370$  MPa). Under the conditions of MIG welding in argon joint strength value is equal to 258–261 MPa, and in helium it decreases (238–243 MPa). The above-mentioned occurs as

a result of structural transformations of metal under the thermal-physical welding conditions, and it is also associated with appearance of eutectic interlayers and excess phases near the weld crystallite boundaries. The high probability of defect formation at argon application under MIG conditions, limits its application for critical parts and components.

3. Impact toughness value of TIG welds made along the rolling direction is equal to 15.9–16.9 and across the rolling direction it is 17.5–22.4 J/cm<sup>2</sup>. Technological ductility (bend angle) of the joints is equal to 50 and 60°, respectively. After MIG welding in argon this value is almost the same, irrespective of the rolling direction (43–46 and 44–47°), in helium it is 50–55 and 53–57°, respectively, which is almost 3–4 times lower than the base metal value (180 and 177°). Impact toughness of welds after MIG welding in helium is 18.3–18.6 J/cm<sup>2</sup> along the rolling direction, and 17.5–18.4 across the rolling direction. In case of argon application a lowering of the value depending on the rolling direction is observed in the welds, 16.0–16.5 and 16.9–17.1 J/cm<sup>2</sup>, respectively.

4. Fracture of joints of 2219-T31 alloy with technological reinforcement and weld root occurs along the boundary of the weld fusion with the base metal, and at a distance from the surface it runs along the weld axis. The relief retains a predominantly cellular structure, microcrack initiation, probably, occurs on the coarse phase particles or intermetallic inclusions, located along the boundaries of crystallites and metal grains, much more brittle than the aluminium matrix. The length of the primary crack depends on the volume fraction of the above-mentioned particles in the alloy and thermal-physical conditions of welding (TIG or MIG). It is found that formation of a more uniform structure of weld relief, when the proper joint strength and ductile mode of their fracture are pro-



duced, can be achieved with optimum modes for both the technologies.

## REFERENCES

1. Beletsky, V.M., Krivov, G.A. (2005) *Aluminium alloys (Composition, properties, technology, application)*: Refer. Book. Ed. by I.N. Fridlyander. Kyiv, Komintekh [in Russian].
2. Albert, D. (1993) Aluminium alloys in arc welded constructions. *Welding World*, 32(3), 97–114.
3. Ishchenko, A. Ya., Labur, T.M. (2013) *Welding of modern aluminium alloy structures*. Kyiv, Naukova Dumka [in Russian].
4. Labur, T.M. (2022) Tendencies of technological development of arc welding processes for joining modern aluminium alloys. *Svarshchik*, 1, 6–17 [in Russian].
5. Lobanov, L.M., Labur, T.M., Mazur, O.A. et al. (2022) Cost optimization of the methods of welding structures of fuel tanks for aerospace vehicles. *Avtomatych. Zvar.*, 3, 42–52 [in Ukrainian].
6. Nyrkova, L.I., Labur, T.M., Shevtsov, E.I. et al. (2022) Complex of properties of 2219 alloy weld joint in T62 state under modeling operating conditions. *Space Sci. & Technol.*, 28(2), 14–29.
7. Mashin, V.S., Poklyatsky, A.G., Fedorchuk, V.E. (2005) Mechanical properties of aluminium alloys in consumable and nonconsumable electrode arc welding. *The Paton Welding J.*, 9, 39–45.
8. Kiyoto, S. (1993) Materials and joining technologies for rocket structures. *J. of the JWS*, 62(8), 46–52.

## ORCID

T.M. Labur: 0000-0002-4064-2644,  
A.G. Pokliatskyi: 0000-0002-4101-2206,  
V.A. Koval: 0000-0001-5154-1446

## CONFLICT OF INTEREST

The Authors declare no conflict of interest

## CORRESPONDING AUTHOR

A.G. Pokliatskyi  
E.O. Paton Electric Welding Institute of the NASU  
11 Kazymyr Malevych Str., 03150, Kyiv, Ukraine.  
E-mail: pag556a@gmail.com

## SUGGESTED CITATION

T.M. Labur, A.G. Pokliatskyi, V.A. Koval (2024) Consumable and nonconsumable electrode welding of high-strength 2219-T31 aluminium alloy. *The Paton Welding J.*, 5, 18–27.

## JOURNAL HOME PAGE

<https://patonpublishinghouse.com/eng/journals/tpwj>

Received: 08.02.2024

Received in revised form: 11.03.2024

Accepted: 23.05.2024



Developed in PWI

## ELECTRON BEAM SMELTING OF INGOTS OF HIGH-STRENGTH TITANIUM ALLOYS

Products using high-strength titanium alloys





Semi-finished products from high-strength titanium alloys for industry








# OPTIMIZATION OF THE METAL POOL SHAPE DURING ELECTROSLAG SURFACING IN A STATIONARY CURRENT-SUPPLYING MOULD FOR MANUFACTURE OF BIMETALLIC PRODUCTS

V.G. Solovyov, Yu.M. Kuskov, I.Yu. Romanova

E.O. Paton Electric Welding Institute of the NASU  
11 Kazymyr Malevych Str., 03150, Kyiv, Ukraine

## ABSTRACT

Mathematical modeling of multiphysics processes of Joule heating has been conducted using a finite element model of a stationary current-supplying mould (CSM). To manufacture bimetallic products using a stationary current-supplying mould with a circular cross-section during melting of a discrete additive at its batch feeding, the study presents the results of calculated assessment of the dependence of such metal pool shape parameters as the mirror diameter and the liquid fraction depth on the slag pool depth and CSM design parameters, namely the mould diameter, the thickness of copper bushings in the mould current-supplying and forming sections, the water-cooled bottom plate thickness, and the variations in the graphite lining height caused by wear. The findings will contribute to improvement of the mould design, optimization of the metal pool shape, and the technology of discrete additive melting at batch feeding in a stationary CSM.

**KEYWORDS:** stationary current-supplying mould, metal pool parameters, shape optimization, multiphysics modeling, electroslag surfacing, bimetallic product

## INTRODUCTION

The method of surfacing and remelting in a current-supplying mould (CSM) [1] has specific features determined by the design of this device. First of all, it represents a section nonconsumable electrode of a circular type. In CSM, the lower section, electrically isolated from the upper one, is the forming one (FMS), in which the metal pool (MP) is formed. The second nonconsumable electrode represents a bottom plate or a product being formed. In addition, due to a vertical cut in a current-supplying section, a magnetic field is generated in the melt, due to which, the rotation of slag (SP) and metal pools in the horizontal plane is provided. Stationary CSM has one more important feature – comparatively small ingots (not more than 60 mm) are deposited in it.

Ksendzyk G.V., the author of the idea and the base model of a current-supplying mould, suggested to use a “clamping device for current supply connected to the device for additive feeding to the slag pool” as a means to influence the crystallization front shape of the molten metal in the FMS. This enabled an adjustment of the MP shape by means of varying the current direction and value in the clamping device. This allows making it more flat and thus reducing the risk of defects in crystals [2, 3].

This is especially important for fusion of bimetallic parts. Flat MP is achieved by selecting the optimal ratio of currents, voltages and feed rate of a consumable electrode or a consumable discrete additive, as well as the thermal level of the SP and the intensity of heat sink

through the mould walls [4]. The geometric CSM parameters, such as the diameters of the mould and electrode (consumable and nonconsumable), the distance between the MP mirror and the lower end of the graphite lining (GL), the thickness of the electric insulating gasket between the both sections of the mould and bottom plate, have a great effect on the MP formation. A series of works has been devoted to the control of the metal pool formation process [5, 6]. In [5], a conclusion is made, that a flat MP shape can be obtained in a double-circuit surfacing at appropriate power ratios on the mould and electrode. In [6], different existing methods and technological techniques of the metal crystallization control in electroslag remelting are characterized, which are based on the use of metallurgical mechanisms and external physical influences. It has been concluded that the control of the process of primary crystallization of ingots, especially complex alloys and ingots of large diameters, remains one of the key tasks in the further development of electroslag technologies. In [7], the method of impact on the metal pool shape by means of the external magnetic field is used. Thus, the traditional Joule heating and stirring of the liquid metal under the influence of a directed magnetic field are combined.

As indices of the MP shape, geometric data of its sizes such as the relative average for the product surface, penetration depth and relative penetration unevenness [8, 9], as well as height of the cylindrical part of MP are used. In the best case, the optimal MP shape should be minimal in height and have a cylindrical shape.

In [10], the authors came to the conclusion that the average mould section, which is conducting, shunts a



part of SP and shifts the area of a predominant heat sink into the near-wall area, leaving the central zone relatively cold. However, directly near the mould wall itself, the MP remains relatively cold due to water cooling of the mould. As a result, the MP bottom can take a specific shape of “sombbrero”. The shape of the MP bottom in the form of “sombbrero” is characterized by a large relative unevenness of the MP, so it requires optimization.

Mathematical modeling of heat exchange, melting and solidification processes in the electroslag technology becomes an effective means of theoretical research [11–14].

## THE AIM

of the work is to analyze the factors affecting the MP shape when manufacturing bimetallic products using a stationary CSM with a circular cross-section in the process of melting a discrete additive at its batch feeding, as well as to optimize the thermal physical processes of surfacing by means of mathematical modeling. Within the frames of a calculation experiment, the possibilities of improving the MP shape by variations in the CSM design were considered.

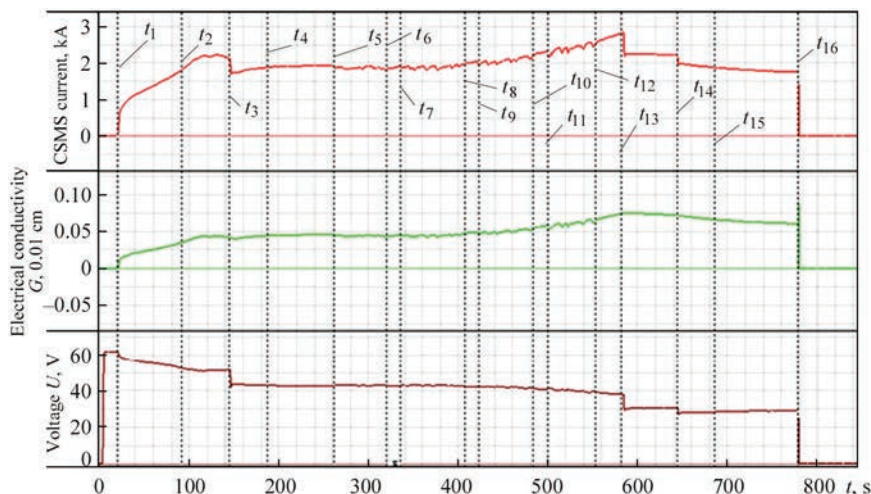
## METHODS OF EXPERIMENTAL RESEARCH

In the work, the results of the experimental electroslag surfacing (ESS) of layers with a different thickness using a stationary current-supplying mould with a vertical cut in a current-supplying section were used [15]. This surfacing was conducted to study the nature of variation in the electrotechnical parameters of the discrete additive melting process at batch feeding. During the experiment, rotation of the SP was observed. AC voltage from the TShP-10 transformer with a sinusoidal voltage having four voltage variation degrees was supplied to the terminals of the current-supplying mould section (CSMS) and the mould bottom plate. The “liquid” start was used. A batch four-time shot feeding by 2 kg was performed. During the experiment, the voltage applied to the terminals of the copper CSMS bushing and the

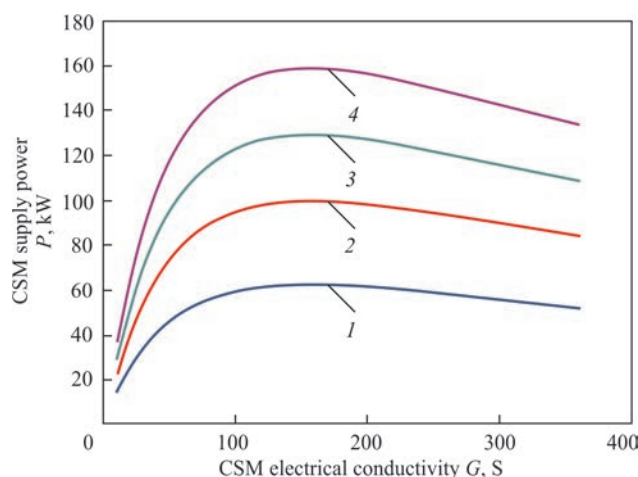
bottom plate, as well as the current in the CSMS-slag pool-metal pool-product-bottom plate circuit were measured in time. The digital conversion of the mentioned parameters and the calculation of the conductivity and consumed power of the measured electrical circuit were performed. In the future, to simplify the presentation, the obtained electrical parameters were attributed to the CSM as a whole. Figure 1 shows the nature of variation in the CSM electrical conductivity in the process of the experiment.

After switching the current source from the 4<sup>th</sup> to the 3<sup>rd</sup> degree, the voltage in the CSM changed from 51 to 43 V. The shot charging was accompanied by a gradual increase in the CSM current and electrical conductivity even after the end of charging. This was partially explained by a decrease in the slag layer level between the molten metal layer on the bottom plate and the graphite lining of the CSMS, as well as an increase in the SP temperature due to a rise in the current (from 1.9 to 2.8 kA). A drop in the current was achieved by switching to the 2<sup>nd</sup> and then to the 1<sup>st</sup> degree of the power source. In the physical experiment, CSM with the following design parameters was used: internal mould diameter  $D_m = 180$  mm; CSMS height  $h_{CSMS} = 90$  mm; FMS height  $h_{FMS} = 73$  mm; GL height  $h_{gl} = 65$  mm; GL thickness  $T_{gl} = 15$  mm; SP depth  $h_{sp} = 70$  mm.

Stages of surfacing (Figure 1):  $t_1$  — liquid slag pouring, switching on the power source to the 4<sup>th</sup> degree;  $t_2$  — increase in the slag rotation;  $t_3$  — 3<sup>rd</sup> degree is switched on;  $t_4$  — the process runs stable;  $t_5$  — beginning of feeding the 1<sup>st</sup> shot batch;  $t_6$  — end of feeding the 1<sup>st</sup> shot batch;  $t_7$  — beginning of feeding the 2<sup>nd</sup> shot batch;  $t_8$  — end of feeding the 2<sup>nd</sup> shot batch;  $t_9$  — beginning of feeding the 3<sup>rd</sup> shot batch;  $t_{10}$  — end of feeding the 3<sup>rd</sup> shot batch;  $t_{11}$  — beginning of feeding the 4<sup>th</sup> shot batch;  $t_{12}$  — end of feeding the 4<sup>th</sup> shot batch;  $t_{13}$  — the 2<sup>nd</sup> degree is switched on;  $t_{14}$  — the 1<sup>st</sup> degree is switched on;  $t_{15}$  — pool rotation is normal;  $t_{16}$  — switching off the power source.



**Figure 1.** Variation in current, electrical conductivity and voltage on CSM over time in the process of surfacing



**Figure 2.** Dependences of power, consumed by the mould, on the CSM electrical conductivity for four degrees of voltage variation of the TShP-10 power source, obtained during surfacing: 1 — first degree; 2 — second degree; 3 — third degree; 4 — fourth degree

In the experiment, ANF-29 flux (melting point is 1230–1250 °C); the shot being deposited from chromium cast iron, batch by 2 kg were used. During melting, a shot batch turned into a liquid metal, which was subsequently solidified in the form of a deposited layer of ~12 mm thick.

Based on the results of the experiment data analysis, the dependence of the specific electrical conductivity of ANF-29 flux  $\sigma_{sp}$  on the SP temperature at a hypothetical point of its maximum value  $\sigma_{sp}[T_{\max}] = 1.349 \cdot 10^{-3} T_{\max}^{1.638} + 138.2$  was obtained for the temperature range of 1000–2000 °C. A hypothetical point of the maximum value of the SP temperature is a point, at which the SP temperature reaches the highest value at set electroslag process parameters. The maximum value of the SP temperature at a hypothetical point was determined as a result of calculating the thermal SP field using an additional CSM substitution design model, similar to that described in [15].

Based on the results of the analysis, the dependencies of power consumed by the CSM on the CSM

electrical conductivity for four degrees of the power source were obtained (Figure 2).

The data of these dependencies were used to predict surfacing parameters that were not obtained during a physical experiment. Analytical appearance of the obtained dependences is the following:

$$P(G) = a \exp(bG) + c \exp(dG)$$

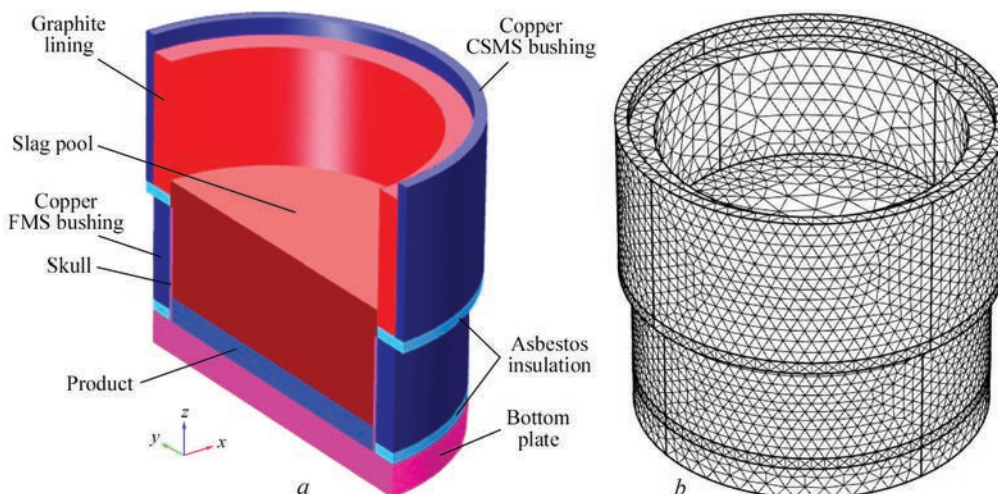
where for the 1<sup>st</sup> degree:  $a = 77.16$ ;  $b = -0.001076$ ;  $c = -75.78$ ;  $d = -0.02025$ ; for the 2<sup>nd</sup> degree:  $a = 124.0$ ;  $b = -0.0011076$ ;  $c = -121.8$ ;  $d = -0.02025$ ; for the 3<sup>rd</sup> degree:  $a = 160.6$ ;  $b = -0.001076$ ;  $c = -157.7$ ;  $d = -0.02025$ ; for the 4<sup>th</sup> degree:  $a = 197.6$ ;  $b = -0.001076$ ;  $c = -194.0$ ;  $d = -0.02025$ . Determination coefficient is  $R = 0.9999$ .

The data obtained as a result of the experiment were used to create and validate the ESS mathematical model of in the CSM.

## MULTIPHYSICS MODELING

Multiphysics modeling was performed on a graphic three-dimensional model (Figure 3, *a*) with modeling of the Joule heating. The model contains the upper current-supplying mould section, consisting of a copper water-cooled bushing without a vertical cut and a graphite lining, as well as the lower forming mould section, which is the second copper bushing. In addition, the model contains a slag pool, a product, a bottom plate, a skull between the forming section and the SP/product, as well as asbestos insulation between the sections of the mould and bottom plate.

By means of the magnetic field generated by the current-supplying mould section, the rotation of slag and metal pools in the horizontal plane is provided. As a result, heating of the external water-cooled SP edges and heat sink from its maximum heating zones is intensified, which in itself leads to the thermal SP field equalization in a horizontal cross-section and an increase in the intensification of the surfacing process and the consumed power. However, in the scien-



**Figure 3.** Examples of model scheme: *a* — CSM design; *b* — finite element model of CSM



**Table 1.** Physical properties of materials for modeling

Parameter	Product	Slag	Graphite	Asbestos	Copper
Heat conductivity $C_p$ , J/(kg·K)	475	1200	710	1000	385
Relative dielectric permeability $\varepsilon$	1	1	1	5	1
Density $\rho$ , kg/m <sup>3</sup>	7850	8960	1950	$\rho[T]$	8940
Thermal conductivity $k$ , W/(m·K)	44.5	60	150	$k[T]$	400
Temperature expansion coefficient $\alpha$ , 1/K	$12.3 \cdot 10^{-6}$	—	—	—	$3.862 \cdot 10^{-3}$
Specific electrical conductivity $\sigma$ , S/m	$4.032 \cdot 10^6$	$\sigma_{sp}[T]$	$2 \cdot 10^5$	$4.032 \cdot 10^{-6}$	$5.998 \cdot 10^7$

tific literature, there are different opinions about the electromagnetic effect on the depth of a metal pool, formed during the electroslag process. As noted by Ksendzyk G.V. in [16], “some of them believe that simple rotation of slag and metal pools leads to an increase in the MP depth and only a reciprocating movement ensures its decrease”. We believe that the solution of a hydrodynamic problem associated with the movement of liquid in the slag pool can adjust certain values of the metal pool depth relative to that calculated using the presented model. We also believe that the trends of the effect of variations in the geometric parameters of the model on the MP shape will not change. In connection with the stated above, when modeling a current-supplying mould, we did not use an split current-supplying section, which provides the rotation of slag and metal pools in the horizontal plane, did not solve the hydrodynamic problem, but limited to electromagnetic and thermal models.

Based on the provisions of the theory of similarity [17], a geometric model was created, that takes into account the similarity of its geometric parameters with the geometric parameters of the physical model. The main condition for modeling was to provide the maximum correspondence of the geometric part of the model with the geometric parameters and the results of the physical experiment. The physical properties of the materials of the slag, welding product and electrodes were used (Table 1).

The model uses the following design parameters: internal mould diameter  $D_m = 180$  mm; CSMS height  $h_{CSMS} = 90$  mm; FMS height  $h_{FMS} = 74$  mm; GL height  $h_{gl} = 80$  mm; GL thickness  $T_{gl} = 15$  mm; SP depth  $h_{sp} = 90$  mm; thickness of copper CSMS bushing, the surface of which is cooled with water  $l_{gl} = 7$  mm; thickness of copper FMS bushing, the surface of which is cooled with water  $h_{cb} = 15$  mm; asbestos insulation gasket height  $h_i = 7$  mm; product height  $h_{ph} = 15$  mm; bottom plate height  $h_{b,p} = 20$  mm.

Parameters  $\rho[T]$ ,  $k[T]$  are set by the appropriate approximation dependencies on the temperature  $T$ , K (not given in the article).

The SP is heated at the expense of the Joule heat released while passing the electric current through it. To study the distribution of electric field, current and

potential in slag and metal pools, as well as to analyze the heat distribution in the volume of the studied zone, a finite element model was used (Figure 3, b).

The model solves the following thermal conductivity equations:

$$\rho(T)C_p \frac{\partial T}{\partial t} + \nabla \cdot q = Q,$$

where  $q = -k(T)\nabla T$ ;  $Q$  is the additional heat source (in capacity of which, a heated metal pool can be used), W/m<sup>3</sup>;  $q$  is the heat flow density, W/m<sup>2</sup>.

In the stationary coordinate system, the point form of the Ohm's law has the following appearance:  $J = \sigma(T)E$ ; where  $J$  is the current density, A/m<sup>2</sup>;  $E$  is the electric field strength, V/m. The static form of the equation of current continuity in the electrically conductive environment requires:  $\nabla J = -\nabla\sigma(T)\nabla U = 0$ , where  $U$  is the voltage on CSM, V.

In the model, a stationary problem is solved and the results of the already established process are derived. The model allows determining the potential, current density and temperature at each point of the studied space in different variations (within the parameters determined by the technology) of the mould diameter, product thickness, distance between the MP and the lower CSMS edge, SP depth, etc.

The following restrictions were accepted for calculating the parameters of multiphysics processes in the model:

- hydrodynamic processes in the slag pool are not considered;
- device for water cooling of copper CSMS and FMS bushings and bottom plate is not considered;
- electrical contacts of the model are free side surfaces of the CSMS electrode and bottom plate;
- supplied voltage on the CSM does not exceed 15–60 V;
- power source current does not exceed 7 kA;
- the maximum value of the temperature  $T_{max}$  of heating SP elements does not exceed the boiling point of the slag. In the model,  $T_{max} = 1800$  °C;
- thermal losses due to radiation are not considered;
- the values of only set parameters after the transition process are considered.

Based on the results of analysing the data obtained from the experiment, the dependence of the specific electrical conductivity of ANF-29 flux on the SP temperature at the point of its maximum value is determined. This dependence was used to control  $T_{\max}$  when calculating modeling results with the aim not to exceed it. If as a result of the mathematical experiment at set input parameters,  $T_{\max}$  exceeds the boiling point of the slag, then the values of input parameters are reviewed.

## MATHEMATICAL EXPERIMENTS ON THE MP FORMATION

### INFLUENCE OF THE SLAG POOL DEPTH ON THE METAL POOL SHAPE

The impact of a growth in the SP depth on its thermal level at a constant interelectrode distance was considered under the following initial conditions: distance between the product and the level of the lower CSMS edge  $H_{pgl} = 73$  mm; SP depth  $h_{sp} = 90$  mm; voltage on the CSM relative to the bottom plate  $U = 42.7$  V. The calculation under these initial conditions showed that the maximum SP temperature at the level of the lower CSMS edge  $T_{CSMS} = 1767$  °C; the maximum MP mirror temperature  $T_{MP} = 1450$  °C; the electrical conductivity of the mould  $G_m = 44.5$  S; the consumption power  $P_m = 81.1$  kW; the maximum depth of the liquid part of MP  $H_{lf} = 6.7$  mm; the depth of the interfacial part of MP  $H_{mp} = 2$  mm.

After an increase in the SP depth by 40 mm (from 90 to 130 mm), the values of other parameters being constant, the calculation showed the following: the maximum SP temperature at the level of the lower CSMS edge  $T_{CSMS} = 1627$  °C; the maximum MP mirror temperature  $T_{MP} = 1525$  °C; the electrical conductivity of the mould  $G_m = 49.9$  S; the consumption power  $P_m = 91$  kW; the maximum depth of the liquid part of MP  $H_{lf} = 9.6$  mm; the depth of the interfacial part of MP  $H_{mp} = 2$  mm.

The relative impact of the SP depth, other geometric parameters being constant, on the power consumed by the process, the CSM electrical conductivity and the MP depth is the following:  $\delta P_m = (91 - 81.1)/40 = 0.25$ ;  $\delta G_m = (49.9 - 44.5)/40 = 0.135$ ;  $\delta h_{mp} = (9.6 - 6.7)/40 = 0.0725$ .

From this it follows that an increase in the SP depth, other geometric parameters being constant,

leads to an increase in the MP depth. For example, an increase in the SP depth by 10 mm leads to an increase in the MP depth by  $\sim 0.7$  mm.

### IMPACT OF THE WEAR VALUE OF THE LOWER EDGE OF THE GRAPHITE LINING ON THE METAL POOL SHAPE

The impact of the wear  $O_{gl}$  of the lower edge of the graphite lining of the CSMS as a result of operation on the power consumed by the mould, electrical conductivity and MP depth is considered. For the calculations, six values of the GL wear height relative to its initial location were accepted, bearing in mind that at the value  $O_{gl} = 0$ , the calculation was carried out in the p. 1. The results are given in Table 2.

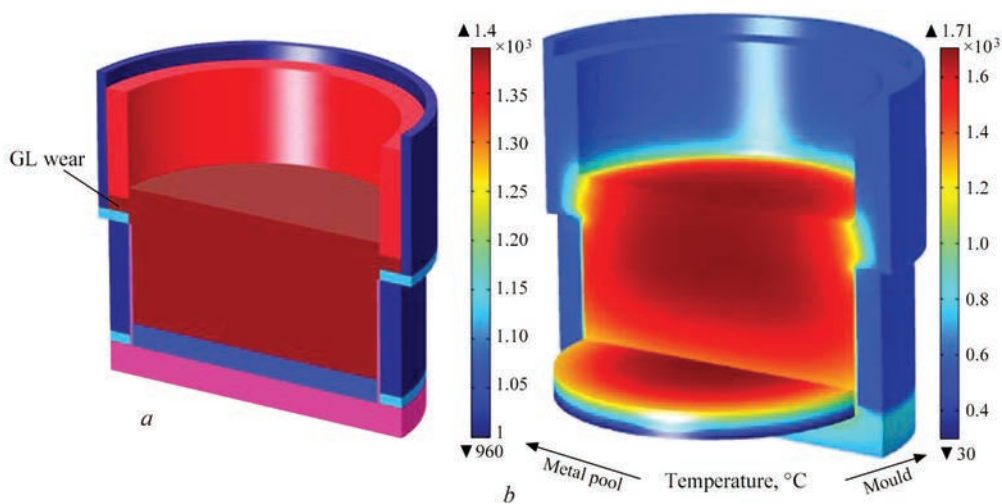
In Nos 5 and 6 of the experiment, the lack of the pool is predetermined by the absence of the required level of power released in the slag pool under these created conditions.

The data (Table 2) indicate a significant impact of the wear of the lower GL edge on the MP formation. This phenomenon is associated with sharp cooling of the SP, caused by a direct contact of the slag with a water-cooled copper bushing. It is important to keep in mind that depletion of the wall in the copper CSMS bushing can lead to its rapid wear due to electric erosion, especially taking into account, that the lower CSMS edge is characterized by the highest current density, flowing in the mould. In addition, an increase in the GL production leads to an increase in the contact area with the slag and, accordingly, to an increase in the temperature of the copper bushing wall that borders it. The larger the area of the current-conducting bushing is protected by graphite, the lower probability of damages to the bushing in this place with erosion and the greater the probability that with some small area of an unprotected bushing and the corresponding low current density passing through this part, the formation of slag crust on this small surface area is probable. Therefore, at some point and within some time, there may be a replacement of graphite protection of some part of the copper surface with the help of a slag crust. But since the current-supplying section is connected to the power source, with the further increase in the area of unprotected graphite of the copper bushing, the copper wall will be heated to the melting point (about 1100 °C) and an emergency situation may occur.

**Table 2.** Impact of wear of the lower GL edge on the metal pool shape

Exp. No.	GL wear $O_{gl}$ , mm	Power $P_m$ , kW	CSM conductivity $G_m$ , S	MP depth $H_{lf}$ , mm	MP mirror diameter $\phi_{mp}$ , mm
1	0.1	80.2	44.0	6.7	176
2	1	79.6	43.6	6.2	176
3	4	77.2	42.3	4.28	146
4	8	73.9	40.6	1	74
5	12	70.7	38.7	—	No pool
6	16	67	36.8	—	





**Figure 4.** Examples of modeling results: *a* — graphite lining wear location; *b* — graphic temperature distribution in CSM at GL deformation

Figure 4 shows fragments of GL wear modeling.

*IMPACT OF VARIATION IN THE THICKNESS OF THE COPPER CSMS BUSHING ON THE METAL POOL SHAPE*

The thickness of the water-cooled upper CSMS and the lower FMS copper bushings, as well as the thickness of the water-cooled bottom plate together with the workpiece determine the consumed component of the CSM thermal balance. As a result of variation in the thicknesses of the mentioned components of the CSM design at a constant voltage, it is possible to change the thermal level of the surfacing process and influence the MP shape.

The created model was used to analyze the level of the impact of the variation in the wall thickness of the copper CSMS bushing  $l_{sw}$  on  $P_m$ ,  $G_m$  and  $H_{if}$ . The initial value  $l_{sw} = 7$  mm. Table 3 shows the results of calculations of the impact of the thickness of the copper CSMS bushing on the MP parameters. The calculations were performed at the voltage on the CSM  $U = 35.7$  V, the distance between the MP mirror and the lower CSMS edge is 58 mm.

The given data indicate that at a voltage being constant, there is almost no impact of the wall thickness of the copper CSMS bushing on the electrical conductivity of the mould, consumed power and the temperature of the bushing side bordering on the GL. The variation in the wall thickness has a relatively small impact on the MP depth. As the wall thickness of the copper CSMS bushing becomes larger, the MP depth increases slightly and the mirror diameter or the

height of the cylindrical part of the MP grows slightly. This is explained by the fact that with an increase in the wall thickness of the copper CSMS bushing, the thermal level of the SP grows due to reduction in losses through the bushing. At a constant value of the power consumption, the MP heating grows. This is accompanied by an increase in the depth and width of the MP. The fact that a slight variation in the wall thickness leads to the variation in the temperature of the bushing side, which borders on the GL, indicates that the wall thickness can still be reduced to a certain value, which depends on the arrangement of the system for cooling the copper bushing. At the same time, the MP depth will decrease.

Due to the fact, that the CSMS bushing is under the thermal and electric protection of the GL, it becomes necessary to check the possibility of replacing the copper bushing with a steel one, which is less expensive.

*REPLACING THE COPPER CSMS BUSHING WITH A STEEL ONE*

Impact on the metal pool shape. The experiment was conducted in the conditions similar to those specified in the p. 3 of the section. For the experiment, St3 steel was selected. The presented data (Table 4) confirm that when replacing the copper CSMS bushing with a steel one and while keeping the same voltage on the CSM, as in the previous experiment, the consumed CSM power and electrical conductivity remained unchanged. However, an increase in the thermal impact on the MP was observed, which led to an increase in its depth and the mirror diameter. Hence, it follows

**Table 3.** Analysis of the impact of the wall thickness of the copper CSMS bushing on the MP parameters

Exp. No.	Thickness of copper wall $l_{gp}$ , mm	Power $P_m$ , kW	CSM conductivity $G_m$ , S	MP depth $H_{if}$ , mm	MP mirror diameter $\varnothing_{mp}$ , mm	Temperature of the copper wall, °C
1	7	71.9	56.5	7.2	162	571
2	11	72.0	56.5	7.4	162	580
3	15	72.0	56.5	7.5	164	590

**Table 4.** Analysis of the impact of replacing the copper CSMS bushing with a steel one on the metal pool shape

Exp. No.	Thickness of steel wall $l_{sw}$ , mm	Power $P_m$ , kW	CSM conductivity $G_m$ , S	MP depth $H_{if}$ , mm	MP mirror diameter $\varnothing_{mp}$ , mm	Temperature of the steel wall, °C
1	7	71.9	56.5	8.8	172	701
2	11	72.0	56.5	9.7	176	761
3	15	72.0	56.5	10.4	176	810

**Table 5.** Analysis of the impact of the wall thickness of the copper FMS bushing on the MP parameters

Exp. No.	Thickness of copper wall $h_{cb}$ , mm	Power $P_m$ , kW	CSM conductivity $G_m$ , S	MP depth $H_{if}$ , mm	MP mirror diameter $\varnothing_{mp}$ , mm	Temperature of the copper wall, °C
1	7	76.1	56.5	7	167	559
2	11	76.2	56.5	7.2	167.8	565
3	15	76.2	56.6	10.2	170.2	588

that by reducing the voltage on the CSM and, accordingly, reducing the consumed power of the CSM, it is possible to return the characteristics of the MP to the values similar to the previous experiment (p. 3).

*IMPACT OF VARIATION IN THE THICKNESS OF THE COPPER FMS BUSHING ON THE METAL POOL SHAPE*

The experiment was carried out in the conditions similar to p. 3. Table 5 shows the calculation data of the impact of the thickness of the water-cooled copper bushing of the forming FMS section  $h_{cb}$  on  $P_m$ ,  $G_m$  and  $H_{if}$ .

The mentioned data indicate that at a constant voltage, the impact of the wall thickness of the copper FMS bushing on the electrical conductivity of the mould and its consumed power is almost absent. The variation in the wall thickness has a significant effect on the MP depth than the variation in the thickness of the copper CSMS wall due to the presence of a thermal insulating GL in the CSMS. As the wall thickness of the copper FMS bushing becomes larger, the MP depth grows, and the diameter of the MP mirror increases. This is explained by the fact that with an increase in the wall thickness of the copper FMS bushing, the thermal level of the SP grows due to reduction in the heat losses through the bushing. At a constant value of the consumed power, the MP heating grows, which is accompanied by an increase in the depth and

width of the MP. This is important when it is necessary to increase the diameter of the MP mirror to the maximum value at a set voltage.

*IMPACT OF VARIATION IN THE THICKNESS OF THE WATER-COOLED BOTTOM PLATE ON THE METAL POOL SHAPE*

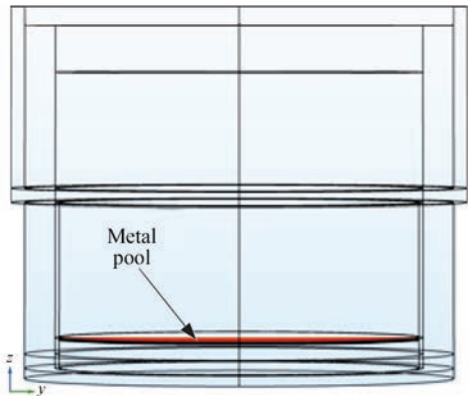
The experiment was carried out in the conditions similar to those described in p. 3. Table 6 shows the calculation data on the impact of the variation in the thickness of the water-cooled bottom plate  $h_{b,p}$  on  $P_m$ ,  $G_m$  and  $H_{if}$ . The product height in the experiment remains constant  $h_{ph} = 30$  mm. The given data indicate that at a constant voltage of the power source, the impact of the variation in the bottom plate thickness on the electrical conductivity of the mould and its consumed power is almost absent.

The variation in the bottom plate thickness leads to an increase in the depth and diameter of the MP mirror. When reducing the bottom plate thickness and increasing the voltage on the CSM, the MP shape can be significantly improved. Figure 5 shows an example of the MP with a depth  $H_{if} = 2.6$  mm and the mirror diameter of 176 mm at  $U = 51$  V, bottom plate thickness of  $h_{b,p} = 5$  mm,  $P_m = 116$  kW and  $G_m = 44.5$  S. In this example, as the bottom plate thickness is reduced, a limit on the maximum temperature value of the SP  $T_{max} < 1800$  °C was reached.

When searching for the CSM and voltage configuration on the CSM to reach the minimum depth and the maximum diameter of the pool mirror, the conditions were kept, that the SP temperature in its maximum zone did not exceed 1800 °C and the voltage on the CSM did not exceed 60 V.

*IMPACT OF THE VARIATION IN THE MOULD DIAMETER ON THE MP SHAPE*

The experiment was carried out in the range of the variation in the mould diameter  $D_m = 180\text{--}300$  mm. To obtain the sought parameters that will not exceed the operating ones, the voltage value on the CSM was taken as  $U = 35$  V and the distance between the product



**Figure 5.** Example of metal pool with the minimum depth for the given CSM configuration with the minimum bottom plate thickness



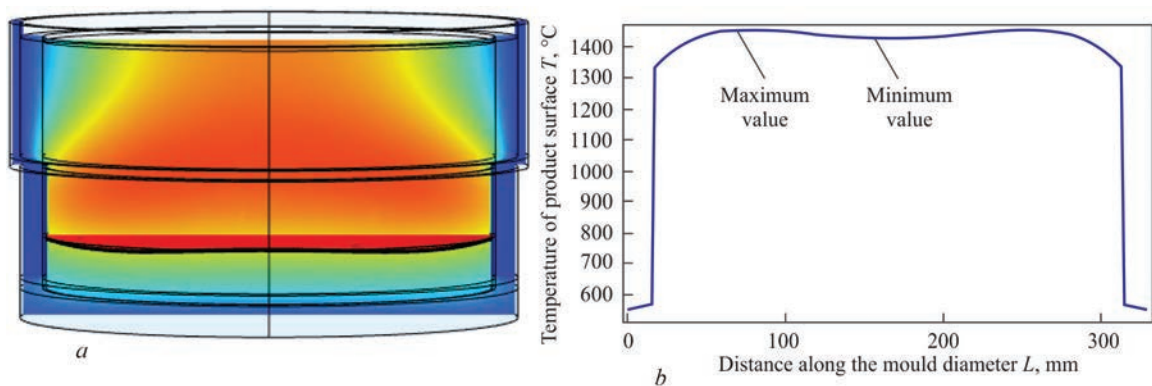
**Table 6.** Analysis of the impact of the bottom plate thickness on the MP parameters

Exp. No.	Thickness of bottom plate $h_{b,p}$ , mm	Power $P_m$ , kW	CSM conductivity $G_m$ , S	MP depth $H_{ij}$ , mm	MP mirror diameter $\varnothing_{mp}$ , mm	Max. temperature of the upper surface of the product, °C
1	20	71.9	56.5	7.2	162.0	1425
2	26	71.9	56.4	10.5	173.8	1464
3	30	71.9	56.4	12.5	176.0	1486

**Table 7.** Analysis of the impact of variation in the mould diameter on the MP parameters

Exp. No.	Mould diameter $D_m$ , mm	Power $P_m$ , kW	CSM conductivity $G_m$ , S	MP depth $H_{ij}$ , mm	MP mirror diameter $\varnothing_{mp}$ , mm	Max. temperature of the upper product surface, °C
1	180	74.4	60.8	10.6	176	1471
2	220	100.0	81.8	9.7	216	1451
3	260	126.0	102.8	5.7/7.5*	256	1402/1435*
4	300	152.0	124.0	5.1/7.1*	296	1355/1418*

\*At the mould diameter of 260 mm and higher; the voltage on the CSM  $U = 35$  V and the distance between the product and the level of the lower CSMS edge  $H_{pgl} = 53$  mm, MP takes the form of “sombbrero” [9] (see Figure 6), which is characterized by two values of  $H_{ij}$  parameters and the maximum values of the product surface temperature.



**Figure 6.** MP shape and temperature along the diameter of the upper product edge at the mould diameter of 260 mm: *a* — MP “sombbrero” shape; *b* — temperature distribution with the confirmation of unevenness in the form of “sombbrero” with the designation of the minimum and maximum temperature values

and the level of the lower edge of the CSMS was taken as  $H_{pgl} = 53$  mm. The results are given in Table 7.

The presented data indicate that the voltage values on the CSM being stable and the distance between the product and the lower edge of the CSMS being constant, the MP mirror diameter grows almost proportional to the mould diameter. The power consumed by the mould and electrical conductivity grow by about 20 % faster. The maximum temperature of the upper product surface remains almost unchanged. At the same time, the MP depth decreases almost twice, which leads to an increase in the ratio of the mirror diameter to the depth ( $\varnothing_{mp}/H_{ij}$ ) from 16.6 to 58.

## CONCLUSIONS

Based on the results of the analysis of the obtained experimental data, the dependence of the specific electrical conductivity of ANF-29 flux on the SP temperature at the point of its maximum value was constructed. The de-

pendences of the power consumed by the mould on the SP electrical conductivity for four degrees of operation of the TShP-10 power source were obtained.

Multiphysics modeling was performed, that allows modeling the Joule heating processes for manufacturing bimetallic products using a stationary current-supplying mould with a circular section in the process of melting a discrete additive at its batch feeding. The carried out mathematical experiments allowed finding the ways to optimize some values of the initial parameters of the surfacing process, including geometric CSM parameters.

The results obtained during the mathematical experiment showed that an increase in the SP depth, other geometric parameters being constant, leads to an increase in the MP depth. A significant impact of the wear of the lower GL edge on the MP parameters was revealed. As the wear increases, the depth and diameter of the MP decrease, the electrical conductivity and consumed power of the SP drop.

Replacing the copper CSMS bushing with a steel one while keeping voltage on the CSM has almost no impact on the variation in the power consumption and electrical conductivity, but leads to an increase in the MP depth and diameter.

The voltage on the CSM being constant, the impact of the variation in the wall thickness of the copper CSMS and FMS bushing on the electrical conductivity of the mould and its consumed power is almost absent.

The voltage on the CSM being constant, the impact of the variation in the bottom plate thickness on the electrical conductivity of the mould and its power is almost absent. However, an increase in the bottom plate thickness leads to an increase in the depth and diameter of the MP mirror.

As the mould diameter grows from 180 to 300 mm, the diameter of the MP mirror increases almost proportionally to the mould diameter. The power consumed by the mould and electrical conductivity rise by about 20 % faster. The maximum temperature of the upper product surface remains almost unchanged. At the same time, the MP depth is almost twice decreased, which leads to an increase in the ratio of the mirror diameter to the depth ( $\Phi_{mp}/H_{if}$ ) from 16.6 to 58.

Analysis of the research results will contribute in improvement of the mould design and the technology of the process of melting discrete additive at batch feeding in CSM.

## REFERENCES

1. Ksendzyk, G.V., Frumin, I.I., Shirin, V.S. (1980) *Electroslag remelting and surfacing apparatus*. Pat. GB 1568746A. <https://patentimages.storage.googleapis.com/6c/fe/4a/9f-5b70c9345524/GB1568746A.pdf>
2. (1986) *Metallurgy of electroslag process*. Ed. by B.I. Medovar et al. Kyiv, Naukova Dumka [in Russian].
3. Kuskov, Yu.M., Grishchenko, T.I. (2019) Formation of metal pool in current-supplying mould at electroslag process. *The Paton Welding J.*, **4**, 33–36. DOI: <https://doi.org/10.15407/tpwj2019.04.07>
4. Mamyshev, V.A., Shinskii, O.I., Sokolovskaya, L.A. (2018) Intensification of internal and external heat sink at the manufacture of cast billets in molds with different properties. Report 2. *Metall i Litiyo Ukrainy*, 300–301(5–6), 38–45 [in Russian].
5. Medovar, L.B., Tsykulenko, A.K., Chernets, A.V. et al. (2000) Examination of the effect of the parameters of the two-circuit system of electroslag remelting on the dimensions and shape of the metal pool. *Advances in Special Electrometallurgy*, **4**, 3–7.
6. Protokovilov, I.V., Porokhonko, V.B. (2014) Methods to control metal solidification in ESR. *Sovrem. Elektrometall.*, **3**, 7–15.
7. Hou, Z., Dong, Y., Jiang, Z. et al. (2022) Effect of an external magnetic field on improved electroslag remelting cladding process. *Int. J. Miner. Metall. Mater.*, **29**, 1511–1521. DOI: <https://doi.org/10.1007/s12613-021-2277-3>
8. Solovyov, V.G., Kuskov, Yu.M. (2018) Influence of technological and electrical parameters of ESS in current-supplying mould. *The Paton Welding J.*, **6**, 20–27. DOI: <https://doi.org/10.15407/tpwj2018.06.03>
9. Matvienko, V.N., Mazur, V.A., Leshchinsky, L.K. (2015) Evaluation of shape and sizes of weld pool in surfacing using combined strip electrode. *The Paton Welding J.*, **9**, 28–31. DOI: <https://doi.org/10.15407/tpwj2015.09.04>
10. Tomilenko, S.V., Kuskov, Yu.M. (2000) Regulation and stabilization of base metal depth penetration in electroslag surfacing in current-supplying mould. *Svaroch. Proizvodstvo*, **9**, 32–35 [in Russian].
11. Sokolovskaya, L.A., Mamishev, V.A. (2009) Mathematical modeling of problems with phase transitions in metallurgy and foundry. *Protsessy Litya*, **2**, 24–29 [in Russian].
12. Liu, Fb., Zang, Xm., Jiang, Zh. et al. (2012) Comprehensive model for a slag bath in electroslag remelting process with a current-conductive mould. *Int. J. Miner. Metall. Mater.*, **19**, 303–311. DOI: <https://doi.org/10.1007/s12613-012-0555-9>
13. Makhnenko, O.V., Milenin, A.S., Kozlitina, S.S. et al. (2016) Optimizing technological process of electroslag melting of steel cylindrical ingots based on results of mathematical modeling. In: *Proc. of 8th Int. Conf. on Mathematical Modeling and Information Technologies in Welding and Related Processes, 19–23 September 2016, Odesa*, 96–101.
14. Zhiwen Hou, Yanwu Dong, Zhouhua Jiang et al. (2018) Simulation of compound rolls produced by electroslag remelting cladding method. *Metals*, **7**(8), 504. DOI: <https://doi.org/10.3390/met8070504>
15. Kuskov, Yu.M., Solovyov, V.G., Lentyugov, I.P., Zhdanov, V.A. (2018) Electroslag surfacing of layers of different thickness in stationary current-supplying mould. *The Paton Welding J.*, **10**, 33–36. DOI: <https://doi.org/10.15407/tpwg2018.10.06>
16. Ksendzyk, G.V. (1975) Current-supplying mould providing slag pool rotation. *Spets. Elektrometall.*, **27**, 32–40 [in Russian].
17. Gukhman, A.A. (1973) *Introduction to the theory of similarity*. 2<sup>nd</sup> Ed. Moscow, Vysshaya Shkola [in Russian].

## ORCID

V.G. Solovyov: 0000-0002-1454-7520,  
Yu.M. Kuskov: 0000-0002-8091-2274,  
I.Yu. Romanova: 0000-0001-7154-1830

## CONFLICT OF INTEREST

The Authors declare no conflict of interest

## CORRESPONDING AUTHOR

V.G. Solovyov  
E.O. Paton Electric Welding Institute of the NASU  
11 Kazymyr Malevych Str., 03150, Kyiv, Ukraine.  
E-mail: [hhsova@gmail.com](mailto:hhsova@gmail.com)

## SUGGESTED CITATION

V.G. Solovyov, Yu.M. Kuskov, I.Yu. Romanova (2024) Optimization of the metal pool shape during electroslag surfacing in a stationary current-supplying mould for manufacture of bimetallic products. *The Paton Welding J.*, **5**, 28–36.

## JOURNAL HOME PAGE

<https://patonpublishinghouse.com/eng/journals/tpwj>

Received: 21.02.2024

Received in revised form: 04.04.2024

Accepted: 10.06.2024



DOI: <https://doi.org/10.37434/tpwj2024.05.05>

# STRUCTURE AND MECHANICAL PROPERTIES OF TITANIUM ALLOY-CARBON STEEL BIMETAL OBTAINED BY EXPLOSION WELDING

P.S. Shlonskyi, Feng Gao

Liaoning Xin Huayang Weiye Equipment Manufacturing Company Ltd No. 1 Road,  
Tieling high-tech industrial development zone, Liaoning province, China

**ABSTRACT**

The quality of the bimetal produced by explosion welding is affected by the mechanical characteristics of flying plate material. For development of explosion welding modes, a study of the structure and mechanical properties of titanium alloy Grade 12 (TA10, flying plate) + carbon steel 16 Mn (09G2S) bimetal was conducted. The thickness of the titanium alloy plates was 5 and 6 mm, the mechanical properties, namely the relative elongation in as-delivered condition for these plates differed by 15 %. The results on tear and shear strength of titanium alloy-carbon steel bimetal are given. In the case of titanium alloy TA10 it is demonstrated that for plates with a lower relative elongation, the strength of the joint produced by explosion welding is lower. Bending test showed no delamination for two thicknesses of the titanium alloy. Also, for the two thicknesses of the titanium alloy, the joint zone has a microstructure characteristic for explosion welding.

**KEYWORDS:** explosion welding, titanium-steel bimetal, mechanical properties

**INTRODUCTION**

Different branches of modern mechanical engineering feel an urgent need for titanium-steel bimetal. Production of this bimetal runs into difficulties, which are primarily related to the specific properties of titanium, namely formation of brittle intermetallic compounds in the joint zone.

Explosion welding is one of the methods, allowing production of titanium-steel bimetal, owing to a short duration of the process of the joint formation and absence of heating [1–3]. However, the task of producing sound titanium-steel bimetal has not been solved completely, as there exists a very narrow range for producing a sound joint, and also brittle intermetallic compounds form in the joint zone.

In the case of [4, 5], we can see that at present investigations on producing bimetal plates by explosion welding in the People’s Republic of China and in the world are concentrated, predominantly, on pure titanium. It should be noted that pure titanium strength drops with temperature rise, and after achievement of 250 °C it decreases two times. Therefore, titanium alloys should be used for equipment operating at higher temperatures. So, in [6] investigation of the properties of bimetal of TA10 titanium alloy and Q345 carbon steel was conducted.

**EXPERIMENTAL MATERIALS AND METHODS**

TA10 titanium is a low alloy of titanium of Ti–Mo–Ni system, containing 0.3 % Mo and 0.8 % Ni (Table 1),

which not only improves its high-temperature mechanical properties, but also provides its good corrosion resistance to chlorides with a low pH or to weakly-reducing acids, and its corrosion resistance is much better than that of pure titanium [7].

TA10 titanium alloy 5 and 6 mm thick was used as the flying plate. Mechanical properties of the material of the plates of different thickness are given in Tables 2 and 3. Relative elongation in as-delivered condition differed by 15 % for plates of different thickness. Plate size was 450×300 mm.

The objective of this work was investigation of the influence of relative elongation of TA10 titanium alloy on the mechanical properties and microstructure

**Table 1.** TA10 chemical composition according to GB/T 3620.1–2007 (PRC standard)

Ti, balance, %	Admixtures, not more than, %						
	Mo	Ni	Fe	C	N	H	O
	0.2–0.4	0.6–0.9	0.30	0.08	0.03	0.015	0.25

**Table 2.** Mechanical properties of 6 mm sheet of titanium alloy TA10

Material condition	$\sigma_y$ , MPa	$\sigma_t$ , MPa	$\delta$ , %
M	275	345	30

**Table 3.** Mechanical properties of 5 mm sheet of titanium alloy TA10

Material condition	$\sigma_y$ , MPa	$\sigma_t$ , MPa	$\delta$ , %
M	227	362	26



**Figure 1.** Appearance of plates of titanium alloy Grade 12 and carbon steel 09G2S before explosion welding (a) and after it (b) of the joint of TA10 + 09G2S bimetal produced by explosion welding.

During optimization of the mode of explosion welding of TA10 titanium alloy to 09G2S steel experiments were conducted on full-scale samples.

Used as the base was an 80 mm plate of 09G2S carbon steel.

The height of the explosive was 50 and 45 mm for 6 and 5 mm plates of the titanium alloy, respectively. The detonation rate was measured by wire sensors; it was 2100 and 2040 m·s<sup>-1</sup> for 6 and 5 mm plates, respectively. Plate appearance before (a) explosion welding and after welding (b) is shown in Figure 1.

Explosion welding was followed by heat treatment to relieve internal stresses at temperature not higher than 540 °C, and checking the joint quality by ultrasonic testing. Samples for mechanical tests were cut out by the scheme shown in Figure 2.

The collision velocity of the plates was calculated by the formula where:  $D$  is the detonation rate;  $r$  is the load coefficient during explosion welding, ratio of explosive weight to that of the flying plate [1].

Explosive density is equal to 1 g·cm<sup>-3</sup>.

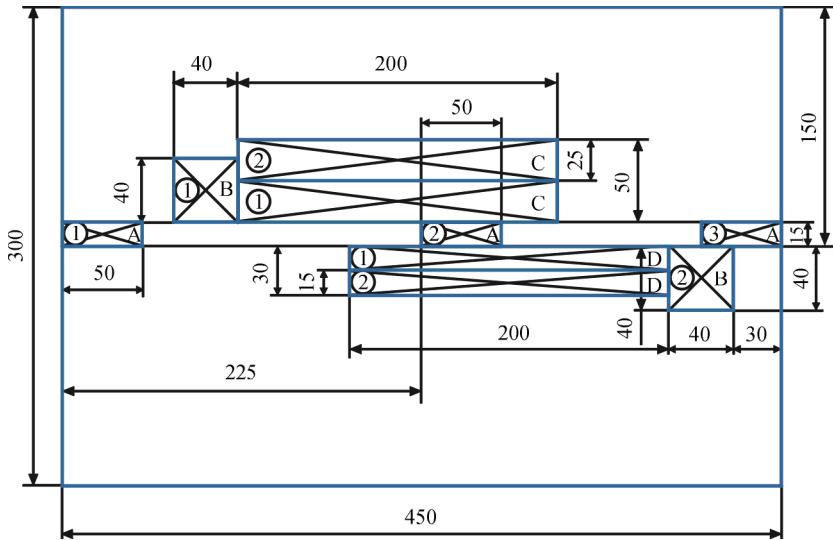
$$Vc = D \frac{\left( \sqrt{1 + \frac{32}{27}r} - 1 \right)}{\left( \sqrt{1 + \frac{32}{27}r} + 1 \right)}.$$

After performing a simple calculation, we get the collision velocity of 592 and 598 m·s<sup>-1</sup> for 6 and 5 mm plates, respectively. Thus, plate energies at collision will have close values, and the energy of 5 mm plate will be even lower.

Microstructural studies were performed in a metallographic microscope MS600. Microstructure of titanium alloy TA10 + 09G2S joint is shown in Figure 3.

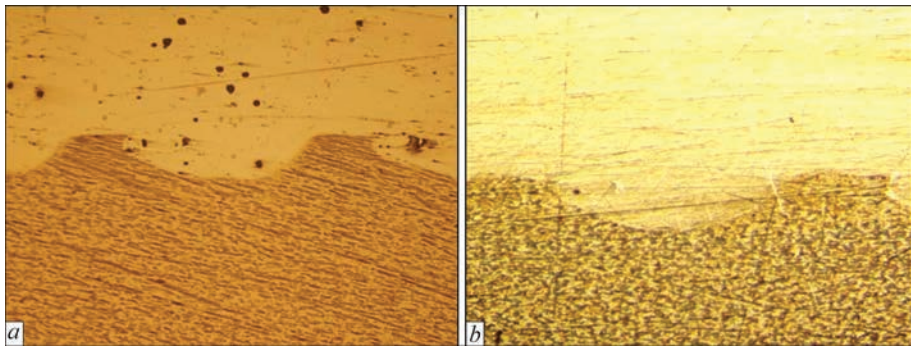
**EXPERIMENTAL RESULTS AND THEIR DISCUSSION**

As one can see from Figure 3, the joint zone has a wavy interface characteristic for explosion welding. The wave shape, their amplitude and frequency are almost the same for different cladding thicknesses. Here, intermetallic compounds in the form of dispersed inclusions in the regions on the wave back side are observed on the interface of TA10 + 09G2S joint with 5 mm cladding (Figure 3, b). It fully correlates



**Figure 2.** Scheme of cutting out samples for mechanical tests: 1A, 2A, 3A are samples for microstructural studies: 1B, 2B are samples for investigation of cladding tear strength; 1C, 2C are samples for studying the cladding shear strength; 1D, 2D are samples for studying the bending strength





**Figure 3.** Microstructure of the zone of the joint of titanium TA10 (top) + steel 09G2S (bottom), cladding thickness of 6 mm (a) ( $\times 100$ ) and 5 mm (b) ( $\times 200$ )

with the results of work [8], where the features of phase formation in pressure welding were studied.

Evaluation of mechanical properties of TA10 + 09G2S bimetal produced by explosion welding was performed by testing the cladding for tear, shear and bending.

Tear tests were conducted by pulling off around a circular contour. A test sample is placed into a tubular-shaped support, and on top a die is inserted into the blind hole on the sample, to which the rupture machine pressure is applied (Figure 4, a).

The tear strength of TA10 + 09G2S bimetal joint was determined by dividing the force applied to pull off the cladding, by the ring area. One can see from Figure 4, b that rupture occurred in the joint zone, that

is characteristic for titanium alloy — carbon steel bi-metal, and the joint line is of a clearly defined wavy shape.

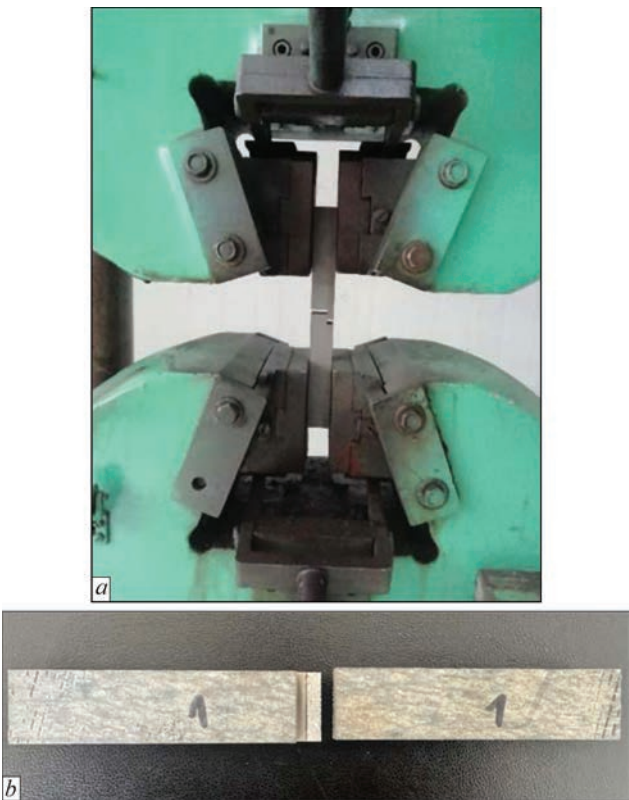
Results of tear and shear tests are shown in Table 4. As one can see from the results in Table 4, the tear strength for the titanium alloy with smaller relative elongation is lower by 73 and 112 % for samples from regions 1 and 2, respectively. The tear strength decreases by 92.5 % on average.

Shear strength tests of the bimetal were conducted by stretching flat samples with transverse cuts of the layers (Figure 5). The results of shear strength tests completely correlate with those of tear strength tests.

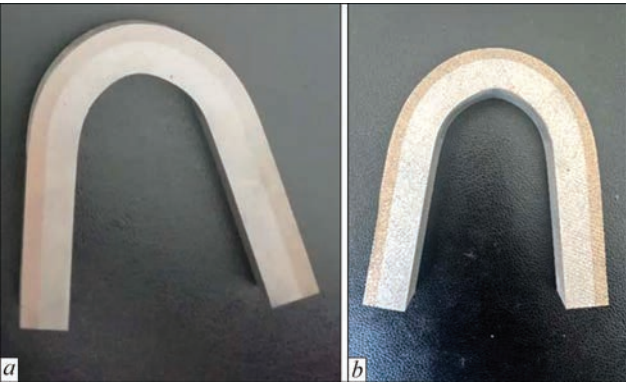
As one can see from Table 4, the shear strength for the titanium alloy with smaller relative elongation is 117 and 68 % lower for samples from regions 1 and 2, respectively. Shear strength at the beginning



**Figure 4.** View of tear tests of the cladding (a) and of samples after testing for 6 mm cladding (b)



**Figure 5.** View of shear strength tests (a) and of the sample after testing (b)



**Figure 6.** Bending tests of TA10 + 09G2S bimetal, cladding thickness of 6 mm (a), cladding thickness of 5 mm (b)



**Figure 7.** Appearance of TA10-09G2S bimetal tubesheet of 3340 mm diameter after heat treatment

of the sample is higher than that at the end for both the thicknesses. Shear strength decreases by 92.5 % on average. The discrepancy of mechanical testing results in regions 1 + 2 is attributable to dispersity of intermetallic formation.

At investigation of mechanical properties of the bimetal produced by explosion welding, bending test is quite revealing, as delamination in the joint zone takes place in case of poor quality welding. Samples for both the cladding thicknesses of 6 and 5 mm (Figure 6) withstood bending through 180° without delamination, which is indicative of a high welding quality.

Ultrasonic testing of the joint continuity showed absence of delaminations over the entire plane of the bimetal plate.

Based on the conducted investigations recommendations were provided on producing by explosion welding bimetal tubesheets of 3340 mm diameter for heat exchanger (Figure 7).

CONCLUSIONS

- 1. It was found that lowering of relative elongation by 15 % for titanium alloy TA10 leads to lowering of tear and shear strength by 92.5 % on average at close values of explosion welding energy.
- 2. As a result of the conducted work, recommendations were issued for correction of the mode of explosion welding of titanium alloy TA10 to carbon steel 09G2S with 5 mm cladding to improve the joint quality.

**Table 4.** Results of the cladding tear and shear tests for TA10 + 09G2S bimetal produced by explosion welding

Cladding thickness/ sample number	Tear strength, MPa	Shear strength, MPa
5 mm/No. 1	289.1	163.2
5 mm/No. 2	167.1	146.9
6 mm/No. 1	502.4	354.4
6 mm/No. 2	354.8	247

REFERENCES

1. Kudinov, V.M., Koroteev, A.Ya. (1978) *Explosion welding in metallurgy*. Moscow, Metallurgy [in Russian].  
2. Lysak, V.I., Kuz'min, S.V. (2005) *Explosion welding*. Moscow, Mechanical Eng. [in Russian].  
3. Deribas, A.A. (1980) *Physics of hardening and explosion-welding*. Novosibirsk, Science [in Russian].  
4. Zheng Yuanmou (2002) *Explosive welding and metal clad-ded materials as well as the engineering applications*. Central South University Press, Changsha.  
5. Wang Yaohua (2007) *Researches and practices on explosive welding of metal sheets*. National Defense Industry Press, Beijing.  
6. HAN Xiao-min, WANG Shao-gang, HUANG Yan et al. (2015) Interfacial microstructure and mechanical properties of TA10-Q345R composite plate with explosive welding. *Titanium Academics J., Nanjing*, 32(6), 24–29. DOI: <https://doi.org/10.3969/j.issn.1001-4837>.  
7. Findik, F. (2011) Recent developments in explosive welding. *Materials and Design*, 32(3), 1081–1093.  
8. Markashova, L.I., Arsenyuk, V.V., Grigorenko, G.M. (2002) Features of phase formation during pressure welding of dis-similar metals under high-speed deformation conditions. *Automatic Welding*, 9, 12–17 [in Russian].

ORCID

P.S. Shlonskyi: 0000-0002-3566-1752

CONFLICT OF INTEREST

The Authors declare no conflict of interest

CORRESPONDING AUTHOR

P.S. Shlonskyi  
Liaoning Xin Huayang Weiye Equipment  
Manufacturing Company Ltd No. 1 Road,  
Tieling high-tech industrial development zone,  
Liaoning province, China.  
E-mail: [shlensk@ukr.net](mailto:shlensk@ukr.net)

SUGGESTED CITATION

P.S. Shlonskyi, Feng Gao (2024) Structure and mechanical properties of titanium alloy-carbon steel bimetal obtained by explosion welding. *The Paton Welding J.*, 5, 37–40.

JOURNAL HOME PAGE

<https://patonpublishinghouse.com/eng/journals/tpwj>

Received: 26.01.2024  
Received in revised form: 15.03.2024  
Accepted: 15.05.2024



# UltraMARS SYSTEM FOR NON-DESTRUCTIVE MEASUREMENT OF RESIDUAL STRESSES: NEW DEVELOPMENTS

J. Kleiman

Structural Integrity Technologies, Inc. (Sintec) Markham, Ontario, Canada

ABSTRACT

One of the effective methods for non-destructive testing of residual and operating stresses is the acoustic method that is based on the propagation of elastic ultrasonic vibrations inside a solid body. A portable complex for measurement of applied and residual stresses in solid materials using an acoustic non-destructive stress control method was developed in the early 2000 by a team of scientists from Integrity Testing Laboratory, Sintec and E.O. Paton Electric Welding Institute (PWI). An advanced complex UltraMARS was developed based on the early prototype that allows measuring the magnitude and the sign of operating and residual stresses in laboratory and field conditions, either averaged through thickness, or in surface and subsurface layers, as well as monitoring stresses in metal structural elements during their manufacture, repair and operation. It is effective in assessing the quality of welded joints, after post-weld treatments carried out in order to redistribute residual stresses. It has been successfully used in various applications in marine, aerospace, construction and other industries. A four-pole transducer has been developed to improve the operational characteristics of the UltraMARS complex in monitoring stresses on the surface and in the near-surface layers of the material. It differs from the used two-pole transducers of the surface wave (Surface-Rayleigh Wave — Transducer RF12) and subsurface wave (Subsurface — Transducer SF12) in having two transmitter-receiver pairs located at 90° to each other. This change allowed measuring the velocity of ultrasonic waves simultaneously in both orthogonal directions without rotating the transmitterreceiver by 90°. To use these transducers with the UltraMARS complex, a transmitter-receiver switching program has been developed. A transducer with a variable pole distance was also developed for measurement of residual stresses in the near-surface layers of materials, making it possible to determine the uniaxial induced stresses to a depth from 0 to 8–10 mm by changing the base distance between the emitter and receiver. At the moment, a stress control technique is being developed. 22 Ref., 10 Figures.

**KEYWORDS:** residual stresses, non-destructive ultrasonic measurement of residual stresses, UltraMARS, variable base transducer, 4-pole transducer

INTRODUCTION

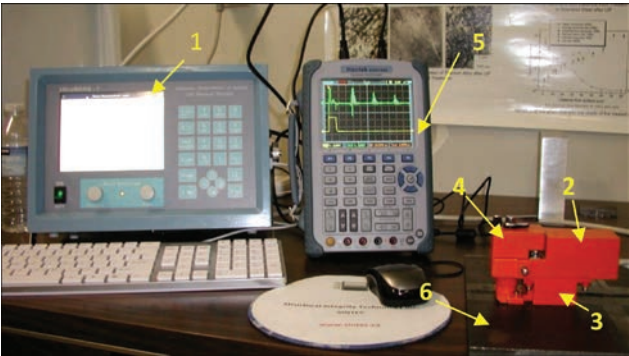
Residual stresses (RS) play a very important role in the integrity of structural members, as they can significantly change the mechanical properties of materials and thus affect fatigue life, deformation, dimensional stability, corrosion resistance, etc. The control of operating (acting) and residual stresses (RS) is becoming top priority in many industries [1–3].

In the last few decades, more and more research has been carried out on use of ultrasound to measure residual stresses in materials of various designs and to measure the elastic-acoustic constants of materials. Numerous examples of stress measurements in bulk (average in thickness) and surface layers have shown that ultrasonic methods can be used for non-destructive evaluation of stresses in various materials, being especially suitable for measuring stress profiles and evaluation of stress distributions at the same point after different treatment conditions [4–9].

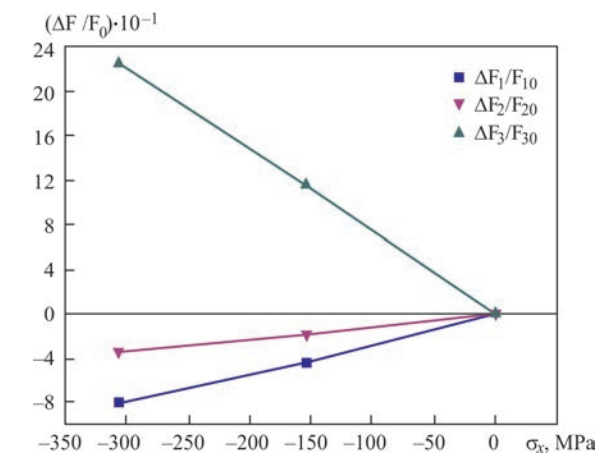
In recent years we made significant progress in modernizing the UltraMARS complex that makes it possible to measure operating and residual stresses not only in bulk (average through thickness), but also in surface and near-surface layers of materials. Using the method for determining stresses, developed by

PWI [5], we designed the hardware and developed the software, making it possible to measure all three types of reflected ultrasonic signals at the same point using a non-destructive method [6, 10].

Generally, the change in the speed of an ultrasonic wave in materials under the action of stresses amounts only to tenths of a percent. Therefore, the equipment for the practical application of the ultrasonic method for measuring residual stresses must be of high resolution and fully computerized. The developed UltraMARS complex, shown in Figure 1, includes a measurement unit; a preamplifier for excitation and



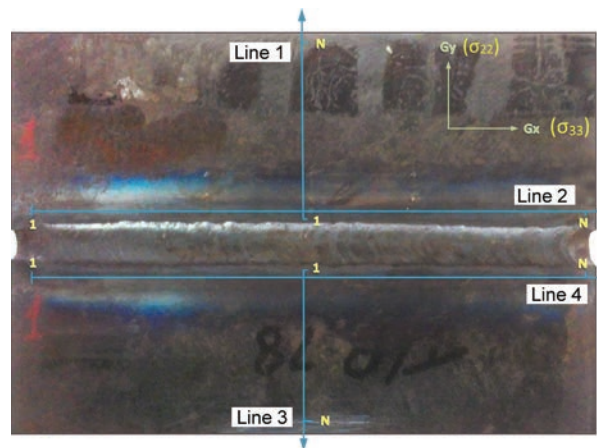
**Figure 1.** Ultrasonic computerized complex for residual and applied stress measurement: 1 — measurement unit with supporting software; 2 — preamplifier (REW component); 3 — magnetic holder; 4 — transducer; 5 — oscilloscope (20 MHz); 6 — sample



**Figure 2.** Changes of ultrasonic wave velocities in a sample of a material under the action of applied stresses

reception of reflected ultrasonic signals (REW) before they are sent to the measurement unit for further processing; a transducer holder that can be either magnetic or electromagnetic or mechanical; a set of replaceable ultrasonic transducers that are used for excitation and reception of longitudinal (XF3) and shear (YF12) waves; as well as for excitation and reception of surface waves (RF12) and subsurface waves (SF12). An oscilloscope is usually used for visual control of the received reflected signals. Typically, the oscilloscope is needed to select and tune to a reflected waveform when using the manual method.

The developed UltraMARS complex makes it possible to determine single- and biaxial working (applied) and residual stresses in various materials and structures. This article will, firstly, review the latest advances in the development and application of the non-destructive ultrasonic method for measuring of residual stresses in materials and structures and present examples of stress measurement in various materials and structures and introduce the new transducers that are at different stages of development, i.e. the four-pole transducer and the variable base transducer for measuring stresses at different depths of materials.



**Figure 3.** Welded sample (low carbon steel) with marked lines 1–4 indicating the locations of RS measurements

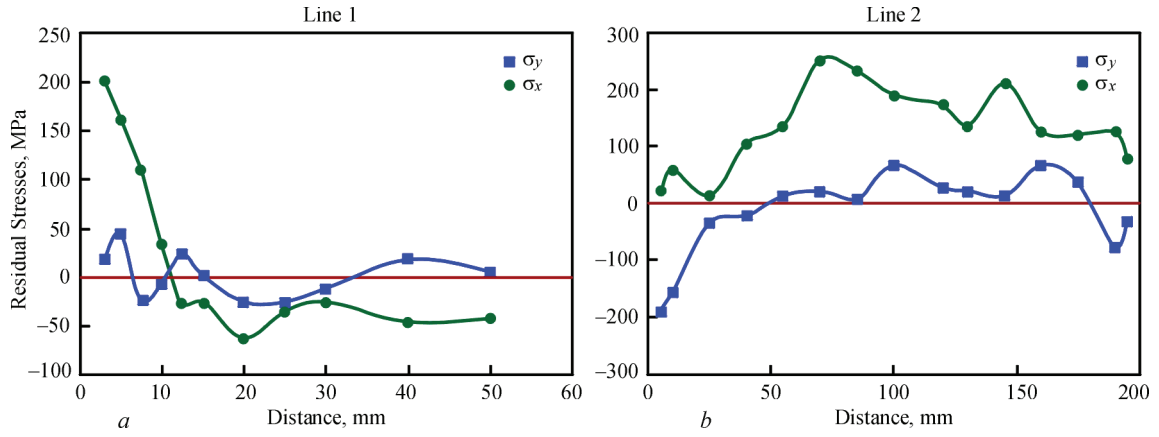
### MEASUREMENT OF RESIDUAL STRESSES BY ULTRASONIC METHOD

The measurements of residual stresses (RS) using ultrasound are based on solid theory [11–13] and original technique and use of precise instrumentation [5, 10, 12]. It is possible to use ultrasound for measurement of stresses in materials, because, according to the acoustic-elastic theory of interaction of ultrasound with materials, the changes in travel velocities (or frequencies) of ultrasound in a material depend linearly on the stresses in the materials over a certain range of stresses (Figure 2). The intensity and nature of such changes may vary depending on the physical and mechanical properties of the material. With known acoustic-elastic properties of the material, the determination of stresses is reduced to measuring the velocities (proportional to frequency) of longitudinal and shear waves, when they propagate in the main directions of stress action. The acoustic-elastic properties of the material are included in the equations relating the propagation velocities of ultrasonic waves to the stresses in the material in the form of proportionality coefficients. They are determined by the elasticity constants of the second and third orders and can be calculated or measured [13, 18].

For determination of the elasticity constants, control samples are used, in which, under uniaxial or biaxial loading, changes in the velocities of longitudinal and shear ultrasonic waves are measured and the calculation of acoustic-elastic coefficients based on these measurements is performed.

The UltraMARS complex performs these measurements, and the calculated values of the acoustic-elastic coefficients are stored in memory for further stress calculation [3 and references therein]. The measurement error of operating stresses in the elastic region is  $\sim 15$  MPa, and for residual stresses is  $\pm 0.1 \sigma_t$ , where  $\sigma_t$  is the ultimate tensile stress of the material.

Figure 3 through Figure 5 are presented as examples of the type of residual stress information that can be achieved using the UltraMARS system with different transducers. A butt-welded sample shown in Figure 3, measuring  $200 \times 150$  mm and 12 mm thick, was used for residual stress measurements. The distribution of the longitudinal and transverse residual stresses (respectively, parallel and perpendicular to the weld direction) were measured along lines 1 and line 2, as marked in Figure 3. The stresses were measured starting from point 1 (as marked in Figure 3) and advancing towards point marked as N. Measurement point 1, on line 1, was located at a distance of  $\sim 3$  mm from the weld toe. All measurements along lines 2 were made at a distance of  $\sim 5$  mm from the



**Figure 4.** The distribution of average through thickness (bulk ultrasonic waves) residual stresses in the sample along line 1 (a) (normal to the weld direction) and along line 2 (b) (along the weld direction)

weld toe. To measure the residual stresses even closer to the weld/bead or in the weld require special preparation of the surface of the weld/bead or removing of the weld reinforcement.

Figure 4. presents the measurement results of average through thickness residual stresses along lines 1 and 2 obtained with the bulk transducers. In all cases, two components of the residual stress,  $\sigma_{22}$  and  $\sigma_{33}$  were measured (marked in the figures as  $\sigma_x$  and  $\sigma_y$ , respectively).

In technical literature, different symbols are used to mark the distribution of residual stresses and propagation velocities of ultrasonic waves [13, 18]. Among the most common used, one can mention the following:

- symbol  $\sigma_{33}$  (or  $\sigma_x$ ) — marks the longitudinal principal stress that is acting along the application of external force or along the weld (see Figures 3 and 4);
- symbol  $\sigma_{22}$  (or  $\sigma_y$ ) — marks the transverse principal stress that is acting perpendicular to the applied external force or in the direction perpendicular to the weld (see Figures 3 and 4);
- symbol F3 (or F1) — denotes the frequency (propagation velocity  $V_{Sx3}$ ) of the reflected (bottom) shear ultrasonic wave, excited and received back by a Y-cut piezoelectric transducer. The polarization vec-

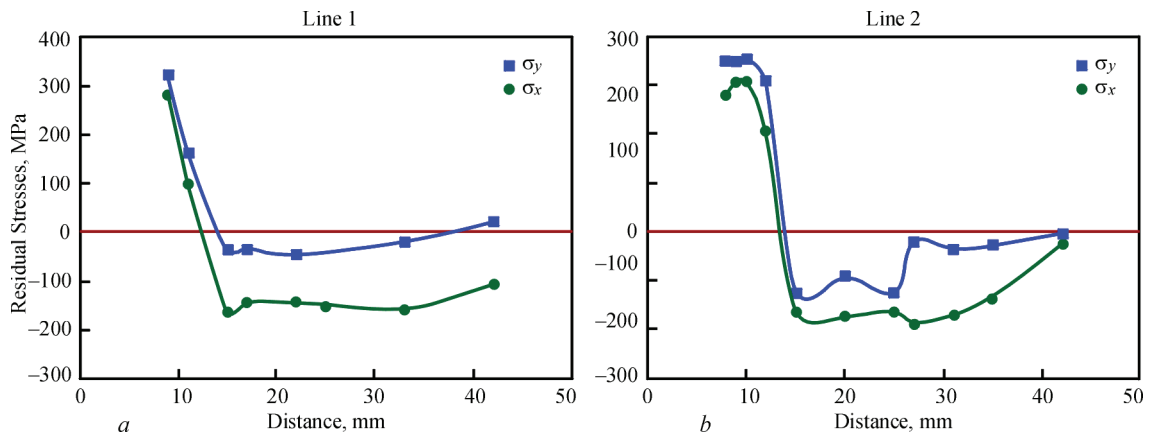
tor of the piezoelectric transducer is directed along the action of the stress  $\sigma_{33}$  ( $\sigma_x$ ), and the plane in which the particles oscillate in the element is directed perpendicular to the wave propagation (along the thickness of the material);

- symbol F2 — denotes the frequency (propagation velocity  $V_{Sx2}$ ) of the reflected (bottom) shear ultrasonic wave. The polarization vector of the piezoelectric transducer is directed along the action of the stress  $\sigma_{22}$  (or  $\sigma_y$ ) or perpendicular to the action of the stress  $\sigma_{33}$  (or  $\sigma_x$ ), and the plane in which the particles oscillate is directed perpendicular to the propagation of the wave (along the thickness of the material);

- symbol F1 (or F3) — frequency (propagation velocity  $V_{Lx1}$ ) of the reflected (bottom) longitudinal ultrasonic wave, excited and received by a X-cut piezoelectric transducer.

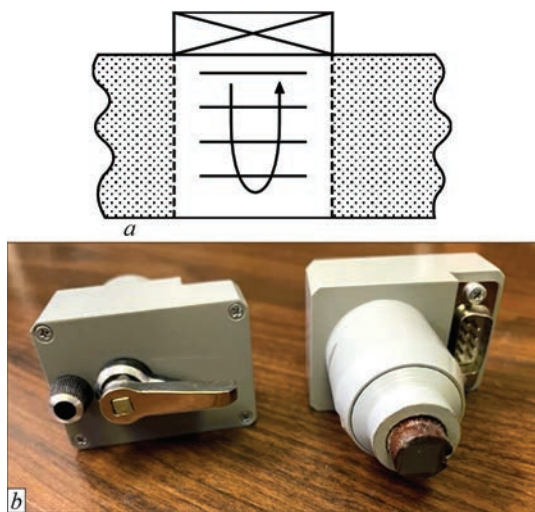
The polarization vector of the piezoelectric transducer can be at any angle to the direction of the stress  $\sigma_{33}$  (or  $\sigma_x$ ), and the particles in the element oscillate in the direction of wave propagation (along the thickness of the material).

Figure 5 shows the distribution of surface (a) and subsurface (b) residual stresses in the sample as mea-



**Figure 5.** The distribution of surface residual in the sample as measured along Linne 1 using the surface (a) and subsurface (b) ultrasonic wave transducers (in both cases the stresses normal to the weld direction were measured)





**Figure 6.** Principle of measurement of average through thickness (bulk) stresses (pulse-echo) and the transducers for measurement of the longitudinal and the transversal components of average through thickness (bulk) stresses

sured along Line 1 using the surface (RF12) and sub-surface (SF12) ultrasonic wave transducers (in both cases the stresses normal to the weld direction were measured). Using the surface ultrasonic transducer allows to measure residual stresses in surface layers of material, with a penetration depth for this application being  $\sim 0.7$  mm (determined experimentally). By using subsurface transducers, it is possible to measure stresses to a depth of  $\sim 6$  mm. The  $9 \times 4$  mm standard transducer was selected for this application.

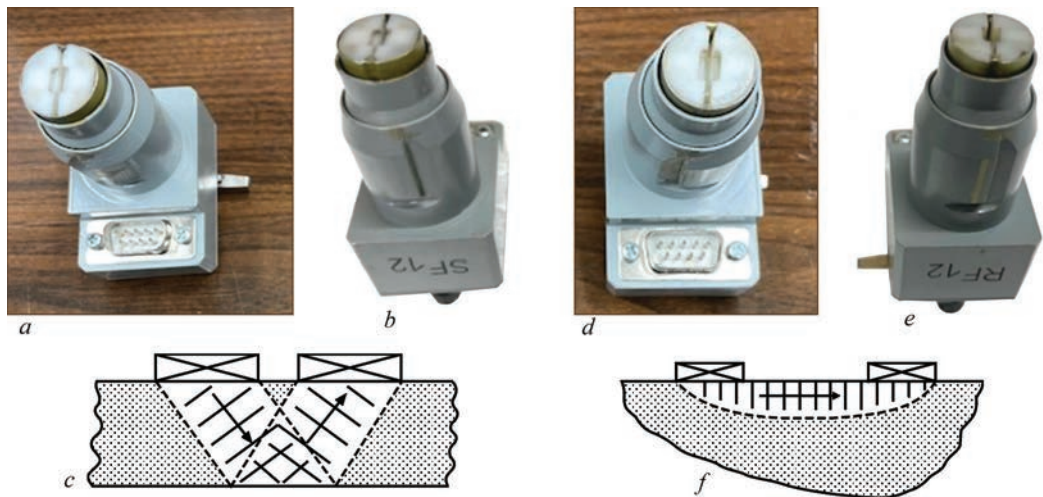
The obtained RS profiles were analyzed and the obtained data had shown that the results of ultrasonic RS measurements in the sample are in accordance with existing understanding of the distribution of RS in welded elements and structures [14, 15]. In a study of residual stresses in a large-scale welded panel, designed to represent structural elements of a ship, good coincidence between the measured stresses and calculations using the FEA method was demonstrated [16, 17].

Recently, the UltraMARS complex was modified further, including a number of new technical solutions, making the operation of the complex more stable and user-friendly. The symbols denoting the major stresses and frequencies have been replaced. Thus,  $\sigma_1$  determines the vector of the main stress acting along the applied force to the structure or weld;  $\sigma_2$  determines the vector of the main stress acting perpendicular to the force applied to the structure or weld. The frequency designation symbols have been also changed, tying them to the new stress symbols. The use of new electronic elements made it possible to improve the tuning to the wave in automatic mode and increase the accuracy of identification of received reflected signals. Changes have been also made to the calculation of stresses when using surface and subsurface wave transducers.

### ULTRASONIC TRANSDUCERS

Presently, the measurement of average through thickness longitudinal and transverse residual stresses in the sample are performed (respectively, parallel and perpendicular to the welding direction) at each point by two types of ultrasonic transducers (Figure 6). To excite bulk ultrasonic waves, quartz plates with a polarization vector Y-cut (cut along the optical Y axis) and X-cut (cut along the optical X axis) with a 5 MHz resonant frequency of quartz piezoelectric plates were used. This is the optimal frequency of quartz oscillation, at which mechanical ultrasonic oscillations respond to changes in the crystals of the material from stresses and do not attenuate when reflected from the lower surface of the sample.

Piezoelectric PZT plates with a resonant frequency of 4 MHz are used to excite and receive the Rayleigh surface ultrasonic wave (Figure 7, *a–c*). The plates are glued to a damper made of a solid polyamide material



**Figure 7.** Principle of measurement of sub-surface (*a–c*) and surface (*d–f*) stresses (pitch-catch) and the transducers for measurement of two transversal components of stresses



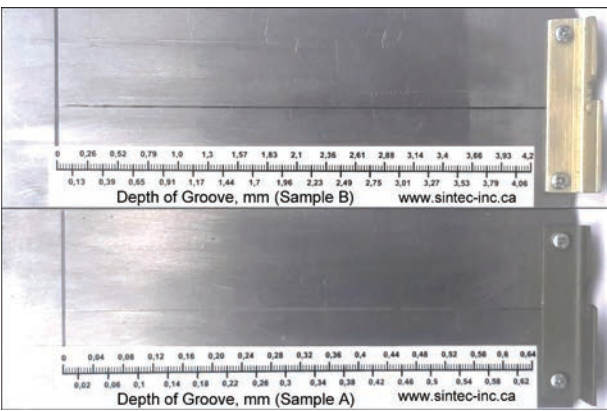
**Figure 8.** Images of the four-pole transducers for measurements of surface and subsurface stresses

with good wear resistance [20, 21]. The wedge angles of the emitter and receiver for the surface wave are 70° [20–22]. The damper with glued piezoceramic plates is protected by a metal cap.

For excitation and reception in the near-surface layers of the material, piezoelectric PZT plates with a resonant frequency of 4 MHz are used. The plates are glued to a damper with the emitter and receiver wedge angles at 29° (Figure 7, *d–f*) [20–22] that makes it possible to obtain the maximum amplitude of received ultrasonic waves for various metals. The damper with glued piezoceramic plates is protected by a metal cap.

To simplify the measurements of surface and subsurface stresses, four-pole transducers were developed that, unlike two-pole transducers, allow measurements in two directions without turning the transducer head 90°. The transducer dampers are made by milling them from a solid polyamide block that has good abrasion strength. The PZT plates with a resonant frequency of 4 MHz were then attached to transmitters and receivers. The wedge angles of the transmitter and receiver for the surface wave is 70°, and for the subsurface 29° that allows to obtain the maximum amplitude of the received waves for different metals. The transmitter and the receiver are placed opposite each other at a constant base distance. The second transmitter-receiver set is placed at 90° to the first one. To reduce interference between the transmitter and the receiver, a square recess is made in the damper housing, which does not allow interference from the transmitter to the receiver. The damper housing with piezoceramic plates is protected by a metal cap. The whole damper assembly is inserted into the transducer housing (Figure 8). To conduct a measurement, the four-pole transducer is inserted into the REW device (item 3 in Figure 1) of the UltraMARS-8 instrument.

To check the penetration depth of the ultrasound waves for the two-pole and four-pole transducers,

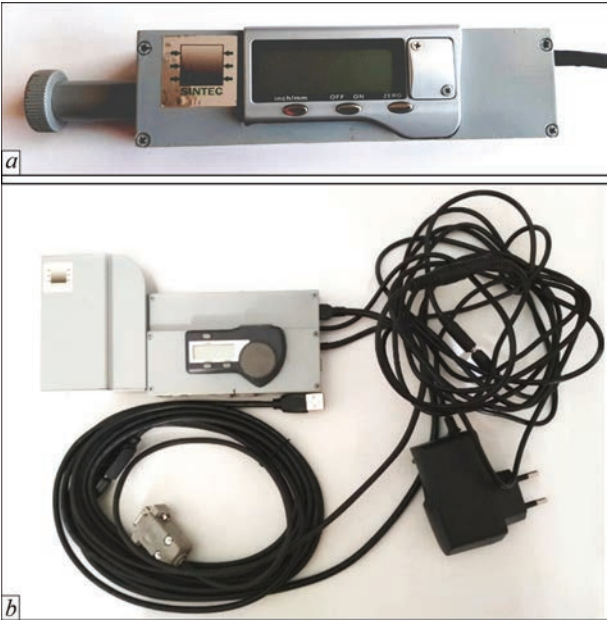


**Figure 9.** Images of the plates with a slot cut in them for evaluating the propagation depth of the ultrasonic wave in materials. The rulers with marked slot depth are attached to the plates

plates were made from various metals with a groove cut into them. The depth of the groove was made with an increasing slope of a few degrees, and a ruler was attached to the plate, showing the change in depth of the groove with distance, starting from 0 mm and continued, to reach the thickness of the metal (Figure 9).

A study is now in progress to evaluate the depth penetration of the surface (RW) and subsurface (SW) waves in 2-pole and 4-pole transducers in steel and aluminum plates prepared as described above with increasing slope grooves.

A transducer with a variable base between the emitter and the receiver was developed recently. Figure 10 shows the developed transducer with a variable base that emits and receives longitudinal critically refracted (LCR) waves. In this transducer, the receiver and transmitter can move relative to each other. The distance between them (base) can be changed either



**Figure 10.** Images of the variable base LCR transducers with a manual (*a*) and a mechanized (*b*) change of distance between the emitter and the receiver (top view)



manually by turning the handle on the side of the transducer (Figure 10, *a*) or by a command from the UltraMARS system (Figure 10, *b*). Presently, work is underway to develop programs to acquire and process the stresses and for controlling the movements of the emitter and the receiver in the transducer. The transducer is attached to the sample with permanent magnets that ensures good contact between the transducer and the sample. A coupling lubricant is used to ensure efficient signal transmission from the PZT crystals to the sample. In this design the base distance between the transmitter and the receiver varies from 10 mm to 50 mm.

By changing the base distance, one can change the propagation depth of the LCR wave that allows to probe different layers of the sample. The wedge angle of the transmitter and receiver was chosen to be  $29^\circ$  [20–22]. This angle was chosen based on the maximum amplitude of the received signal for different metals. The developed prototypes are currently undergoing various tests, the results of which will be published elsewhere.

## CONCLUSIONS

Through selected examples, it has been shown that an acoustic method that is based on the propagation of elastic ultrasonic vibrations inside a solid body can be effectively used for nondestructive testing of residual stresses in materials. An UltraMARS complex was developed and recently modernized for measurement of the magnitude and the sign of operating and residual stresses, either averaged through thickness, or in surface or sub-surface layers of materials, in laboratory and field conditions. The developed technology allows monitoring stresses in metal structural elements during their manufacture, repair and operation. It is also effective in assessing the quality of welded joints, after post-weld treatments carried out in order to redistribute residual stresses.

A four-pole transducer has been developed to improve the operational characteristics of the UltraMARS complex in monitoring stresses on the surface and in the near-surface layers of the material, allowing measuring the velocity of ultrasonic waves simultaneously in both orthogonal directions without rotating the transmitter-receiver in the transducer by  $90^\circ$ .

A variable-base transducer was designed and manufactured that allows measuring uniaxial induced residual stresses in the near-surface layers of materials to a depth up to  $\sim 10$  mm by changing the base distance between the emitter and receiver.

Work is now in progress on extensive evaluation of the new transducers and developing a stress control technique for the variable-base transducer.

## REFERENCES

1. Kleiman, J., Kudryavtsev, Y. (2012) Residual stress management in welding: residual stress measurement and improvement treatments. In: *Proc. of ASME 2012 31<sup>st</sup> Inter. Conf. on Ocean, Offshore and Arctic Engineering*, 6: *Materials Technology; Polar and Arctic Sciences and Technology; Petroleum Technology Symp.*, Rio de Janeiro, Brazil, July 1–6, 2012, 73–79.
2. O'Brien, E. (2002) Crack tip residual stress and structural health monitoring. *Materials Sci. Forum*, **404–407**, 779–784.
3. Kleiman, J., Kudryavtsev, Y., Sugihara, H., (2018) Structural health monitoring (SHM) of residual and applied stresses using a non-destructive ultrasonic technique. In: *Proc. of the Twenty-eighth Inter. Ocean and Polar Engineering Conf.*, Sapporo, Japan, June 10–15, 2018, 1372–1376.
4. Bray, D.E. (2002) Ultrasonic stress measurement in pressure vessels, piping and welds. *J. of Pressure Vessel Technology*, **124**(3), August, 326–335.
5. Gushcha, O.Y., Kot, V.G., Smilenko, V.M., Brodovoy, V.O. (2011). *Acoustic method of controlling subsurface stresses in solid media*. Pat. Ukraine UA-93297.
6. Kudryavtsev, Y., Kleiman, J., Gushcha, O. (2000) Residual stress measurement in welded elements by ultrasonic method. In: *Proc. of IX Inter. Cong. on Experimental Mechanics*, Orlando, Florida, USA, June 5–8, 2000, 954–957.
7. Rollins, F.R.Jr., Kobett, D.R., Jons, CMJ J.L. (1963) *Study of ultrasonic methods for nondestructive measurement of residual stress*: Technical Documentary Report, WADD-TR-61-42, Pt II, January, 1–38.
8. Schneider, E. (2009) Evaluation of stress states of components using ultrasonic and micro magnetic techniques. In: *Proc. of the ASME 2009 Pressure Vessels and Piping Division Conf.*, PVP2009, July 26–30, 2009, Prague, Czech Republic, 1–9.
9. Uzun, F., Bilge, A.N., (2011) Investigation of total welding residual stress by using ultrasonic wave velocity variations. *GU J. Sci.*, **24**(1), 135–141.
10. Kudryavtsev, Y., Kleiman, J., Gushcha, O. et al. (2004) Ultrasonic technique and device for residual stress measurement. In: *Proc. of X Inter. Cong. and Exposition on Experimental and Applied Mechanics*, Costa Mesa, California USA, June 7–10, 2004, 1–7.
11. Hughes, D.S., Kelly, J.L. (1953) Second-order elastic deformation of solids. *Phys. Rev.*, **92**(5), 1145–1149.
12. Murnaghan, T.D. (1951) *Finite deformation of an elastic solid*. John Wiley, New York.
13. Guz, A.N., Makhort, F.G., Gushcha, O.I. (1977) *Introduction to acoustoelasticity*. Kyiv, Naukova Dumka [in Russian].
14. Kudryavtsev, Y., Kleiman, J., Gushcha, O. (2000) Ultrasonic measurement of residual stresses in welded railway bridge. In: *Proc. of NDT Conf. on Structural Materials Technology*, Atlantic City, NJ, February 28–March 3, 2000, 213–218.
15. Bate, S.K., Green, D., Buttle, D. (1997) *A review of residual stress distributions in welded joints for the defect assessment of offshore structures*: HSE Books, OTH 482.
16. Polezhayeva, H., Kang, J.-K., Lee, J.-H. et al. (2010) A study on residual stress distribution and relaxation in welded components. In: *Proc. of the Twentieth Inter. Offshore and Polar Eng. Conf.*, Beijing, China, June 20–25, 2010, 282–289.
17. Kudryavtsev, Y., Kleiman, J., Polezhayeva, H. (2011) Ultrasonic measurement of residual stresses in welded elements of ship structure. In: *Proc. of Integrating Simulation and Experimentation for Validation (ISEV) on Inter. Conf. on Advances in Experimental Mechanics*, Edinburgh, Scotland, September 7–9, 2011.
18. Gushcha, O.I. (1994) Non-destructive analysis of inhomogeneous fields of residual stresses in welded joints. *Avtomatich. Svarka*, **7–8**, 3–5 [in Russian].



19. Gushcha, O.I., Makhort, F.G. (1995) Application of the acoustic method for determining residual stresses in welded structures. *Technical Diagnostics and Non-Destructive Testing*, 4, 8–15 [in Russian].
20. Ermolov, I.N., Razygraev, N.P., Shcherbinsky, V.G. (1978) Use of head-type acoustic waves for ultrasonic testing. *Defectoscopy*, 1 [in Russian].
21. Razygraev, N.P. (2003) Head waves in non-destructive testing of metal structures. *World of Non-Destructive Testing*, 22(4), December.
22. Viktorov, I.A. (1966) *Physical foundations for the use of Rayleigh and Lamb ultrasonic waves in technology*, Science.

#### ORCID

J. Kleiman: 0000-0003-1011-7504

#### CORRESPONDING AUTHOR

J. Kleiman  
Structural Integrity Technologies, Inc. (Sintec)  
Markham, Ontario, Canada.  
Email: jkleiman@itlinc.com

#### SUGGESTED CITATION

J. Kleiman (2024) UltraMARS system for non-destructive measurement of residual stresses: New developments. *The Paton Welding J.*, 5, 41–47.

#### JOURNAL HOME PAGE

<https://patonpublishinghouse.com/eng/journals/tpwj>

Received: 11.03.2024

Received in revised form: 13.04.2024

Accepted: 14.06.2024



**OKOndt GROUP**

📍 Turkey, Ankara

## Eddy current flaw detector ETS2-73



**Commissioning of  
the flaw detector and  
training of  
Turkish specialists**

▶ ProNDTSolution

✉ sales@ndt.com.ua

☎ (044) 531 37 26 (27)

**www.nfd.com.ua**

# SIMULATION OF ELECTRIC ARC MODE OF ELECTRIC FURNACE AND ANALYSIS OF ITS OPERATION IN REAL TIME

**M.M. Gasik**

Aalto University, 00076, AALTO, Espoo, Finland

## ABSTRACT

A model of a three-phase electric furnace is considered, for which the distribution of temperature and electric field over the volume is calculated. Areas of the furnace are shown, in which extreme values of current density and temperature occur. The simulation results are compared with the real data of the 12 MVA furnace operation in factory conditions, and the features of the furnace operation in various modes are discussed.

**KEYWORDS:** simulation, furnace, electric mode, temperature distribution, current density

## INTRODUCTION

Ore-renovation electric furnaces in the production of ferroalloys, mattes, molten refractories, slag and other products at high temperatures use high-power current, operating in arc, arc-free or mixed electric modes [1, 2]. Arc-free mode is typical of multislag processes, where reactions occur on the slag-melt interface, and the electric arc is almost absent. An example of such a process may be manganese slag dephosphorization for melting silicomanganese, higher grades of ferromanganese and metal manganese [2] and processes of slag refining in the production of copper, nickel and metals of the platinum group [3].

Despite the absence of an electric arc in the working volume and the associated turbulence of melts movement, the analysis of such thermal and electric modes of furnaces is a complex problem as far as it has many uncertain parameters and their direct experimental measurement is often impossible. Thus, simulation of the furnace operation allows evaluating and predicting local values of important variables (temperature, current density, speed of movement of metal and slag flows, kinetics of chemical reactions, etc.), if the corresponding parameters were applied during simulation. The best result can be obtained during experimental confirmation of the model in real time, but in factory conditions, the amount of data being registered is rather limited. Earlier, the authors have shown that such models can be used with high efficiency when analyzing the operation of electrocalcinators for thermoanthracite production [4], where it is impossible to obtain direct data directly from the volume of the calcinator.

For the purpose of developing a well-grounded and adjusted model, in this research, the 12 MVA furnace in the arc-free mode, its electrical and thermal parameters, measured in the real-time mode and the appropriate digital twin for calculations are considered.

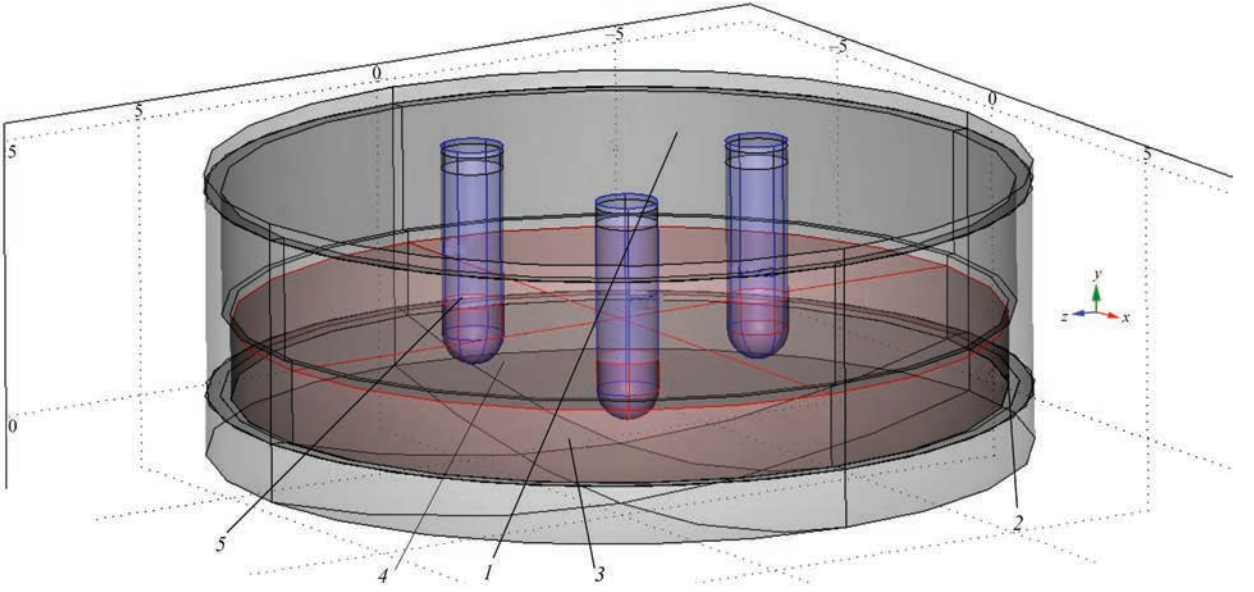
## FURNACE MODEL AND RESULTS OF CALCULATIONS

The model of a three-phase electric furnace, operating in the resistance mode (arc-free mode) with a diameter of 13 m, with self-sintering electrodes of 1100 mm diameter and a rated capacity of 12 MVA was created with the COMSOL Multiphysics 5.4 package. The model includes furnace casing with lining, closed flue, molten metal and slag volumes and upper interlayer rich in coke (Figure 1). All materials have set equations of heat and electrical conductivity, heat capacity, density, etc. depending on the temperature, and for the liquid phase, the viscosity equation is also added [5]. Thermal mode of the furnace in the model is introduced by general differential equations of heat conductivity and convective heat exchange, and electric mode is introduced by the system of Ampere–Maxwell's equations, where the vector of current density  $\mathbf{J}$ :

$$\mathbf{J} = \nabla \times \mathbf{H} = \sigma(\mathbf{E} + \mathbf{v} \times \mathbf{B}) + i\omega \mathbf{D} + \mathbf{J}_{ext} \quad (1)$$

where  $\mathbf{H}$  is the vector of magnetic field elasticity;  $\mathbf{E}$  is the vector of electric field strength;  $\mathbf{v}$  is the speed of movement of electrically conductive environment;  $\mathbf{B}$  is the vector of magnetic induction;  $\mathbf{D}$  is the vector of electric displacement;  $i = \sqrt{-1}$ ,  $\omega = 2\pi f$  is the angular frequency of the field ( $f = 50$  Hz);  $\mathbf{J}_{ext}$  is the density of external current (in the case is absent);  $\sigma$  is the electrical conductivity of the environment. Differential equations based on the electric field intensity  $\mathbf{E} = -\nabla \varphi$  have the following form:





**Figure 1.** Scheme of three-phase furnace model (coordinate sizes in meters): 1 — crypt; 2 — wall; 3 — bottom-plate; 4 — melt; 5 — electrode

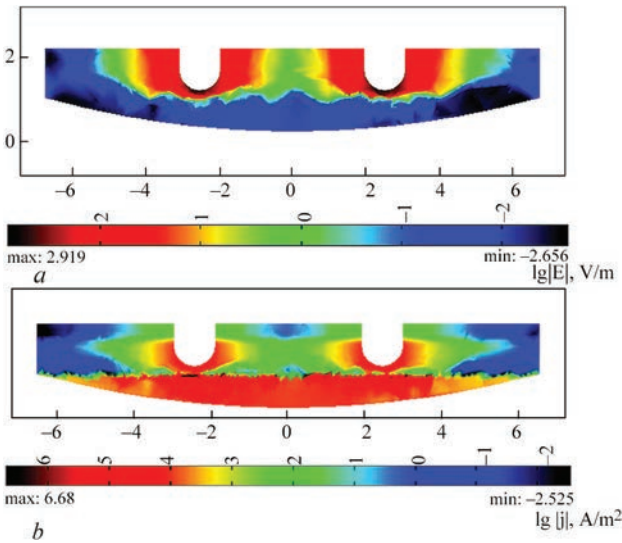
$$\begin{aligned}
 & -\nabla \left( (i\omega\sigma - \omega^2\epsilon\epsilon_0) \mathbf{A} - \sigma \mathbf{v} (\nabla \times \mathbf{A}) + \right. \\
 & \left. + (\sigma + i\omega\epsilon\epsilon_0) \nabla\phi - (\mathbf{J}_{ext} + i\omega\mathbf{P}) \right) = 0; \\
 & (i\omega\sigma - \omega^2\epsilon\epsilon_0) \mathbf{A} + \nabla \left( (\mu\mu_0)^{-1} \nabla \times \mathbf{A} - \mathbf{M} \right) - \\
 & -\sigma \mathbf{v} (\nabla \times \mathbf{A}) + (\sigma + i\omega\epsilon\epsilon_0) \nabla\phi = \mathbf{J}_{ext} + i\omega\mathbf{P},
 \end{aligned} \quad (2)$$

where  $\mathbf{A}$  is the vector magnetic potential;  $\phi$  is the scalar electric potential;  $\mathbf{M}$  is the vector of magnetization environment;  $\mu$  is the relative magnetic permeability;  $\mu_0 = 4\pi \cdot 10^{-7}$  is the magnetic permeability of vacuum. It should be emphasized that the calculations consider the entire volume of the furnace with electrodes, lining and casing. Therefore, in equations (1, 2), a mag-

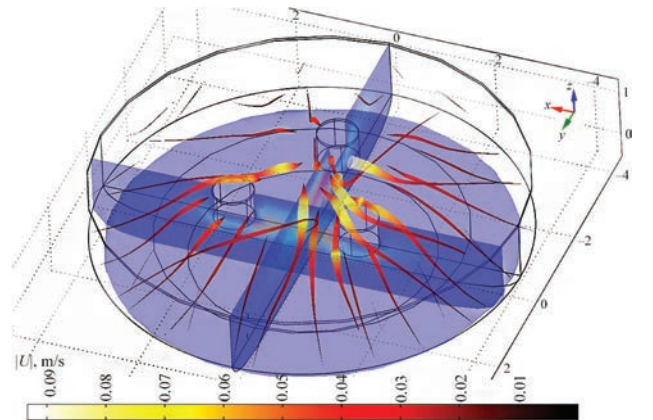
netic contribution for metal design elements can be very significant. These equations do not have a clear temperature contribution, but almost all variables depend on the temperature. Thermal model of the furnace has a contribution from the electric  $W_e$  and magnetic  $W_m$  powers of the system:

$$\begin{aligned}
 W_e &= \int_{\Omega} \left( \int_0^T \mathbf{E} \frac{\partial \mathbf{D}}{\partial t} dt \right) d\Omega; \\
 W_m &= \int_{\Omega} \left( \int_0^T \mathbf{H} \frac{\partial \mathbf{B}}{\partial t} dt \right) d\Omega,
 \end{aligned} \quad (3)$$

where  $\Omega$  is the volume of the furnace (with electrodes and lining);  $T = 1/f$  is the period of current harmonics (1/50 s). Partial derivatives from  $W_e$  and  $W_m$  in time are electric and magnetic powers, respectively, the sum of which is associated with ohmic (active) and reactive components of the Poynting theorem:

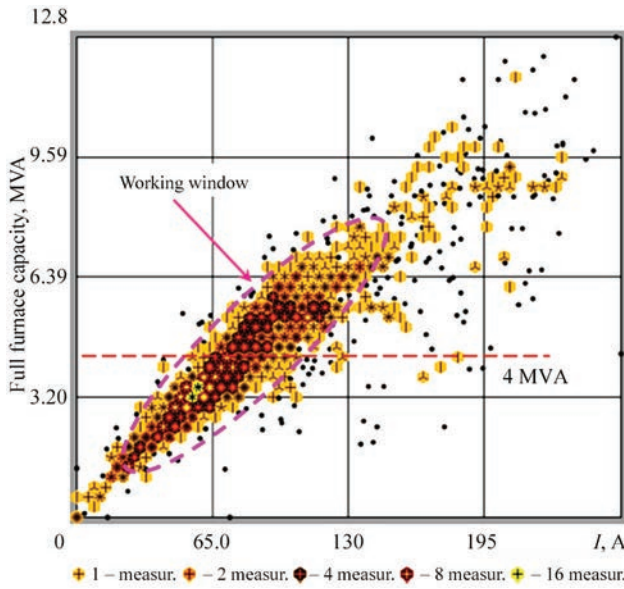


**Figure 2.** Logarithms of amplitude of electric field gradient (a) and current density in the furnace cross-section (b). Digits of colour scale — logarithms relative to electric field gradient (V/m) and current density (A/m²)



**Figure 3.** Amplitude of melt movement speed in a three-phase furnace model

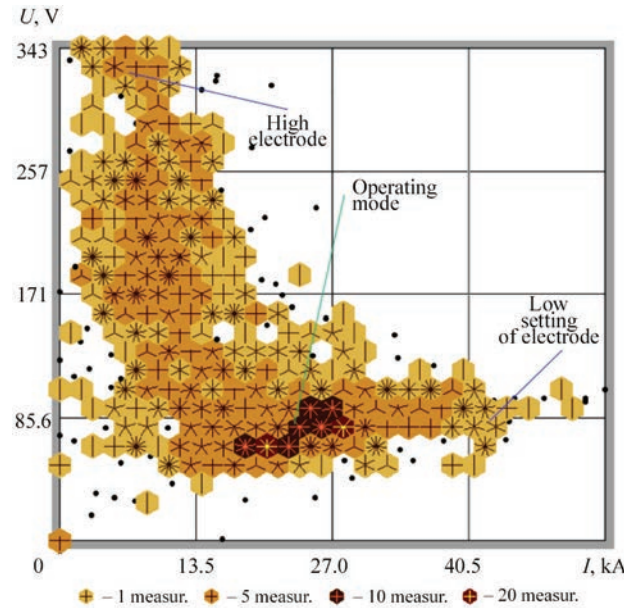




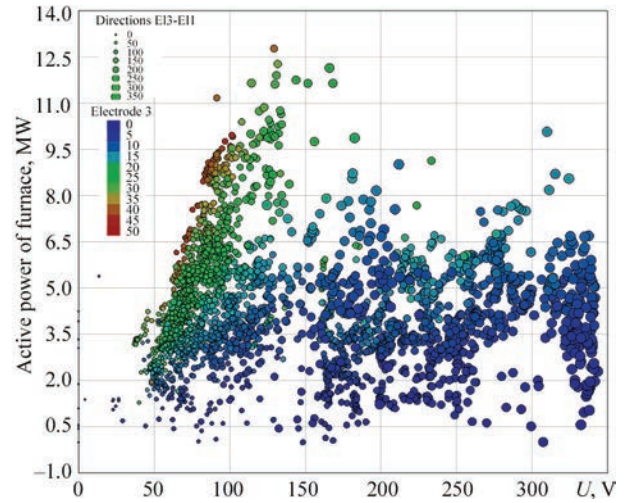
**Figure 4.** Power as a transformer primary current function (log data on real-time furnace operation\*)

$$\begin{aligned} -\int_{\Omega} \left( \mathbf{E} \frac{\partial \mathbf{D}}{\partial t} + \mathbf{H} \frac{\partial \mathbf{B}}{\partial t} \right) d\Omega = \\ = \int_{\Omega} \mathbf{J} \cdot \mathbf{E} d\Omega + \oint_S (\mathbf{E} \times \mathbf{H}) \cdot \mathbf{n} dS, \end{aligned} \quad (4)$$

where  $\mathbf{n}$  is the normal vector to the surface  $S$ , limiting the volume  $\Omega$  of the furnace. The first member in the right part of the equation (4) is the ohmic losses (Joule heat) and the second one is the reactive and radiation electromagnetic losses. Ohmic losses are added to the heat transfer equations as a generated thermal power



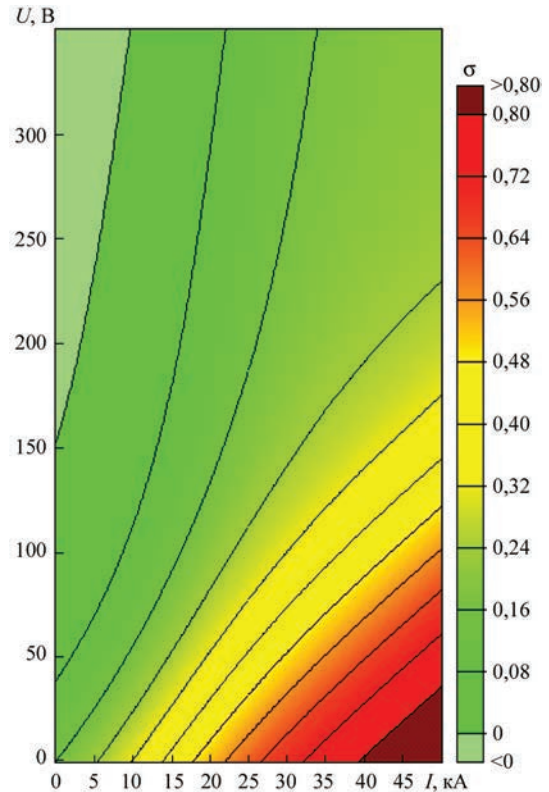
**Figure 5.** Voltage between the first electrode and hearth of the furnace and current on the first electrode (log data on real-time furnace operation)



**Figure 6.** Active power as a voltage function between the third electrode and hearth of the furnace (log data on real-time furnace operation are presented in a 4D-format)

er together with the enthalpy of chemical reactions. Thus, the system of basic differential equations is nonlinear and it requires iterative solutions together with the heat and mass exchange equations [4, 5].

On the electrodes in the model of this research, a harmonic phase voltage with an amplitude of 140 V and a frequency of 50 Hz was applied, and these pa-



**Figure 7.** Dependence of effective electrical conductivity on voltage between the electrodes and electrode current according to the results of neural network computations [6]

\*The average value of the furnace power in the analyzed month was about 4 MVA (red line). The oval outlines the range of primary current of the transformer and the furnace power, in which the furnace operated the longest amount of time.

rameters were used to calculate the distributions of electric field gradient  $|E|$  in the volume (Figure 2, *a*) and current density (Figure 2, *b*). According to the results (Figure 2), the highest current density is observed near the ends of the electrodes between the electrodes and inside the molten metal ( $>10^6$  A/m<sup>2</sup>), whereas near the lining of the furnace, it is reduced to 0.003 A/m<sup>2</sup>.

Since the specific electrical resistance of the metal is much lower than that in slag or coke interlayer, active power and, accordingly, thermal power also exhibit low values there. Thus, the highest thermal power is observed directly in the area of the electrodes immersed in slag (in Figure 2, exactly in the locations of the reddest zones for the electric field and current density at the same time).

The uneven distribution of power and temperature leads to the convection movement of metal and slag melts, the maximum of which (up to 0.1 m/s) is observed near the electrodes as a result of lower viscosity and higher temperature gradients in these areas (Figure 3).

### ANALYSIS OF REAL FURNACE OPERATION

For the electric furnace similar to the model above, experimental data (approximately 4,000 lines of temperature and electrical logs data collected in a one calendar month) were collected in real factory conditions. The furnace with a rated capacity of 12 MVA is operating to refine slag in a limited temperature range and, therefore, it usually operates with much lower electrical load compared to its rated capacity. The ellipse dotted line (Figure 4) outlines the working window of the electric furnace mode (the highest statistical amount of data), but there are also more distant points for various reasons (electrodes freezing, short circuit, incorrect movement or electrode breakdown, other reasons, maintenance, etc.).

An unconventional format of the diagram (Figure 4) allows covering the whole picture of the furnace operation. For example, a yellow point with six “petals” indicates here 96 ( $16 \times 6$ ) measurements, since one petal is equal to 16 measurements, having the same value. For a dark yellow point, one petal is equal to one measurement, for black one — four measurements, etc. This allows showing high dimensionality data in a 2D-diagram. Figure 5 shows data on voltage between the first electrode and hearth of the furnace and current on the first electrode. These data indicate in particular the frequency of furnace staying with a high or low electrode, as well as the area of the highest number of cases of normal operation (for example at 70–120 V and 20–30 kA).

Data of the furnace operation can also be represented in a 4D format (Figure 6), where along the abscissa axis, voltage between the third electrode and hearth of the furnace is marked; along the ordinate axis, active power is marked and the colour of each point corresponds to the value of current on the electrode at a moment and the size of a point corresponds to the voltage between the first and third electrodes.

Results in Figure 6 indicate essential features in the furnace operation. Thus, red points (high current of up to 50 kA) show the limit of power and voltage, which are regulated by the overall electrical resistance of the furnace at a particular measurement moment. Large blue points indicate a high electrode setting (low current and high voltage), and small blue points indicate cases of rising and switching off electrodes (low active power at low current and voltage).

The electrical power system of the furnace is based on transformers converting input high mains voltage and low current on the primary side to a level suitable for the furnace operation [1]. At normal operation, all three transformers have the same parameters that provide symmetrical conditions of the furnace operation. If displaced settings occur (points in Figures 4–6, that deviate significantly from the working area), this leads to circulating unbalanced currents in triangular connections [5], which may be not detected by standard measurements, that may cause malfunction of the electrical equipment (except for the cases of normal technological maintenance).

From Figures 4 and 5, it is seen how the change in the electrode position affects the flow direction of current and power. In turn, the area near the ends of the electrodes (Figure 2) is hotter and has a lower resistance. Therefore, it is necessary to avoid direct immersion into the molten metal as it will lead to electric breaking.

The results show that even simple electrotechnical log data contain a considerable amount of information, which at the moment of required visualization can indicate many significant parameters regarding deviations from optimal modes and possible ways to improve operation of the furnace. It is also necessary to point out the agreement of the model values with real data, which makes it possible to create the so-called digital twin of the furnace and simulate its operation in computer networks. Figure 7 shows the calculated efficient electrical conductivity depending on the voltage between the electrodes and the electrode current, which was generated by a neural network computation on the example of [6] based on the



real furnace data given above (Figures 4–6) and the proposed computer model (Figures 1–3).

Results in Figure 7 show that at a low electrode position (high current, low voltage gradient), the efficient electrical conductivity (taking into account the metal, slag and coke interlayer) is the highest and it is significantly non-linear in relation to electrical parameters of the furnace. Such tools can be used to simulate different situations of the furnace to determine its optimal operation.

CONCLUSIONS

1. The model of the ore-renovation 12 MVA furnace was designed and shown, for which the distributions of electric field gradient in the volume, current density and movement of molten metal and slag as a result of temperature gradient and melt properties were calculated.
2. In parallel with the simulation, log data of the furnace operation in factory conditions in real-time modes were analyzed and options for visual analysis of this data were presented, which helps to understand the furnace operation and the reasons for deviation of the electric mode from the set one.
3. By combination of the model and real data, the possibility of creating digital twin of the furnace was shown, where parameters can be calculated and different furnace situations can be simulated to determine the optimal operation.
4. The carried out analysis shows the possibilities of using modern computing tools to control the operation of metallurgical units and their further improvement.

REFERENCES

1. Gladkykh, V.A., Gasyk, M.I., Ovcharuk, A.M., Projdak, Yu.S. (2004) *Design and equipment of electric steel making and ferroalloy shops*. Dnipropetrovsk, Systemni Tekhnologii [in Ukrainian].
2. Gasik, M.I. (1992) *Manganese*. Moscow, Metallurgiya [in Russian].
3. Larsen, B. (2012) Electrode models for Söderberg electrodes. In: *Proc. SAIMM «Platinum 2012», South Africa, Johannesburg*, 275–286.
4. Gasik, M.M., Gasik, M.I., Urazlina, O.Yu., Kutuzov, S.V. (2010) Modelling and optimisation of anthracite treatment in an electrocalcinator. In: *Proc. of 12<sup>th</sup> Inter. Ferroalloys Congr. INFACON, Helsinki, Finland*, 1, 339–347.
5. Gasik, M. (2013) *Handbook of Ferroalloys: Theory and Technology*. Elsevier/Butterworth-Heinemann, Oxford, UK.
6. Gasik, M.M., Gasik, M.I. (2010) Multi-variation analysis and optimisation of electrical conductivity of MnO–CaO–SiO<sub>2</sub> slags. In: *Proc. of 12<sup>th</sup> Inter. Ferroalloys Congr. INFACON, Helsinki, Finland*, 2, 537–545.

ORCID

M.M. Gasik: 0000-0002-5782-7987

CORRESPONDING AUTHOR

M.M. Gasik  
Aalto University, 00076, AALTO, Espoo, Finland.  
E-mail: michael.gasik@aalto.fi

SUGGESTED CITATION

M.M. Gasik (2024) Simulation of electric arc mode of electric furnace and analysis of its operation in real time. *The Paton Welding J.*, 5, 48–52.

JOURNAL HOME PAGE

<https://patonpublishinghouse.com/eng/journals/tpwj>

Received: 18.02.2024

Received in revised form: 25.03.2024

Accepted: 07.06.2024



International Congress Centre in Katowice, Poland  
15-17 October 2024

9th edition of the International Welding  
Fair ExpoWELDING

The most important welding fair in Poland and one of the most recognized industry events in Europe, where market leaders present the latest solutions related to welding technology.

[www.expowelding.pl/2024](http://www.expowelding.pl/2024)



## DNIPROMETYZ TAS: EXPANDING HORIZONS AT THE DÜSSELDORF WIRE 2024 EXHIBITION

Wire 2024 Exhibition, which is the largest international event dedicated to the production of wire, cables and related equipment and technologies, held every two years, took place in Düsseldorf, Germany, from 15 to 19 April 2024.



The exhibition presents the latest developments and innovations in the field of production and use of wire and cables, as well as accompanying equipment and materials. It is an important place for meeting and exchange of experience for professionals from different sectors such as energy, telecommunications, automotive and construction. For the DNIPROMETYZ TAS plant, this is not only an opportunity to present its products, but also to prove its commitment to innovation and quality.

During five days, filled with energy and dynamics, attention was focused on innovation and new

trends. Automation and robotization of processes turned out to be the decisive factors in improvement of the quality and stability of welded joints, which are important in the context of the future orientation.

The exhibition was housed in eighteen pavilions with a total area of about 306,888 square meters and brought together more than 2,725 companies from 64 countries. Having overcome all the problems of wartime, three Ukrainian companies were able to take part in the work of Wire exhibition at independent stands: DNIPROMETYZ TAS Company — Dnipro, PJSC “Stalkanat-Silur” Production Association — Odesa, PJSC “Garant Metyz Invest” — Zhovti Vody.

Before the start of the exhibition, the March issue of Wire Journal, which is the official publication of the International Wire Association, was published. The 120 pages of the Journal contain several scientific papers and “a lot” of useful information for producers and consumers of wire and products from it. *Daily WIRE & TUBE*, a bilingual (English and German) exhibition newspaper, was freely distributed every day during the exhibition. The almost 600-page Wire exhibition catalog contains complete contact information about the companies and firms that participated in the work of Wire 2024.

The DNIPROMETYZ TAS plant worthily performed alongside other leading global companies in the field of welding and metal cutting, presenting its products.

Visitors who visited the DNIPROMETYZ TAS stand had a unique opportunity to be acquainted with the full range of welding materials, receive detailed information about the products of the Ukrainian brand, and communicate with representatives of the plant.

An assortment of welding wires was presented at the stand:

- copper-plated solid welding wire G4Si1 with diameters of 0.8; 1.0; 1.2; 1.4, 1.6, 2.0 mm on cassettes of 15; 5; 2.5; 1 kg with precision winding;
- uncoated polished solid welding wire with diameters of 0.8; 1.0; 1.2; 1.6 mm on cassettes of 15 and 18 kg;
- welding wire in branded packaging for robotic complexes in barrels weighing 250 kg.

Of particular interest to visitors was the availability of a certificate of conformity from Deutsche Bahn. This certificate confirms high product quality and safety, which meets the European standards. This increased the confidence of customers and partners in the products.



\*The catalog of Wire Exhibition can be found at the editorial Board of “The Paton Welding J.”.



The purpose of participation of the DNPROMETYZ TAS Company in the Wire 2024 exhibition is not only to demonstrate products, but also to confirm the reputation of a reliable partner with high standards of quality and service. The company strived to ensure that every visitor to the stand not only saw a supplier, but also a strategic partner ready to help them succeed.

Summing up the results of participation in the Wire 2024 exhibition, it is worth noting the interest of consumers from different countries in welding materials from Ukrainian manufacturers. Over five days, the DNPROMETYZ TAS team held numerous meetings with existing and potential clients, and took part in the effective exchange of experience and ideas with other manufacturers of welding materials and representatives of related industries.

Negotiations are currently underway on the supply of welding wire and electrodes produced by DNPROMETYZ TAS to new potential clients in different regions of the world. Thanks to the high quality and reliability of its products, DNPROMETYZ TAS continues to successfully conquer foreign markets, demonstrating its products to customers from different countries, and maintaining the high status of the “MADE IN UKRAINE” label at the global level.